Numerical analysis of windscreen effects on air-cooled condenser fan performance and blade loading

by
Adam John Venter

Thesis presented in partial fulfilment of the requirements for the degree of Master of Engineering (Mechanical) in the Faculty of Engineering at Stellenbosch University

Supervisor: Dr. Michael Owen
Co-supervisor: Dr. Jacques Muiyser

March 2020

The financial assistance of the National Research Foundation (NRF) towards this research is hereby acknowledged. Opinions expressed and conclusions arrived at, are those of the author and are not necessarily to be attributed to the NRF

Declaration

By submitting this thesis electronically, I declare that the entirety of the work contained therein is my own, original work, that I am the sole author thereof (save to the extent explicitly otherwise stated), that reproduction and publication thereof by Stellenbosch University will not infringe any third party rights and that I have not previously in its entirety or in part submitted it for obtaining any qualification.

Date: .....
Signature: .....

Abstract

Numerical analysis of windscreen effects on air-cooled condenser fan performance and blade loading

A.J. Venter

Department of Mechanical and Mechatronic Engineering,
University of Stellenbosch,
Private Bag X1, 7602 Matieland, South Africa.

Thesis: MEng (Mech)

March 2020

Wind is recognized as the most significant challenge facing air-cooled condenser (ACC) performance. Wind exacerbates the flow distortions that occur at the fan unit inlets, which aggravates fan performance losses and blade vibrations. Consequently, multiple wind effect mitigation strategies have been formulated, of which the installation of porous peripheral windscreens that span along and beneath the perimeter of an ACC fan platform is included. However, the benefit of peripheral windscreens is not widely known and the available literature surrounding their impact is inconsistent. Some studies suggest that windscreens offer an increase in perimeter fan performance, while others suggest the contrary or that windscreens are mostly beneficial in reducing blade loading. This study, therefore, undertook to construct and validate numerical techniques that can be used to explore the mechanisms that determine the effect of peripheral windscreens on both ACC fan performance and dynamic blade loading. The ensuing numerical model replicates an experimental ACC fan row test facility and is shown to be able to deliver quantitative assessment of fan row performance effects and qualitative assessment of dynamic blade loading effects. For the experimental facility characteristics, representative of an ACC of low platform height, the model indicates that the installation of peripheral windscreens primarily degrades fan row performance. Based on fan row volumetric effectiveness, a maximum performance deficit of 19% (expressed as a percentage difference relative to the no-screen scenario) accompanies the installation of a windscreen (50% solidity material) covering 50% of the peripheral inlet area at a platform height wind speed of 6.6 m/s (approximated full-scale wind speed of 10 m/s). Conversely, the model shows that the peripheral windscreens offer favourable reductions in edge fan dynamic blade loading. The reduction in fan row performance is attributed to the development of a low pressure wake behind the screens and the favourable reduction in dynamic loading to the creation of more uniform and symmetric velocity profiles through the edge fan's inlet. Moreover, the effective platform height of the experimental facility model is adapted to offer a preliminary assessment of the influence of platform height on the windscreen effects. Resultantly, it appears that the windscreen blade loading effects are largely independent of platform height, while fan row performance effects are shown to exhibit a more definite dependence. It is uncovered that favourable enhancement of fan row performance is attainable once the configuration of the screen and platform height is able to deflect the accelerated flow region, which forms beneath the screen, past the fan row completely; a scenario more easily attained at lower wind speeds with taller platform heights. The numerical techniques described and validated in this study are well-positioned for adoption into future wind effect simulation studies, particularly full-scale simulation.

Uittreksel

Numeriese analise oor die effek van windskerms op lug-verkoelde kondensor waaier werkverrigting en lembelasting

("*Numerical analysis of windscreen effects on air-cooled condenser fan performance and blade loading*")

A.J. Venter

Department of Mechanical and Mechatronic Engineering,
University of Stellenbosch,
Private Bag X1, 7602 Matieland, South Africa.

Tesis: MIng (Meg)

Maart 2020

Wind word gereken as die belangrikste uitdaging wat lugverkoelde kondensors (*air-cooled condenser* (ACC)) se werkverrigting beïnvloed. Wind vererger die vloei-vervormings wat by die inlaat van die waaier-eenheid voorkom, wat die waaier se werksverrigting-verlies en die vibrasies van die lemme vererger. Gevolglik is verskeie strategieë vir die vermindering van die effek van die wind geformuleer, waarvan die installasie van poreuse perifere windskerms wat langs en onder die buitegrense van 'n ACC-waaierplatform ingesluit is. Die voordeel van 'n perifere windskerm is egter nie algemeen bekend nie en die beskikbare literatuur rondom die impak daarvan is teenstrydig. Sommige studies dui daarop dat windskerms 'n toename in die werkverrigting van die waaier teen die buitegrense veroorsaak, terwyl ander die teendeel voorstel, of dat windskerms meestal voordelig is om die las op die lemme te verminder. Hierdie studie het dus onderneem om numeriese tegnieke saam te stel en te verifieer wat gebruik kan word om die meganismes te ondersoek wat die effek van perifere windskerms op beide ACC-waaierprestasie en dinamiese lembelasting bepaal. Die gevolglike numeriese model kopieer 'n eksperimentele ACC-waaierry-toetsfasiliteit en daar word getoon dat dit kwantitatiewe assessering van die waaierry-prestasie-effekte en die kwalitatiewe assessering van dinamiese lembelasting-effekte kan lewer. Vir die eienskappe van die eksperimentele fasiliteit, wat verteenwoordigend is van 'n ACC met 'n lae platformhoogte, dui die model aan dat die installering van die perifere windskerm hoofsaaklik die waaierry-prestasie benadeel. Op grond van die effektiwiteit van die waaierrye, gaan 'n maksimum prestasietekort van 19% (uitgedruk as 'n persentasieverskil relatief tot die geen-skermscenario) gepaard met die installering van 'n windskerm wat 50% van die perifere inlaatarea bedek op 'n platformhoogte windspoed van 6.6 m/s (benaderde volskaalse windsnelheid van 10 m/s). Omgekeerd toon die model dat die perifere windskerm gunstige verlagings bied vir dinamiese lembelasting op die randwaaier. Die vermindering in die waaierry-prestasie word toegeskryf aan die ontwikkeling van 'n laedruk-sone agter die skerms en die gunstige afname in dinamiese lading om meer eenvormige en simmetriese snelheidsprofiele deur die inlaat van die randwaaier te skep. Die effektiewe platformhoogte van die eksperimentele fasiliteitsmodel word aangepas om 'n voorlopige beoordeling van die invloed van die platformhoogte op die windskerm effekte aan te bied. Gevolglik blyk dit dat die lembelasting van die windskerm grootliks onafhanklik van die hoogte van die platform is, terwyl die prestasie-effekte van die waaier 'n duideliker afhanklikheid vertoon. Dit

word duidelik dat 'n gunstige verbetering van die waaierry-werkverrigting gekry word sodra die skerm en die platformhoogte die versnelde vloeigebied, wat onder die skerm vorm, langs die waaier ry heeltemal kan wegbuig; 'n scenario wat makliker gerealiseer kan word by laer windsnelhede met hoër platformhoogtes. Die numeriese tegnieke wat in hierdie studie beskryf en bekragtig is, is goed geposisioneer om in toekomstige windeffek-simulasie studies gebruik te word, veral op volskaalse simulasie.

Acknowledgements

A huge thank you to my supervisors Dr Michael Owen and Dr Jacques Muiyser. I am very privileged to have had your guidance and support during this project. I so appreciate all your contributions and enthusiasm towards my work. It has been a terrific experience working with you guys.

To all my family and Christina, your support and encouragement made all the difference; you are all so wonderful!

To Howden Netherlands B.V and the National Research Fund (NRF) for their financial contribution.

This work is based on the research supported, in part, by the National Research Foundation of South Africa (Grant numbers: 118040).

Dedication

Rudolph Venter
(1940 – 2018)

Table of contents

List of figures

List of tables

Page

Nomenclature

Abbreviations

ACC	Air-cooled condenser
ADM	Actuator disk method
CFD	Computational fluid dynamics
EADM	Extended actuator disk method
FAS	Full approximation storage
FMG	Full multigrid
FSI	Fluid structure interaction
GCI	Grid convergence index
PJM	Pressure jump method
RANS	Reynolds averaged Navier-Stokes
RMS	Root mean square
RR	Radius ratio

Variables

a	Coefficient of influence
	Polynomial coefficient
A	Area
c	Airfoil chord
	Absolute velocity component
C	Constant
C_d	Drag coefficient
C_l	Lift coefficient
c_p	Specific heat at constant pressure
C_2	Inertial resistance
	Turbulence model constant
C_μ	Turbulence model function
d	diameter
D	Deformation tensor
	Hydraulic diameter
g	Gravitational acceleration
F	Force
G	Production term

H	Fan platform height
h_o	Stagnation enthalpy
H_s	Windscreen height
k	Turbulent kinetic energy
K	Loss coefficient
L	Dimensionless windscreen height
L_{ws}	Windscreen material dimension
$\dot{m}$	Mass flow rate
M	Bending moment
M_D	Dynamic bending moment
M_D^*	Nominal dynamic bending moment
M_p	Peak bending moment
M_p^*	Nominal peak bending moment
M_R	Resultant bending moment
M_R^*	Nominal resultant bending moment
N	Revolutions per minute
N_θ	Number of circumferential positions
N_b	Number of blades
N_f	Number of fans
P	Pressure
Q	Heat transfer
r	Spatial co-ordinate
Re	Reynolds number
Re_{y+}	Turbulent wall-based Reynolds number
R^2	Coefficient of determination
S	Source term
	Modulus of the mean strain rate tensor
S_m	Body force Source term
t	Time
	Thickness
T	Temperature
U	Local blade velocity
U^*	Turbulence model function
v	Velocity
V	Volume

$\dot{V}$	Volumetric flow rate
v_x	Average cross-flow beneath fan platform
w	Relative velocity component
W	Work
x	Spatial co-ordinate
y	Spatial co-ordinate
y^+	Dimensionless cell height from wall
z	Spatial co-ordinate

Greek symbols

α	Angle of attack
α_{sm}	Windscreen material face permeability
β	Dimensionless cross-flow
γ	Relative flow angle
δ	Incremental
δ_z	Mean velocity difference
δ_{ij}	Kronecker delta
Δ	Difference
ε	Dissipation rate of turbulent kinetic energy or dynamic strain
ϵ	Material solidity
ζ	Volumetric effectiveness
η	Turbulence model variable
θ	Spatial co-ordinate
μ	Dynamic viscosity
π	Shear stress
Π	Stress tensor
ρ	Density
σ	Blade solidity
σ_ε	Turbulence model constant
σ_k	Turbulence model constant
ν	Kinematic viscosity
ϕ	Flow quantity
ψ	Discretization scheme blending factor
ω	Angular velocity
Ω	Strain rate tensor

Subscript

act	Actual
amb	Ambient
cf	Cell face
CFD	Numerical
d	Dynamic
EXP	Experimental
f	Fan
h	Horizontal
hex	Hex-core
i	Numerical index; 1,2,3…
in	Inlet
j	Numerical index; 1,2,3…
k	Turbulent kinetic energy
	Numerical index
l	Leeward
n	Node index
nw	No wind
p	Node index
r	Radial
ss	Static-to-static
sys	System
tip	Blade tip
t	Turbulent
	Total
ts	Total-to-static
w	Windward
ws	Windscreen
z	Axial
θ	Circumferential
	Tangential
ε	Turbulent dissipation rate
1,2,3	Spatial co-ordinates

1 Introduction

1.1 Background and motivation

Thermoelectric power plants convert thermal energy to mechanical work for the purpose of creating electrical power. In Rankine cycle thermoelectric power plants, high pressure steam is expanded over a turbine and any thermal energy not converted to mechanical work must be rejected to the environment. Cooling systems are accordingly utilized to condense the turbine exhaust steam and any reduction in heat transfer capacity of the cooling system translates into increased turbine backpressure and, correspondingly, reduced electrical output (Kröger, 2004). Cooling systems are thus a key feature affecting overall plant efficiency but, concerningly, predominant wet re-circulatory and once-through cooling methods are highly water-intensive, accounting for 85% to 90% of total plant water usage (DiFilippo, 2008).

A water-conservative alternative is offered through the use of direct-coupled dry-cooling systems that employ mechanical draft air-cooled condensers (ACCs). Mechanical draft ACCs (hereafter referred to as just ACCs) consist of a number of heat exchanger fan units, as shown in Figure 1, typically arranged in horizontal, rectangular arrays. Low pressure steam from the turbine exhaust is routed to the ACC units via the steam-header manifold. Thereafter, steam feeds into inclined finned-tubes and condenses by discharge of heat to the ambient air that is directed over the tubes by a large axial flow fan, thereby effectively eliminating the use of water for cooling purposes.

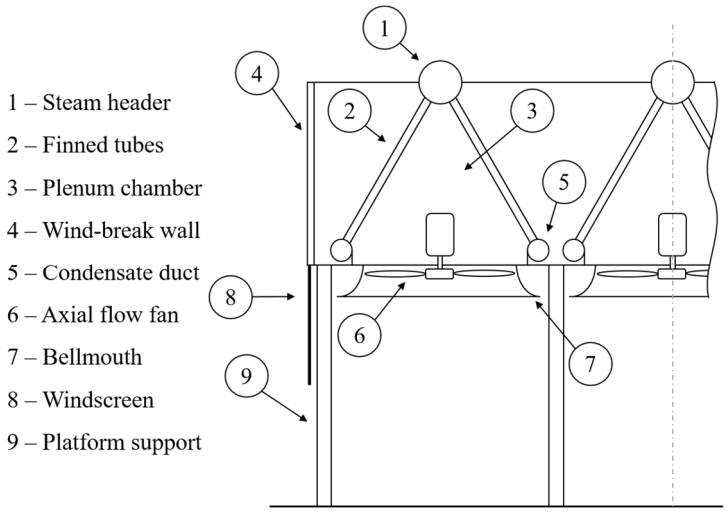

Figure 1: ACC unit schematic

ACCs, therefore, offer significant water-saving potential; however, they are often disparaged due to inefficient operation and high operating and capital costs (EPRI, 2004). Consequently, in the USA, only 1% of thermoelectric power plants employ dry-cooling as the option of heat sink (Bustamante *et al.,* 2015). Cost-disadvantages of ACCs arise due to the poor thermophysical properties of air and the sensitivity of the systems to ambient conditions (Kroger, 2004). ACCs demand large fan installations to compensate for the low density and specific heat of air, resulting in a high percentage of parasitic energy use (EPRI, 2004). When subjected to unfavourable ambient conditions, ACCs can suffer a reduction in heat transfer capacity in excess of 10% (Gadhamshetty *et al.*, 2006), translating to reductions of 3%-11% in electrical output (Byers *et al.*, 2014). The capital cost of an ACC can, therefore, amount to three times that of an equivalent wet-cooled system and operating costs are typically double (EPRI, 2004), all while offering a comparative average annual loss of 2% in energy production (Thopil and Pouris, 2016).

However, in addition to the water-saving advantages, the use of air as the cooling medium awards power plants much greater locational flexibility, as the constraint of having to be near a water source to service a wet-cooled condenser is lifted. ACCs are therefore particularly complementary to concentrated solar power (CSP) technologies which typically find application in arid regions where water is scarce (Moore *et al.*, 2014). From this viewpoint, ACCs are championed as a potential contributor to assisting in achieving renewable energy targets, such as those outlined in the EU's Strategic Energy Tech (SET) plan (Moore *et al.*, 2014).

Furthermore, ACCs are free from the environmental drawbacks that typically accompany wet-cooled methods, allowing plant developers to profit off shortened licensing periods (EPRI, 2012). Notably, concerns over threatening environmental impacts have even led to the prohibition of once-through cooling systems in California, USA (Rao *et al.* 2017). Hence, environmental regulations may promote the use of dry-cooling systems even in areas outside of water-short regions (EPRI, 2012).

These aspects are promoting the use of ACCs, but they remain an unpopular option of heat sink in thermoelectric power plants (Moore *et al.*, 2014). The reluctance of industry to adopt ACCs as the preferred choice of cooling method justifies the need for continued efforts to lessen the undesirable aspects that are stalling their widespread adoption.

Maulbetsch *et al.* (2011) recognize the effects of wind to be the most significant challenge facing ACC performance. Wind has a deleterious effect on fan performance, causes re-entry of the hot exhaust plume through the ACC unit inlets (thereby increasing the effective cooling air temperature) and imposes stresses on the mechanical elements (Maulbetsch and DiFilippo, 2016). Consequently, multiple wind effect mitigation strategies have been formulated, of which one common implementation is the installation of porous and solid windscreens beneath the ACC fan platform, as illustrated in Figures 1 and 2.

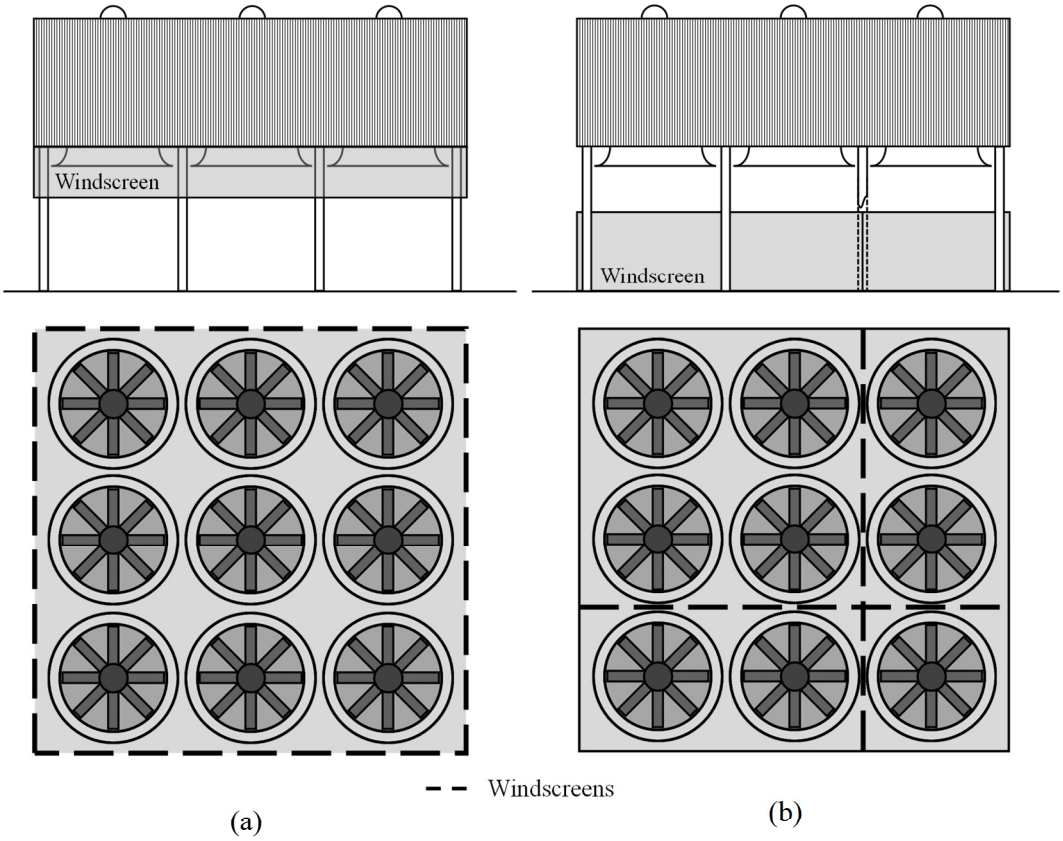

Figure 2: Windscreen arrangements beneath ACC fan platform (side and bottom view): (a) Peripheral-type (b) Cruciform-type

However, little is known about the mechanisms that determine the effect of the windscreens on ACC performance, and there exists considerable uncertainty in the literature regarding the benefit of this measure (as reviewed in Section 2). Therefore, in the attempt to contribute to the collective efforts geared at positioning ACCs as the preferred choice of cooling system in thermoelectric power plants, this study undertakes to partially settle the uncertainty in the literature regarding the impact of porous peripheral-type (Figure 2(a)) windscreens on ACC fan performance. Additionally, this study will contribute to the sparse understanding of cross-flow and windscreen effects on ACC fan blade loading. Determination of the beneficial or harmful impact of peripheral windscreens will allow thermoelectric power utilities to make more informed decisions on how to best configure their ACCs for optimal, more efficient operation.

1.2 Problem statement and scope

The inconsistency in the literature (outlined in Section 2) surrounding the impact of porous windscreens on ACC performance raises suspicion regarding the validity of some of the existing numerical techniques used to investigate their effect. Maulbetsch and DiFilippo (2016) attest that this is due, in part, to the lack of consistent field and/or experimental data against which these prior models could be concretely validated.

In recognition of this deficiency, Marincowitz (2018) modified an experimental fan row test facility to incorporate peripheral windscreens and a controllable cross-flow (wind) induction capability, with a motivation to remedy the lack of experimental data against which a numerical model can be validated. The requirement of this study is to now use the experimental data of Marincowitz (2018) to validate numerical techniques that can be confidently used to provide insight into the mechanisms that determine the effects of windscreens on ACC fan performance and blade loading.

The experimental facility and test cases of Marincowitz (2018) are to be replicated numerically through the use of computational fluid dynamic (CFD) simulations, using available implicit fan and windscreen modelling techniques (discussed in Section 3). Validation of the techniques will be based on the agreement of the resultant model with the experimental results and once validated, an attempt to provide insight into the mechanisms that determined the phenomena witnessed in the experimental analysis will be made. Additionally, whereas the experiment was limited to a fixed platform height, the platform height in the numerical model will be modified to consider its related effect. The scope of the analysis here is limited to the experimental facility, so as to enable the construction of a model capable of delivering results within a high degree of confidence, albeit in a limiting scenario. The promised product of this study is a comprehensively evaluated modelling approach that can be potentially extended into further windscreen effect analysis iterations, particularly, full-scale analysis.

1.3 Objectives and research methodology

The above broad problem statement can be broken up into the following specific sequential objectives, which also outlines the methodology followed in this study.

i. Creation and verification of key component models

Candidate numerical modelling techniques for the representation of the axial flow fans and the windscreens will be compiled and trialled. The correct construction and numerical implementation of the axial fan models will be verified through single fan installation simulations (Section 4). The capabilities of the fan models to replicate the relevant fan's static pressure rise characteristics will be assessed in this verification process. Options to numerically model the porous windscreens will

likewise be explored and tested. All numerical simulations will be executed using the commercially available CFD code, ANSYS Fluent version 18.1, licensed through the University of Stellenbosch. ANSYS Fluent is a widely recognized CFD code and its use for ACC simulation has been successfully proven in previous studies (Bredell *et al.*, 2006; van der Spuy, 2011).

ii. Creation and validation of the experimental test facility model

The multiple fan installation and windscreen test facility as used by Marincowitz (2018) will be numerically replicated and simulated. The candidate component models compiled in the previous activity will be trialled for use in these simulations. Component model appropriateness will be gauged based on accuracy relative to computing expense and the time required to construct the needed numerical infrastructure. Following the selection of the component models, the experimental test cases, performed by Marincowitz (2018), will be reproduced. Where possible the numerical results will be presented in conjunction with their experimental counterparts in an effort to continuously augment the validation of the resultant CFD model.

iii. Assessment of cross-flow and windscreen effects on fan performance and blade loading

The effects of cross-flow, windscreen material porosity and windscreen height on fan performance and dynamic blade loading will be evaluated. The numerically determined data will be analysed to provide insight into the mechanisms that determined the effects witnessed in the experimental analysis. Following replication of the experimental test cases, the influence of windscreens in conjunction with the influence of changing platform height will be assessed to establish a sense of the generalizability of the experimental results.

The structure of this report that serves to detail the execution of the above objectives is outlined in the flow diagram of Figure 3.

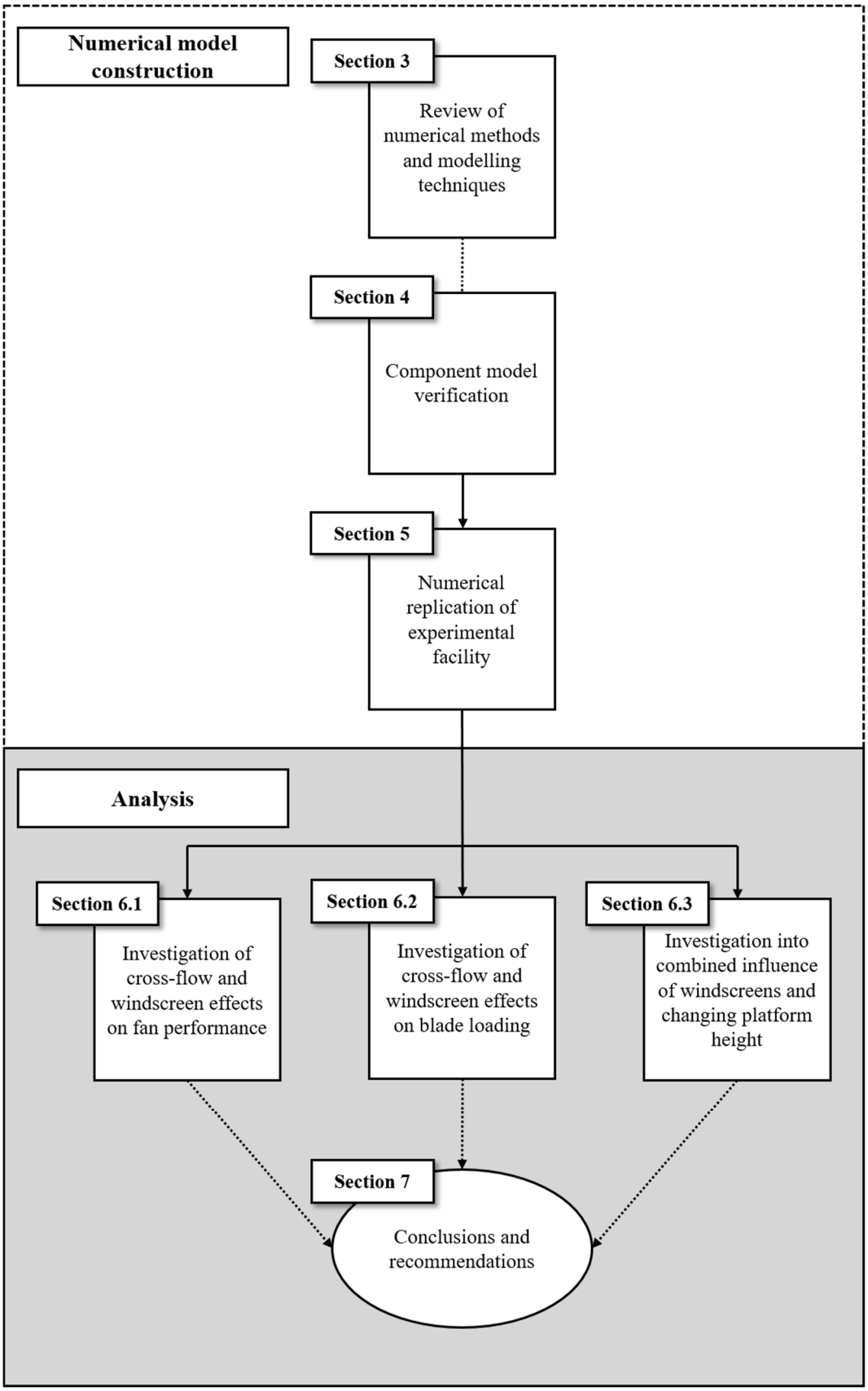

Figure 3: Report flow-diagram

2 Literature review

This section details the relevant literature necessary to formulate a thorough understanding of the present study and its motivations. In order to balance breadth and depth of coverage while remaining within the scope of this study, only a pedagogical review of the common known effects of wind on ACC performance is presented, followed by a review of the literature pertaining to trialled wind effect mitigation measures (with particular emphasis placed on porous windscreens) and a review of the experimental facility which this study numerically replicates.

2.1 Performance metrics

In the subsequent subsections, fan and thermal (ACC) performance are frequently mentioned. If not otherwise stated, fan performance can be considered to refer to volumetric effectiveness, ζ, which equates the actual volume flow rate of air through the fan, $\dot{V}_{act}$, relative to the volume flow rate under 'ideal' inlet conditions, $\dot{V}_{ideal}$ (absence of inlet flow distortions), as described by Equation 2.1.

$$\zeta = {\dot{V}_{act}}/{\dot{V}_{ideal}} \tag{2.1}$$

while thermal performance or heat transfer capacity is captured by Equation 2.2 (Çengel and Cimbala, 2014).

$$\dot{Q} = \dot{m} c_p \Delta T \tag{2.2}$$

where $\dot{Q}$, $\dot{m}$, c_p, ΔT are respectively the heat transfer rate, mass flow rate, specific heat of the air and temperature change between the inlet and outlet of the ACC unit. Thermal performance is referenced to in instances where both air mass flow rate (fan performance) and air inlet temperature are considered.

2.2 ACC wind effects

Duvenhage and Kröger (1996) categorized the effects of wind on the thermal performance of ACCs into two coupled categories, namely plume recirculation and fan performance degradation. In addition to thermal performance deterioration, wind causes excessive fan blade vibrations which leads to physical damage of the ACC structures and mechanical components (Maulbetch and DiFilippo, 2016). The following subsections briefly elaborate on each of these identified effects.

2.2.1 Plume recirculation

Plume recirculation entails the re-entry of the hot exhaust plume into the ACC units' inlets, which increases the effective cooling air temperature and diminishes the ACC's heat transfer capacity (Duvenhage and Kröger, 1996). When subjected to

wind, the hot plume is entrained in vortex structures expanding downwind from the leading edge of the ACC (Owen, 2010).

Owen and Kröger (2011) found through numerical investigation that the effect of plume recirculation increases with wind speed and is most pronounced along the edge and downwind units in an ACC array. Maulbetsch *et al.* (2011), however, experimentally indicated that the effect is most severe at moderate wind speeds, after which the inlet temperatures tend to drop to a lower level. Owen and Kröger (2013) later attributed this discrepancy to the involvement of atmospheric temperature profiles; however, even at high wind speeds, the effect remains to increase the inlet temperature above the low or no wind level.

2.2.2 Fan performance degradation

The more prominent contributor to reduced ACC performance is that of fan performance degradation (Maulbetsch *et al.*, 2011). The reduction in fan performance is due to the distortion of the flow at the entrance of the ACC unit inlets, which is accompanied by a reduction in fan volumetric flow rate (Stinnes and Von Backström, 2002).

These distortions are due to off-axis inflow (Stinnes and von Backström, 2002) and flow detachment around the fan shrouds (Meyer, 2004), as illustrated in Figure 4. In the absence of wind, inner fans of an ACC array induce a cross-flow velocity component across the periphery fans, which is subsequently exacerbated under windy conditions (Stinnes and Von Backström, 2002). Peripheral fans are, therefore, likely to be subjected to both separated and off-axis inflow losses, while interior fan losses are primarily due to off-axis inflow alone (Hotchkiss *et al*., 2006).

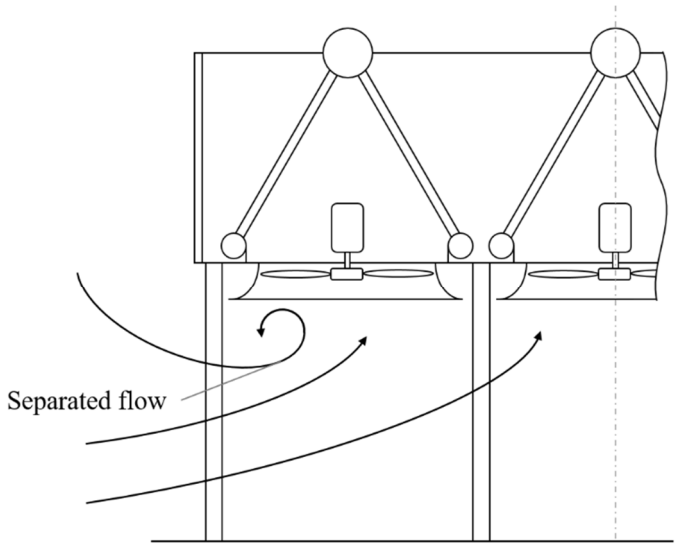

Figure 4: Illustration of the inlet flow distortions beneath an ACC fan platform

Hotchkiss *et al*. (2006) uncovered a dependency between fan total-to-total pressure rise and off-axis inflow angle. They numerically determined a proportional reduction due to greater energy dissipation through the fan, while noting that static-to-static pressure rise is independent of inflow angle.

2.2.3 Blade loading

Whereas the previously addressed thermal performance effects are well documented and understood, research on the effects of wind on ACC fan blade loading is still in its infancy (Muiyser, 2016). Off-axis inflow and flow separation at the fan inlets introduces an asymmetry to the flow's angle of attack and induces varying velocity and pressure distributions on the fan blades as they rotate (Heinemann and Becker, 2017). This azimuthal dependence causes fluctuating mechanical loads on the fan blades and attached mechanical structures.

Through numerical simulation of a single ACC fan row in which the degree of cross-flow could be changed by alteration of the platform height, Bredell *et al.* (2006) found that when exposed to distorted inlet flow conditions, the blade bending moments could exceed steady loading conditions by 70%. Furthermore, the maximum bending moments were found to occur when the blades passed the windward side of the fan casing (Bredell *et al.*, 2006). It was concluded that wind is therefore accompanied by additional threats of blade fatigue and failure (Bredell *et al.,* 2006).

Hotchkiss *et al.* (2006) numerically investigated, in part, the effect of off-axis inflow on blade loading in isolation (absence of separated flow effects) and found the variation of blade thrust and torque to increase with increasing inlet flow angle (up to the maximum investigated case of 45°). Hotchkiss *et al.* (2006) reported a consistent finding with Bredell *et al.* (2006), identifying the maximum bending moments to occur in the upwind position.

Muiyser (2012) carried out strain gauge measurement on a full-scale fan during operation and was able to extract the aerodynamic loading from the measured data. Good correlation with the work of Bredell *et al.* (2006) was found. The increase in average loading with increasing cross-flow was attributed to the corresponding reduction of air flow through the fan. As the flow rate through the fan is reduced the fan static pressure increases, which can be assumed to be proportional to loading (Muiyser, 2012). Muiyser (2012) also observed a proportional dependence between cross-flow and the dynamic component of the loading. Muiyser (2016) next confirmed this observed relationship through laboratory measurements. The same observation was noted by Maulbetsch and DiFilippo (2016) and both investigations attributed the increase in dynamic loading to increased non-uniformity of the inlet air velocity with increasing wind speed.

Heinemann and Becker (2014) experimentally estimated the influence of cross-flow (wind) on blade vibration using Laser Scanning Vibrometry (LSV)

measurements. They found that the harmonics of the rotation frequency, especially the blade pass frequency, were excited strongly in reaction to wind and determined that vibration was more significant at lower fan flow rates.

Heinemann and Becker (2017) later used the same experimental facility and LSV techniques to compare measured spatial and spectral blade vibration distributions to numerical modal analyses. The findings were consistent with their previous study and they noted that there was no significant amplification of the fan's natural frequencies under the influence of cross-flow.

2.3 Wind effect mitigation measures

2.3.1 Overview of wind effect mitigation measures

Several approaches that attempt to mitigate adverse wind effects have been investigated. This subsection highlights some of these established and proposed practices.

It is well known that more favourable flow conditions accompany the elevation of the ACC fan platform height (Salta and Kröger, 1995; Bredell, 2005; van der Spuy 2011; Fourie, 2014). This favourable influence on system (all units) volumetric effectiveness, as experimentally determined by Salta and Kröger (1995), is depicted in Figure 5. Fourie *et al.* (2015) noted that increased cross-wind and reduced platform height have a similar influence on ACC performance. The promotion of system volumetric effectiveness with increasing platform height is attributed to the increase in peripheral inlet area and the subsequent deceleration of the inflow, which leads to lesser maldistribution of the air at the fan unit inlets.

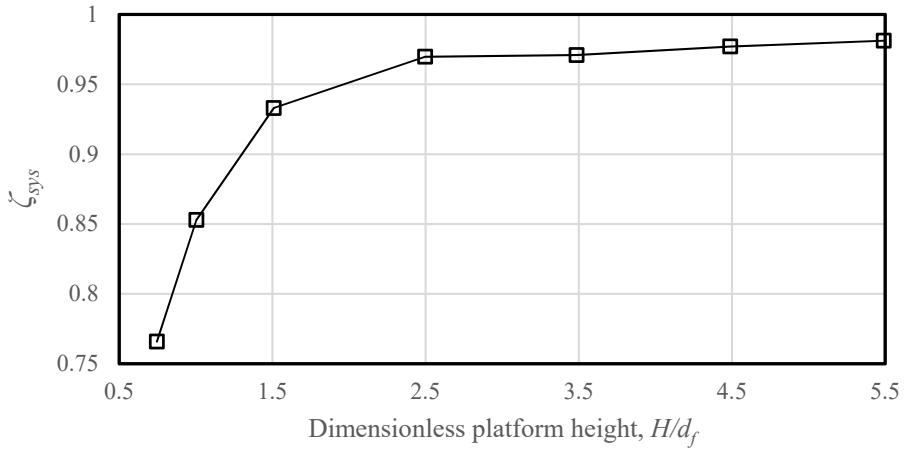

Figure 5: Effect of platform height on ACC system volumetric effectiveness (Salta and Kröger, 1995)

The beneficial influence of a horizontal walkway installation around the perimeter of an ACC is also well known (Meyer, 2004; Bredell, 2005; Owen, 2010). Owen (2010) numerically indicated that the walkway shifts the low pressure region associated with flow separation at the entrance of the ACC platform further upstream, as shown in Figure 6. Consequently, a smaller portion of the upwind fans is exposed to separated flow effects, resulting in increased flow rates through the peripheral fans and, subsequently, enhanced system performance.

Gao *et al.* (2010) propose the installation of deflector plates beneath the fan platform to guide airflow and promote windward peripheral fan performance, also shown in Figure 6. They numerically showed that the plates promise significant enhancement of the mass flow rate through peripheral fans over a range of wind conditions.

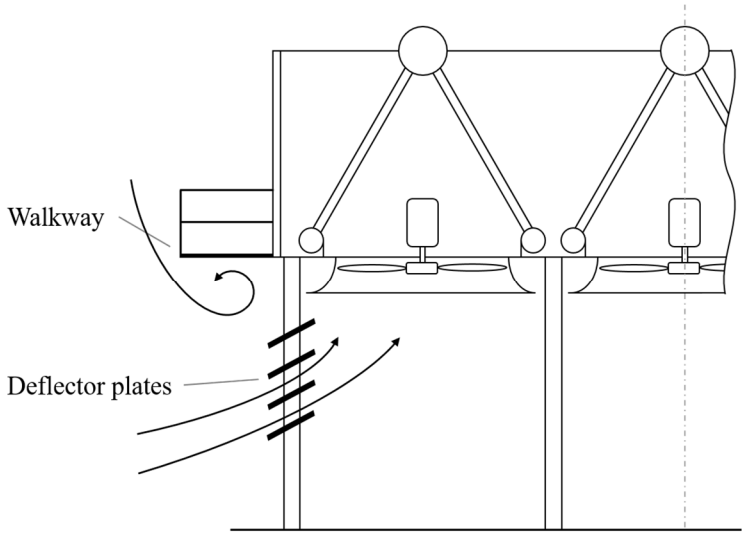

Figure 6: Illustration showing the influence of wind effect mitigation strategies (alternatives to windscreens) on the upstream inlet flow condition

Using numerical methods, Liu *et al.* (2009) detail a proportional reduction in plume recirculation with increasing elevation of the wind-break wall. This favourable effect is attributed to the lengthened distance the hot exhaust plume must travel to re-enter the ACC unit inlets.

Yang *et al.* (2011) numerically investigated both the influence of extending walkway width and wind-break wall elevation on ACC performance. They found that while both measures prove beneficial, the extension of the walkway width offers superior improvements under windy conditions. This is consistent with the understanding that the effect of fan performance degradation is more prominent than plume recirculation.

Kong *et al*. (2017) propose an alternative circular ACC unit arrangement to replace the conventional horizontal, rectangular arrays. They numerically determined that their proposed arrangement effectively alleviates the occurrence of plume recirculation and is capable of achieving lower turbine back pressures than the conventional configuration. Chen *et al.* (2016) propose a vertical arrangement to address the inherent cross-flow across peripheral fans of conventional ACCs. They numerically determined that their novel arrangement enhances performance due to weakened inlet flow distortions and reversed flow in both the presence and absence of wind. Furthermore, Yang *et al.* (2012) recommend the use of a trapezoidal arrangement over conventional ACCs, suggesting the arrangement offers a marginal reduction of the adverse wind effects.

Poullikkas *et al.* (2013a) noted that conventional fixed speed ACC fans are unresponsive to changing ambient wind conditions. Poullikkas *et al.* (2013b) subsequently performed a cost-comparative assessment of using modular air-cooled condensers (MACCs) in place of conventional wet and dry-cooled condensers. MACCs use multiple variable speed fans instead of the typical single, large-diameter fixed or limited speed fans. This allows variation of the condenser operating point and, hence, continuous maximization of efficiency (Moore *et al.,* 2014). Poullikkas *et al.* (2013b) concluded that, given certain parameters, MACCs can be a cost-competitive alternative.

2.3.2 Porous windscreens

Bredell (2005) numerically modelled a single ACC fan row and, in part, considered the effect of combining the, previously mentioned, beneficial walkway installation with porous screen attachments. Bredell (2005) determined that a vertical screen extending down from the peripheral edge of the walkway had a consistent choking effect on upwind edge fan flow.

Van Rooyen (2007) modelled a 30 fan unit ACC subjected to windy conditions and again considered the effect of both a walkway and a porous cruciform-type screen installation on fan performance (similar to Figure 2(b), however, the windscreen covered the full length from the ground to the platform). Van Rooyen (2007) noted that the intention of the screen is to increase the pressure under the upstream fans (fans windward of the screen) and reduce flow passing beneath the fan platform. Considering the case where the ACC was subjected to perpendicular wind relative to its longitudinal axis, and with the screen positioned along the longitudinal axis beneath the fan platform, Van Rooyen (2007) observed that the performance of only the central peripheral fans (fans removed from the longitudinal edges) was significantly improved, while little effect on the remaining fans was apparent. Van Rooyen (2007) therefore suggested that the addition of a screen offers only marginal improvement relative to that of a walkway.

Joubert (2010) modelled the same 30 fan unit ACC of Van Rooyen (2007), using an alternative modelling strategy, and again investigated the influence of the

cruciform-type windscreen installation. Joubert (2010) observed that the screens caused stagnation of the flow beneath the platform ahead of the screens which increased the static pressure and promoted the upstream fans' performance. Joubert (2010), however, also indicated that the screens blocked the flow to the downstream fans, resulting in a low pressure zone beneath these fans and reduced downwind fan performance. Accordingly, Joubert (2010) highlighted that the screens are most effective when positioned towards the rear of the ACC (relative to the incoming wind direction) so that more fans can operate within the beneficial upstream stagnation region.

Owen and Kröger (2010) numerically investigated the influence of the installed porous windscreens at Desert Star Energy Centre's (previously known as El Dorado) ACC. The net effect of the existing cruciform-type screen configuration was found to always enhance the volumetric effectiveness of the ACC under windy conditions. This enhancement was likewise attributed to the more prominent improvement of the flow rate through upwind fans due to stagnation of the flow ahead of the screens. However, it was again observed that the screens have a detrimental effect on the downwind ACC units due to an effective 'suffocation' of those fans.

Louw (2011) numerically investigated the influence of a host of different wind effect mitigation measures on a full-scale ACC and found that screens in a cruciform-type arrangement can offer considerable improvements to fan performance. Consistent reasoning to that given by Owen and Kroger (2010) and Joubert (2010) for the improved performance was provided. A notable difference between Louw (2011) and the previously mentioned cruciform screen investigations is that Louw (2010) considers a screen that only extended across a portion of the length between the fan platform and the ground (similar to that depicted in Figure 2(b)). In this type of arrangement, Louw (2011) suggests the addition of a screen offers greater enhancement to fan performance over the addition of a walkway, contrary to that suggested by van Rooyen (2007).

Zhang and Chen (2015) numerically investigated the influence of a peripheral-type windscreen configuration (Figure 2(a)) on a representative 600MW ACC array (8 x 7). The windscreens covered approximately 15% of the peripheral inlet area and they found the screens to improve the performance of all the peripheral and most of the inner fans irrespective of the wind direction. They dubbed this beneficial influence the 'protection effect' which they suggested is accompanied by a shrinkage of an observed negative pressure region beneath the fan platform. The same beneficial influence was observed in Romano's (2015) numerical simulations of a single ACC unit with a peripheral-type windscreen installation. This beneficial influence, however, opposes the effective 'suffocation' reported earlier in the previously mentioned studies.

Zhang and Chen (2015) also investigated a cruciform-type windscreen arrangement and found this configuration to offer "little performance enhancement or even

adverse impacts at low and intermediate wind speeds," again contradicting the always beneficial effect observed by Owen and Kröger (2010).

WyGen power plant located in Gillette, Wyoming (USA) utilises a solid cruciform-type screen installation and a distinct enhancement in performance has reportedly accompanied its implementation (Maulbetsch and DiFilippo, 2016). The Desert Star Energy Centre's ACC (USA) also employs a cruciform-type screen and an improvement in performance since its installation has likewise been reported (Maulbetsch and DiFilippo, 2016). The peripheral windscreens at Coryton Power Plant in Essex (England) have been reported to benefit performance during periods of high wind speed (> 3 mph), but hamper performance during periods of low wind speed (< 3 mph) (Maulbetsch and DiFilippo, 2016). Ayvazian (2015) reports that a 15-20 MW gain in electrical output has accompanied the installation of the peripheral-type windscreens at Mystic Station, Massachusetts (USA), but noted that the screens are most effective for wind speeds below 20 mph.

Maulbetsch and DiFilippo (2016) conducted field tests over a 16 month period on the peripheral and interior fan of a single interior fan row at Caithness Energy Centre's ACC (6 x 3) in Long Island, New York City (USA). Caithness Energy Centre is a 350 MW gas-fired combined cycle plant in which the ACC is equipped with retractable peripheral windscreens (Figure 2(a)). Their measurements showed that the deployment of the windscreens mostly hindered the peripheral fan's performance, while offering slight improvement of the interior fan at wind speeds less than 8 m/s (velocity at platform height). Additionally, from scaled physical modelling of the ACC they observed that when exposed to windy conditions, the screens created a reduced airspeed region near the fan inlets and extended the high-speed, accelerated flow entering beneath the fan platform further downwind. It was postulated that the reduced airspeed across the immediate vicinity of the fan inlets should encourage greater airflow into the ACC cells and subsequently promote fan performance. The field tests and physical model were further complemented with a numerical model, but accurate representation of the field conditions was only achieved at low wind speeds and no quantitative results or detailed insight into the flow phenomena could be obtained.

It could, however, be deduced from their field measurements that the extension of the windscreens resulted in more uniform inlet velocity profiles, which resulted in a significant reduction of blade loading under windy conditions. This observation of reduced blade loading with peripheral windscreen implementation was also noted by Romano (2015).

2.4 Multiple fan and windscreen test facility

The origin of the facility which this numerical study replicates, traces back to Visser (1990) who designed and built the facility as part of his early investigation into the effects of cross-flow on ACC fan row performance. The facility, shown in Figure 7, consisted of six 630 mm fan test tunnels arranged such that it mimicked a

single internal fan row in an 8 x 6 fan unit array. Visser (1990) reasoned that the incoming flow seen by an internal ACC fan row can be approximated as two-dimensional, allowing the sides of the fan row to be effectively treated as symmetry planes. The assumed symmetry planes were incorporated in the facility by encasing the fan row inlet region with solid sidewalls. Additionally, the ACC upon which the facility was based had a nearby turbine hall situated on the one side and this was accounted for by including another solid wall boundary at the far end of the fan row inlet space. Completing the inlet chamber was an adjustable board which allowed the effective 'floor' height to be altered and the influence of varying platform height and, correspondingly, the degree of cross-flow to be investigated.

Each fan tunnel is based on the ISO 5801 type B testing facility (ISO, 2007). ACC fan units are more closely represented by type A testing configurations. However, the type B format enabled measurement of individual fan tunnel flow rates; therefore, performance could be evaluated based on fan volumetric effectiveness.

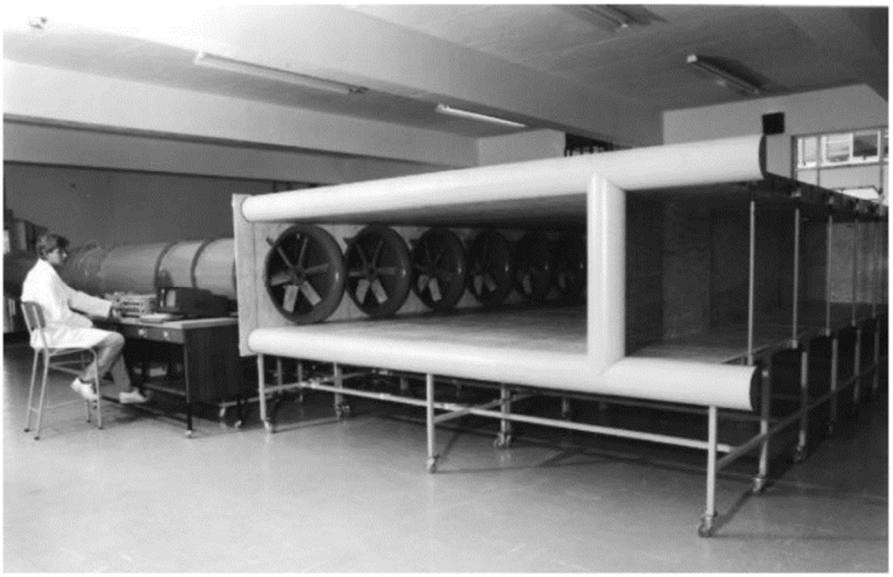

Figure 7: Original experimental facility (Visser, 1990)

Salta and Kroger (1995) later made use of the same facility, followed by Conradie (2010) who implemented several modifications. A notable modification by Conradie (2010) was the reduction of the fan unit number from six to three. Van der Spuy (2011) next used the facility to collect experimental data for numerical fan model validation purposes, during which the fan tunnels were revised to better represent actual ACC installations. This was done by replacing the fan tunnels' flow straightener sections with plenum chambers, fitted with porous mesh sheets. Fourie (2014) likewise used the facility to gather data for validation of numerical axial fan models for use in full-scale ACC simulations.

Finally, Marincowitz (2018) modified the facility further to incorporate the capability to induce a controllable cross-flow component across the fan row at a fixed platform height (necessary to simulate repeatable windy conditions). This was achieved by ducting exhaust flow from an open-loop wind tunnel past the fan row. The constructed ducting that was used to couple the fan row to the wind tunnel outlet is shown in Figure 8. Maricowitz (2018) aimed to replicate an operating ACC for which full-scale data is available at Maulbetsch and DiFilippo (2016). The facility has a dimensionless platform height (H/d_f) of 1.32 and Marincowitz (2018) was able to obtain results that corresponded encouragingly with the full-scale data.

The dimensions of the wind tunnel outlet are 610 x 1205 mm (w x h), while the straightening section (Figure 8) has dimensions of 1250 x 800 mm. The constructed ducting, therefore, had to expand horizontally and narrow vertically to connect the wind tunnel to the fan row.

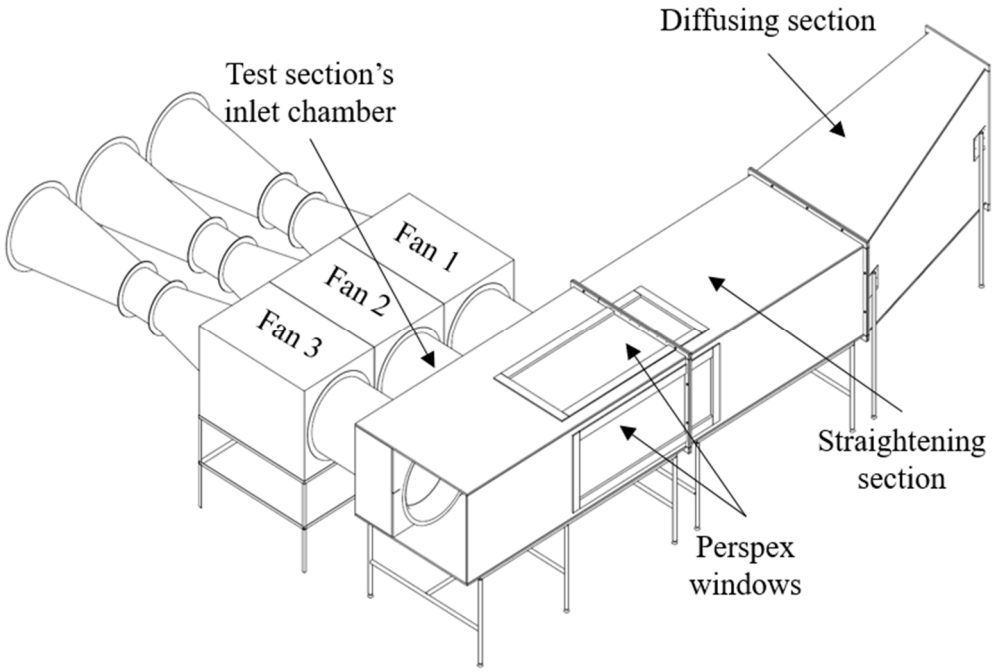

Figure 8: Diagram of the constructed ducting used to route flow from the wind tunnel outlet past the fan row (Marincowitz, 2018)

The straightening section extends across a portion of an effective wind-break wall and the peripheral inlet to the fan row (830 x 800 mm), as shown in Figure 9. Further details of the duct height selection are available in Marincowitz (2018). Modular construction of the different ducting segments allowed for installation and removal of windscreen material at the inlet to the fan row. The fan used during

experimentation was the so-called 630 mm L2-fan with an FX 60-126 airfoil, characteristics of which are detailed in Table 1.

Table 1: 630 mm L2-fan characteristics

Diameter	630 mm
Hub-to-tip ratio	0.15
Number of blades	8
Solidity at mid-span	0.532 (Fourie, 2014)

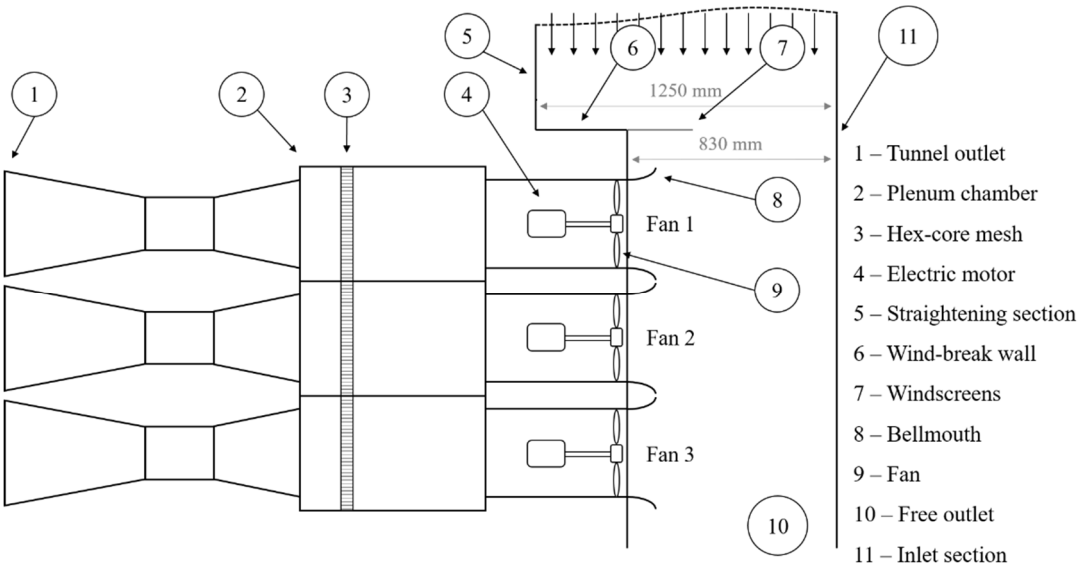

Figure 9: Experimental facility schematic (mid-plane cross-section)

The wind tunnel is able to output a maximum volumetric flow rate of 8.5 m^3/s, which equates to an approximate wind speed of 12.5 m/s at the facility's platform height when no windscreen is present (wind speed calculation is detailed in Section 6). This translates to a full-scale platform height wind speed of approximately 19.2 m/s.

2.5 Summary of the literature review

The information presented within this section highlights that the majority of the ACC wind effect related research is skewed towards thermal performance effects and that the efforts aimed at understanding and mitigating blade loading implications are still juvenile. It is well understood that ACC fan performance is reduced considerably under windy conditions. The mechanisms responsible for this reduction are that of off-axis inflow and flow detachment around the fan shrouds. From the presented investigations, it is also clear that blade loading increases with increasing cross-flow. However, few studies exist that have numerically investigated blade loading effects under forced (high) cross-flow conditions and there is consequently little available information on the aerodynamic mechanisms that are determining this behaviour. This is a shortcoming this study aims to address.

Furthermore, while it appears that the installation of peripheral windscreens may be beneficial to reducing both ACC fan performance losses and fan blade loading, the literature is largely inconclusive. Hence, there is a need for this study to contribute to settling the uncertainty surrounding their effects.

Concrete validation of a numerical model for this purpose is possible with the experimental results available in Marincowitz (2018). Marincowitz's (2018) experimental facility and results enable the validity of numerical modelling techniques to be assessed up to an equivalent full-scale wind speed (at platform height) of 19.2 m/s. Marincowitz's (2018) assessment of windscreen effects was limited as the influence of platform height could not be addressed in his experimental investigation. This study, therefore, aims to extend Marincowitz's (2018) study by factoring platform height variability into the numerical assessment.

3 Review of numerical models

In order to replicate the experimental facility of Marincowitz (2018), methods of numerically modelling the axial flow fans and the windscreens needed to be investigated. This section, therefore, presents a discussion on the background of the numerical fan and windscreen model options available and applicable for use in this study. The discussion here is restricted to the component models; however, further discussion on relevant CFD theory can be found in Appendix A.

3.1 Fan models

The most accurate method of numerically analysing the flow through an axial flow fan is by means of explicit modelling of the fan geometry as solid rotating surfaces (Bredell, 2005). However, this method necessitates large computational grid arrangements and is highly computationally expensive (Meyer and Kröger, 2001; Engelbrecht *et al.,* 2019).

The use of simplified models that save grid complexity and computational effort is therefore motivated (van der Spuy, 2011). Such options include the likes of the pressure jump method (PJM), the actuator disk method (ADM) and the extended actuator disk method (EADM). These methods allow the effect of the fan to be implicitly incorporated into the numerical simulations through the introduction of additional momentum source terms into the computational flow field. Additional implicit methods are detailed in Bredell (2005) and Louw (2015); however, only the named methods, consistent with those described by van der Spuy (2011), are considered in this study.

3.1.1 Pressure jump method

In the pressure jump method (PJM), the effect of the fan is incorporated through a discontinuous static pressure rise applied across the fan's rotation plane (Fluent, 2009). The static-to-static pressure rise corresponds to the velocity through the fan annulus and is added as a per-unit mass source term to the linear momentum equations of the CFD solver in the axial direction (van der Spuy, 2011).

The pressure rise as a function of axial velocity is derived from standard fan total-to-static pressure curves that are converted to static-to-static pressure values (van der Spuy, 2011), conversion requires the addition of the dynamic pressure component and associated losses. A regression is performed on the fan static pressure curve and the resultant polynomial coefficients (which have been changed to static-to-static pressure values) are implemented in Fluent's fan boundary condition on an inter-cell face boundary representing the axial fan location in the flow domain. The axial momentum source terms that are effected in the immediate downstream cells of the applicable surface are described by Equation 3.1 (van der Spuy, 2011).

$$F_{PJM} = \frac{\Delta P_{ss} A_{cf}}{\rho V_c} \tag{3.1}$$

where ΔP_{ss} is the static-to-static pressure rise, A_{cf} is the area of the cell face and V_c the volume of the cell. The derivation of the ΔP_{ss} function for the 630 mm L2 fan used in this study is provided in Appendix B.

This method is simple to implement, does not necessitate any particular mesh structure and can be effectively employed using grids of low resolution (Fourie, 2014). However, the pressure rise is only applied as an axial source term; hence, there is an absence of any induced tangential velocity components downstream of the fan rotation plane and the resultant downstream flow field is not realistic (van der Spuy, 2011), as illustrated in Figure 10 (Figure 10 is compiled using results from the single fan installation simulations discussed in Section 4). The PJM, however, is commonly used for the representation of axial flow fans in ACC simulations and has seen use in multiple prior investigations (Owen, 2010; Joubert, 2010; Fourie, 2014; van der Spuy, 2011; Zheng and Chen, 2015).

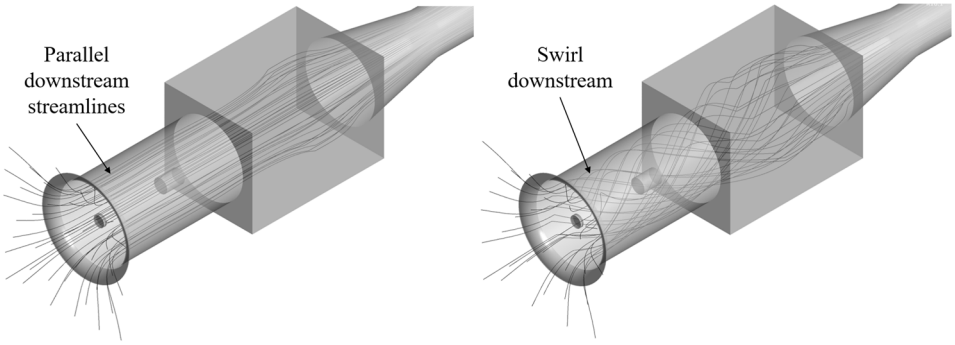

Figure 10: Determined flow pattern through fan tunnel using different implicit fan models: (a) PJM (b) ADM

3.1.2 Actuator Disk Method

The actuator disk method effects the operation of an axial flow fan through a step-change in tangential and axial velocity in the flow field over the fan's plane of rotation (van der Spuy, 2011). The step-change originates from forces calculated using blade element theory, employing lift and drag coefficients determined through two-dimensional, non-rotating isolated airfoil profile tests (Bredell, 2005). The calculated forces are introduced into the flow field as volumetric source terms in the linear momentum equations of the CFD solver (van der Spuy, 2011). The ADM is incorporated through a user-defined subroutine that permits the user to integrate the fan blades' geometric and performance properties into the analysis.

The ADM is implemented using three annular disks of identical grid character. The disks are composed of radial and tangential elements and are manipulated so that each disk is only one cell thick. The three disks are arranged in succession along the fan's rotational axis with the central (rotor) disk coincident with the plane of rotation, as shown in Figure 11. The source terms are introduced at each cell of the rotor disk and are determined using velocity values from the corresponding cells in the up- and downstream disks (Bredell, 2005).

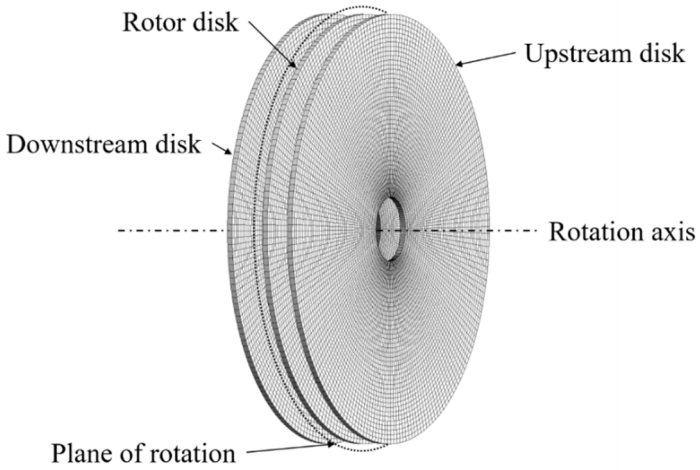

Figure 11: Arrangement of ADM disks

The following derivation of the ADM source terms is taken from Bredell (2005). Consider the isolated two-dimensional fan blade element shown in Figure 12. The associated lift and drag forces at a radius r from the fan rotation axis, as determined in the ADM formulation, are captured by Equation 3.2 and Equation 3.3.

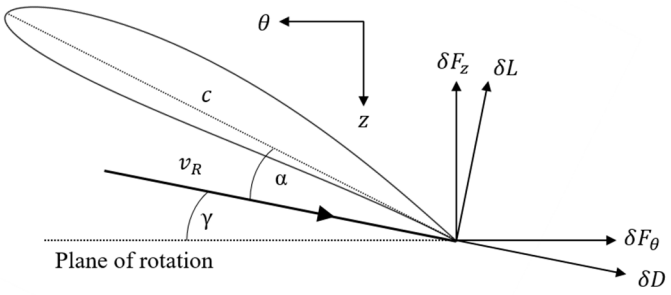

Figure 12: Radial fan blade element

$$\delta L = \frac{1}{2}\rho C_l |v_R^2| c\delta r \tag{3.2}$$

$$\delta D = \frac{1}{2}\rho C_d |v_R^2| c\delta r \tag{3.3}$$

where ρ, c, δr, C_l, C_d, v_R are the fluid density, chord, radial thickness, lift coefficient, drag coefficient and average relative velocity vector respectively. The needed lift and drag coefficients are obtained from polynomial expressions embedded within the ADM code that describe the characteristic data determined through two-dimensional CFD simulation of the fan blade's airfoil. A discussion on the generation of the lift and drag coefficients for the L2-fan used in this study is presented in Appendix C. This process involves iterative simulation of a single airfoil element subjected to impinging flow at a range of anticipated flow angles of attack (α). At each angle of attack, the lift and drag forces on the airfoil element are extracted and processed to obtain the respective coefficients. Polynomials can then be fitted to this data so as to describe the coefficients as a function of α, which are then fed into the ADM's mathematical infrastructure. Use of the average relative velocity vector in Equations 3.2 and 3.3 is consistent with turbomachinery analysis convention and compensates for the difference between the velocity field of an axial flow fan and the uniform field in which the employed lift and drag coefficients are valid (Meyer and Kröger, 2004).

The flow field in which the blade element is submerged experiences equal, opposite forces in response to the relative fan motion and the imparted axial and tangential blade forces are given by Equation 3.4 and Equation 3.5.

$$\delta F_z = \delta L \cos\gamma - \delta D \sin\gamma \tag{3.4}$$

$$\delta F_\theta = \delta L \sin\gamma + \delta D \cos\gamma \tag{3.5}$$

where γ defines the angle between the average relative velocity vector and the plane of rotation (Figure 12). The per-unit volume momentum source term expressions are then given by Equation 3.6 and Equation 3.7.

$$\frac{\delta F_z}{\delta V} = \frac{N_b}{2\pi\delta r t}\delta F_z = \frac{\sigma}{c\delta r t}\delta F_x \tag{3.6}$$

$$\frac{\delta F_\theta}{\delta V} = \frac{N_b}{2\pi\delta r t}\delta F_\theta = \frac{\sigma}{c\delta r t}\delta F_\theta \tag{3.7}$$

where t is the axial thickness of the rotor disk and σ is the blade solidity, which effectively serves as a time averaging factor (Bredell, 2005). Substitution of Equations 3.2 and 3.3 into Equations 3.4 and 3.5, then subsequently into Equation 3.6 and 3.7 yields the complete momentum source term expressions that are introduced into the flow domain. These expressions are given by Equation 3.8 and Equation 3.9 (Bredell, 2005).

$$\frac{\delta F_z}{\delta V} = \frac{1}{2}\rho |v_R^2| \frac{\sigma}{t}(\delta L \cos\gamma - \delta D \sin\gamma) \tag{3.8}$$

$$\frac{\delta F_\theta}{\delta V} = \frac{1}{2}\rho|v_R^2|\frac{\sigma}{t}(\delta L\sin\gamma + \delta D\cos\gamma) \tag{3.9}$$

Thiart and von Backström (1993) investigated the effect of flow distortions for a particular low solidity, low hub-to-tip ratio fan and concluded that the ADM is capable of satisfactorily predicting fan operational trends when subjected to axisymmetric flow. However, Meyer and Kröger (2001) note that the ADM ignores the existence of any radial flow in its formulation. Radial flow and subsequently the Coriolis effect (a resultant chord-wise pressure gradient characteristic of rotating airfoils) are increasingly prevalent at low fan flow rates (Gur and Rosen, 2005). The effect of this radial flow is to modify the airfoil's stall characteristics by delaying boundary-layer separation. Therefore, at low flow rates, the ADM under predicts fan performance due to the unrealistic stall behaviour predicted by the model. Nonetheless, the ADM has been used in multiple prior investigations (Thiart and von Backstörm, 1993; Meyer and Kröger, 2001; Meyer, 2004; Hotchkiss *et al*., 2006) and can be used to investigate fan blade loading, as done by Bredell *et al.* (2006).

3.1.3 Extended Actuator Disk Method

Van der Spuy (2011) formulated the EADM model in an attempt to compensate for the failure of the ADM to accurately account for radial flow effects, characteristic of axial flow fan operation at low volumetric flow rates.

Lindenburg (2004) noted that due to the span-wise rotational velocity variation existing along a rotating blade, a radial variation in relative flow velocity and dynamic pressure exists over the blade. This initiates a centrifugal load on the airflow which establishes an absolute radial flow path and three-dimensional flow in the rotating reference frame of the fan blade. Therefore, the two-dimensional lift and drag characteristics adopted in the formulation of the ADM need to be augmented to incorporate the accompanying three-dimensional effects. Lewis (1996) notes that this three-dimensional flow regime is analogous to flow through a mixed flow fan.

Figure 13 depicts the movement of a fluid particle through a turbomachine as it travels axially from point 1 to point 2 while simultaneously moving from a radius r_1 to r_2. Due to the centrifugal loads, the air moves from regions of low to higher radii with greater tangential velocity during its passage over the fan blades (Louw, 2015). Therefore, the absolute tangential velocity components in the Euler pump equation for an axial flow fan must be re-expressed to capture this radial change.

The following procedure undertaken to re-express the Euler pump equation is taken from Lewis (1996). The Euler pump equation for an axial flow fan is given by Equation 3.10.

$$W = h_{o2} - h_{o1} = U_2 c_{\theta 2} - U_1 c_{\theta 1} \tag{3.10}$$

where W, h_o, U, c_θ are the specific work input, stagnation enthalpy, local blade velocity and absolute tangential velocity component respectively. The tangential velocity components in Equation 3.10 are subsequently re-expressed as shown by Equation 3.11.

$$c_\theta = U - w_\theta = r\omega - w_\theta \tag{3.11}$$

where ω is the angular velocity of the blade and w_θ is the relative tangential velocity. Substitution of Equation 3.11 back into Equation 3.10 results in the Euler pump equation for a mixed flow fan as given by Equation 3.12.

$$W = \omega(r_2 w_{\theta 2} - r_1 w_{\theta 1}) + \omega^2(r_2^2 - r_1^2) \tag{3.12}$$

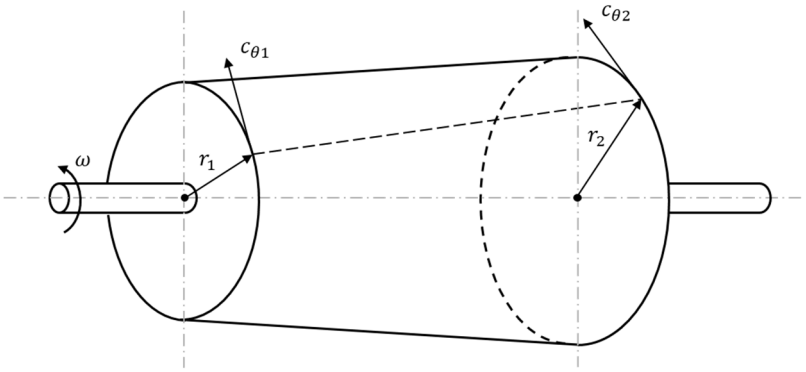

Figure 13: Movement of a fluid particle through a turbomachine (adapted from Dixon (2010))

The alternative expression of the absolute tangential velocity components uncovers the contribution of two separate work input sources. The first term captures the work input due to aerodynamic forces resulting from a change in angular momentum. The second term is dependent solely on the radial shift and is aptly called the Coriolis force (Lewis, 1996). Gur and Rosen (2005) note that the Coriolis force effects a chord-wise pressure gradient which modifies the blade's stall characteristics by delaying boundary layer separation (however, given certain setting angles the Coriolis-force can destabilise the boundary layer (van der Spuy, 2011)). Additionally, radial flow increases the effective chord length of the blade, which alters the effective blade camber and, correspondingly, the blade's lift characteristics (van der Spuy, 2011). Therefore, the presence of radial flow results in greater load exertion by the fan on the flow field (van der Spuy, 2011).

The EADM is formulated by making a slight adjustment to the source term computation in the ADM coding so as to reflect this increased load exertion in the presence of radial flow. Radial flow effects in the EADM are introduced through modification of the lift coefficient polynomial used in the ADM. The linear portion

of the lift coefficient characteristic is extended as shown in Figure 14. Correspondingly, the drag coefficient is proportionately modified using Equation 3.13 (van der Spuy, 2011):

$$C_{d,EADM} = C_{l,EADM}\left(\frac{C_d}{C_l}\right) \tag{3.13}$$

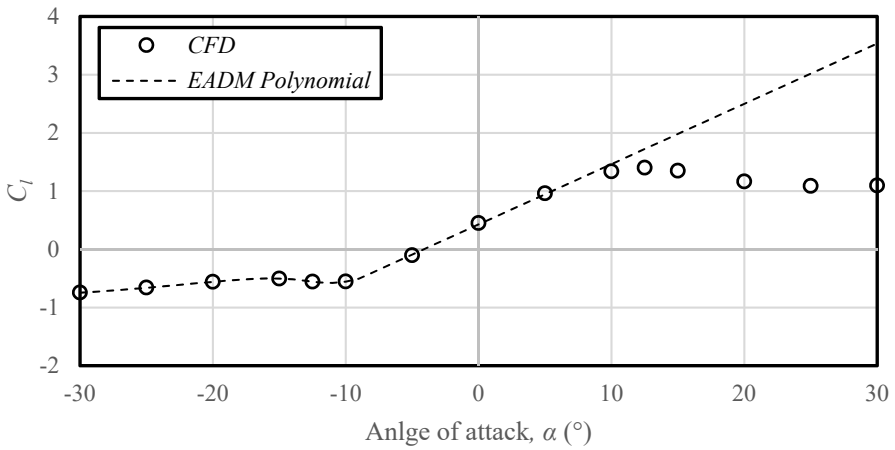

Figure 14: Modification of the EADM fan blade lift coefficient characteristic to account for radial flow effects

The remainder of the EADM formulation and implementation is consistent with the ADM. Extension of the linear portion of the lift coefficient polynomial effectively suppresses the occurrence of stall. The modified lift and drag characteristics are, therefore, only implemented above a set radius ratio (RR) in consideration of the expected presence of stall and reverse flow near the fan's hub, which neglects the augmented lift and drag behaviour. Van der Spuy (2011) suggests a limiting RR of 0.5 for the general case.

The EADM offers a considerable improvement over the ADM in terms of fan characteristic curve prediction, but it still under-predicts performance at low flow rates. This suggests that there are still additional mechanisms associated with low flow rates that the EADM ignores (van der Spuy, 2011).

3.2 Windscreen model

Windscreens or any other porous media can be incorporated into CFD simulations either via explicit modelling or by effecting an equivalent pressure drop in place of the physical structure. Implementation of such implicit pressure drop conditions is achievable in ANSYS Fluent through the use of the porous media model. This model introduces an empirically determined flow resistance into the governing momentum equations as an added sink term (Fluent, 2009). The model can be

applied to an infinitely thin surface or a three-dimensional fluid body. The pressure drop is calculated based on Equation 3.14 (Fluent, 2009).

$$\Delta P = -\left(\frac{\mu}{\alpha_{sm}} v + C_2 \frac{1}{2} \rho v^2\right) \Delta x \tag{3.14}$$

where ΔP is the pressure drop across the zone; ρ the fluid density, μ the dynamic viscosity of the fluid, $1/\alpha_{sm}$ the viscous resistance of the media, C_2 the inertial resistance of the media, Δx the porous zone thickness and v the velocity.

The model parameters for a specific media are derived by fitting second-order polynomials to the respective resistance (pressure loss versus volume flow rate) curves of the porous media. The corresponding coefficients are then equated to determine the needed parameters for input into Fluent's simulation environment. In the case where the model is applied to a surface, the thickness term (Δx) is prescribed into the model specification, whereas for a three-dimensional zone the thickness is set by the dimensions of the zone. The porous media model is referred to as a porous-jump boundary condition when applied to an infinitely thin surface. The pressure drop is applied as a step change and the specified thickness has no effect on the application of the pressure change, only the magnitude. The porous-jump boundary condition was used in all of the windscreen effect investigations discussed in Section 2.

4 Component model verification

The first step to numerically replicating the experimental facility and test cases of Marincowitz (2018) is to construct and test the candidate fan and windscreen model options addressed in Section 3. This is necessary to verify acceptable formulation and implementation into the CFD code. Once verified, the numerical models can be extended and trialled for use in the 'full' experimental facility simulations as discussed in Section 5.

4.1 Single fan installation simulations

In this subsection, the different fan models are evaluated under standard, 'ideal', inlet conditions. The CFD model used in this verification process replicates a single fan tunnel from the multiple fan and windscreen test facility of Marincowitz (2018) in isolation.

4.1.1 Geometry

The fluid domain comprises the inner passages of the single fan tunnel and a 3 x 3 m cubical inlet air space, as shown in Figure 15. Within the fan tunnel, a simplified representation of the fan motor has been incorporated while the fan shaft, supports and detailed surfaces of the motor have been excluded from the analysis. This simulation domain and simplifications are consistent with those adopted by van der Spuy (2011) who modelled the same facility.

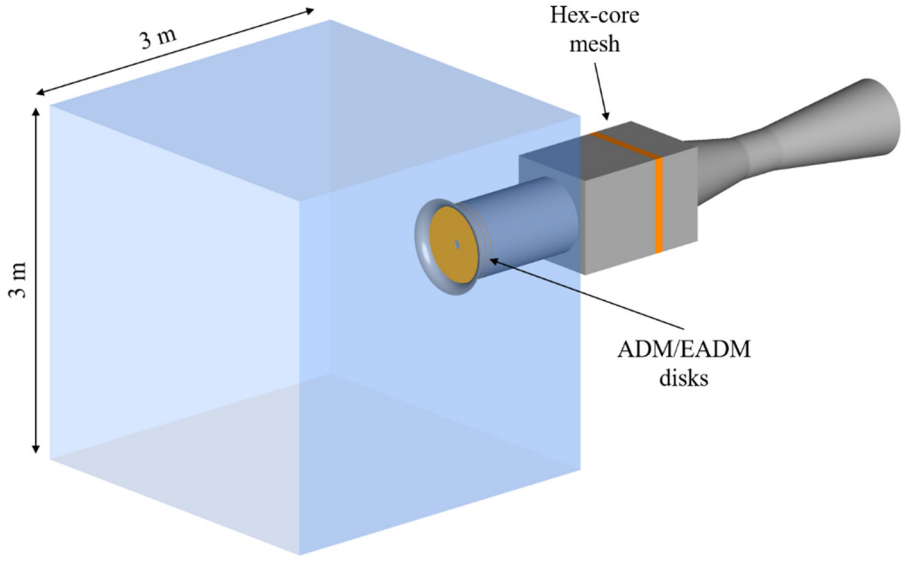

Figure 15: Single fan installation numerical model geometry

While simplification of the fan tunnel features is not expected to affect the determined fan performance, the same cannot be implied for blade loading; as it is known that downstream obstructions can effect blade vibration (Muiyser, 2016). Therefore, confirmation of whether or not the inclusion of these features will affect the blade loading results was sought and a discussion thereof is given in Appendix D. Resultantly, no change to the determined blade loading was suspected to accompany inclusion of these features and the simplified fan tunnel representation was favoured, as it allowed for the use of simpler mesh structures.

4.1.2 Meshing

All meshing was performed using ANSYS Meshing, available within the ANSYS workbench suite. The same mesh is used in the investigation of each candidate fan model. The PJM does not necessitate a particular mesh structure so the mesh was generated to satisfy the requirements of the ADM and the EADM.

Local sizing functions were used to construct the structured grid domains of the ADM disks. The ADM disks were meshed according to the specifications used by van der Spuy (2011). The disks were set to have 200 circumferential elements, 40 radial elements and one cell thickness of 8 mm each. The cells in the annular regions between the rotor and the up- and downstream disks were specified to continue the structured format of the disks. The spacing between the disks match the recommendations as prescribed by van der Spuy (2011). The upstream disk was set $0.43c$ forward of the rotor disk, while the downstream disk was $0.66c$ aft of the rotor disk (where c is the fan blade chord).

The original geometry was adapted to include a secondary body enclosing the bellmouth inlet, allowing the use of a body of influence sizing function around the fan inlet. The body of influence sizing function allowed the element size surrounding the immediate vicinity of the fan inlet to be limited while not suppressing the additional local meshing functions applied to the walls of the bellmouth. The element size in the body of influence was set to change in accordance with neighbouring mesh structures so that a smooth outward expanding element size gradient could be established in the area around the fan inlet.

Local uniform body sizing functions were applied to the unstructured tetrahedral sections of the fan tunnel, downstream of the ADM disks. The geometry was modelled as an assembly of multiple bodies (domains) grouped together to form a single part. Conformal boundaries between the different mesh sections could therefore be established and selective body meshing was used to ensure the correct grid structures between the various domains.

The mesh quality was set to a target skewness of 0.7 with high smoothing functionality enabled, resulting in a mesh of 3.6 million elements with a mixture of both hexahedral and tetrahedral cells. The quality of the mesh was deemed acceptable in accordance with the guidelines stipulated in Fluent (2009). Grid

sensitivity was also deemed acceptable, the details of which are given in Appendix D.

All sizing and inflation layer specifications were chosen to correspond closely to those used by van der Spuy (2011). Instances in which markedly different cell structures or sizings were used originated with the intent to improve the cells' orthogonal quality and skewness. The number of mesh elements is significantly more than that of van der Spuy's (2011) 1.4 million cells due to the use of conformal boundaries between the different mesh domains. Van der Spuy (2011) stitched the various domains together using unmatched boundaries. Initial simulations, however, showed that using a mesh with unmatched boundaries resulted in steps in variable contour plots across the domains. While this won't affect volumetric fan performance, the desire to extract detailed loading profiles on the rotor disk meant that these inconsistencies between mesh domains were not acceptable, and this issue was eradicated through the use of the conformal boundaries. Figure 16 shows a mid-plane cross-section through the resultant mesh, as well as some of the fan tunnel features and the applicable boundary conditions which are discussed in the next subsections.

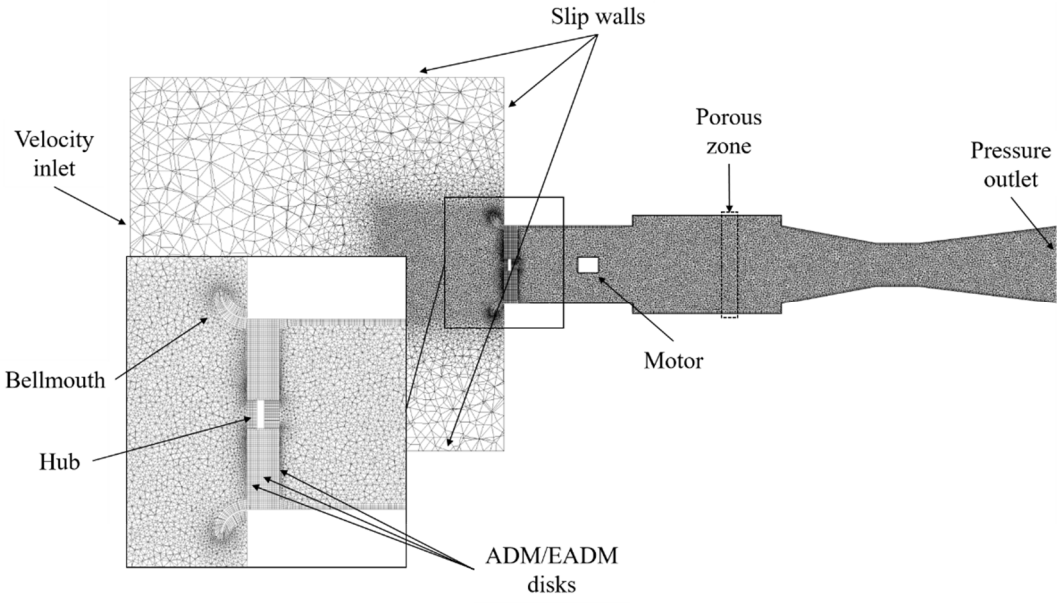

Figure 16: Cross-section of the single fan installation model mesh through a central plane

To allow parallel processing capabilities to be utilized when using the ADM/EADM models, the mesh was divided into six partitions such that the structured, annular disks were grouped into 1 partition. The disks need to be contained in one partition so that a single processor can access the upstream and downstream disk cell velocity values. The default Metis partitioning scheme

available in ANSYS Fluent was used to perform the partitioning for the single fan installation simulations. The PJM simulations did not require a particular partition arrangement, which meant any number of processors could be used. The number of parallel processers (6-24) used for the PJM simulations, therefore, varied depending on available resources and time constraints.

4.1.3 Simulation setup specifications

This subsection details the configuration of the numerical solver and the process undertaken to arrive at the final specifications. The steady, double-precision, three-dimensional pressure-based solver available in ANSYS Fluent, version 18.1 was used in all the simulations in this study. While it is highly likely that transient flow features are present in the physical case (Thiart and von Backström, 1993), steady-state simulations were considered sufficient for the purposes of this study, consistent with multiple prior investigations (Bredell, 2005; Owen, 2010; van der Spuy, 2011; Fourie, 2014). In every case, air at a density of 1.2 kg/m^3 and dynamic viscosity of 1.8 x 10^{-5} kg/ms is used. The realizable k-ε turbulence model, as recommended by van der Spuy (2011), is utilized in conjunction with the enhanced wall treatment functionality. Further details of these chosen solution models and the motivations for their selection are provided in Appendix A.

The simulations were set to converge to scaled residuals of 10^{-4} within a maximum of 3000 iterations. Van der Spuy (2011) adopted the same convergence criteria, except a 2000 iteration limitation was imposed. From initial simulations it was noticed that in some instances there was still notable variance in monitored variable values come the 2000 iterations mark; therefore, the maximum iteration limit was extended to 3000, at which point adequate convergence was consistently achieved.

The selection of the employed discretisation schemes evolved in several steps. Initial simulations used second-order upwind differencing (SD) schemes for all the flow variables. Correct fan characteristic curves were determined and acceptable convergence was achievable in reference to fan static pressure rise. However, when the study later progressed into analysing the fan blade loading, it was discovered that the exclusive use of second-order interpolation schemes resulted in instabilities and an unrealistic flow field in the fan rotor region. Likewise, convergence with regards to variable monitors within the fan region was not attainable.

The use of first-order upwind differencing (UD) schemes remedied the occurrence of the instabilities; however, the greater accuracy offered by second-order schemes was desired. A compromise was, therefore, attained through the utilization of ANSYS Fluent's linear discretisation scheme blending functionality (Fluent, 2009). Fluent allows the application of higher-order discretisation schemes in combination with a degree of first-order upwind differencing. This is done through the introduction of an adjustable blending factor, Ψ, into the resultant discretisation equations. The discretisation process aims to express the value of a scalar quantity, ϕ, at a control volume node, p, as a linear combination of the value

of ϕ at neighbouring nodes, n. The blending factor is introduced into the discretisation equations as shown in Equation 4.1 (Meyer and Kröger, 2001).

$$\phi_p = \Psi \sum a_n^{UD} \phi_n^{UD} + (1 - \Psi) \sum a_n^{SD} \phi_n^{SD} + S_\phi \tag{4.1}$$

where $0 \leq \Psi \leq 1$ and S_ϕ is a source term. The influence coefficients, a, are dependent upon the relevant governing conservation equations, the geometrical characteristics of the control volumes (cells), and the chosen interpolation scheme used to equate the scalars and scalar gradient values at the cell interfaces (Meyer and Kröger, 2001). Further discussion of discretisation schemes is provided in Appendix A.

Blended second-order upwind schemes were, therefore, used for all flow variables. Application of a linear blended discretisation scheme promised results of higher accuracy, relative to the purely first-order scheme case, while still enabling convergence to be attained. The use of a blended scheme was inspired by Meyer and Kröger (2001), who likewise used a linear first-order blending technique but in conjunction with the QUICK interpolation scheme (Fluent, 2009). The blending factor in Equation 4.1 was set to 0.5 and was selected through incremental adjustment and simulation until a realistic, uniform flow field within the fan rotor region was attained.

Additionally, the least-squares cell-based gradient calculation method was selected for its ability to handle unstructured meshes (van der Spuy, 2011) and its lesser computational expenditure requirement over the Green-Gauss cell-based scheme (Louw, 2015). The SIMPLE pressure-velocity coupling algorithm was used and warped-face gradient correction was enabled, as per the recommendation prescribed by Fluent (2009) when using hybrid meshes. Simulations were performed using both the University of Stellenbosch's High Performance Cluster (HPC1 - Rhasatsha) and the Center for High Performance Computing's (CHPC) Lengau cluster.

4.1.3.1 Boundary conditions

The specifics of the boundary conditions common to all single fan installation simulations, regardless of the employed fan model, are detailed in Table 2. The inlet turbulence specification conforms to that used by van der Spuy (2011), who verified the values through hot-film measurements. Likewise, the parameters of the porous zone condition used to represent the hex-core mesh match those determined by van der Spuy (2011).

Table 2: Boundary conditions of single fan installation model simulations

Boundary/zone	Type	Value
Inlet	Velocity inlet	Velocity magnitude set according to required mass flow rate Turbulence intensity = 3% Turbulence Length scale = 0.02 m
Hub	Wall	Absolute rotational speed = 104.7 rad/s (1000 rpm)
Outlet	Pressure outlet	Gauge pressure = 0 N/m^2
Hex-core mesh	Porous zone	Inertial resistance: x-direction = 1000 m^{-1} y-direction = 1000 m^{-1} z-direction = 2.442 m^{-1} Viscous resistance: x-direction = 0 m^{-2} y-direction = 0 m^{-2} z-direction = 1173168 m^{-2}
Inlet chamber walls	Slip walls	-

4.1.3.2 Pressure jump method

For the PJM model simulation, Fluent's standard fan boundary condition was applied to the upstream interior face of the rotor disk domain. The pressure jump function applicable to the L2-fan used by Marincowitz (2018), was taken from Fourie (2014) and is reproduced in Equation 4.2:

$$\Delta p = -0.762v^3 + 7.072v^2 - 31.649v + 151.6 \quad (4.2)$$

where v is the local normal velocity. The prescribed default under-relaxation factors available in ANSYS Fluent, version 18.1 were used for the PJM case simulations. Mesh independence was confirmed through a mesh refinement assessment using the PJM, details of which are included in Appendix D.

4.1.3.3 Actuator disk method

The ADM sub-routine code was adapted from Bredell (2005) and modified to be applicable for the current analysis using the L2-fan. The geometrical characteristics of the L2-fan were taken from Augustyn (2013) and mathematically translated into the sub-routine code.

The ADM calculates the aerodynamic-forces that would be exerted by the fan on the flow field using blade element theory that incorporates the fan's airfoil lift and drag characteristics. Bredell (2005) notes that due to possible back-flow near the

hub and inlet flow distortions, angles of attack ranging between -90° to 90° can be experienced by an axial flow fan. However, airfoil data in the literature is typically only available over a narrow angular range, usually between -10° to 20° (van der Spuy, 2010). It was, therefore, necessary to extend the angular range of the available lift and drag coefficients for the L2-fan so that all potential flow conditions could be accounted for in the ADM.

Extension of the L2-fan's lift and drag characteristics was accomplished through two-dimensional numerical simulation of the fan's blades airfoil profile, using an approach similar to that employed by both van der Spuy (2011) and Bredell (2005). Details of these simulations can be found in Appendix C. Polynomial expressions were determined from the data for incorporation into the ADM code.

The ADM sub-routine is introduced into Fluent's solver environment as a user-defined function (UDF). UDFs enhance the standard features of Fluent by enabling additional functionality to be incorporated into the software package. UDFs are written in the C programming language and use predefined Fluent macros to access the solver data and functionality. The ADM sub-routine was implemented as a compiled UDF (Fluent, 2009) and the embedded initialization and rotor momentum source term calculation functions were hooked to the initialization sequence and rotor disk domain respectively. Additional checks applicable to the ADM's formulation are presented in Appendix D.

Based on the recommendation of Bredell (2005) the simulations were initially run for a few iterations using a momentum under-relaxation factor of 0.1. Thereafter, the momentum under-relaxation factor was reset to the default value of 0.7. All other under-relaxation factors were left at the default settings.

4.1.3.4 Extended actuator disk method

The EADM is implemented into the Fluent solver environment in an identical fashion as done with the ADM and the simulation strategy is likewise consistent. A critical consideration in the formulation of the EADM is the specification of the limiting RR above which the modified lift and drag characteristics are effected. For the 630 mm L2-fan, this was set to an RR = 0.4 and the procedure undertaken to arrive at this value is discussed in Appendix D.

4.1.4 Results

Using the solver, model configurations and solution procedures discussed above, the pressure rise characteristic of the L2-fan was numerically determined using each of the different fan models. For this purpose, multiple simulations at different flow rates were required and, hence, the level of solution convergence varied. Momentum and turbulence residuals were typically well within the mentioned limits; however, the continuity residual only converged (primarily) to higher orders of magnitude (10^{-3} to 10^{-4}). Convergence was, therefore, further assessed through monitoring of the static and total pressures ahead and downstream of the fan

rotation plane. Negligible, sustained variance was witnessed in the monitors of the simulations that ran the full 3000 iterations. Furthermore, the conservation of mass across the entire domain (influx minus outflux) was checked to be maintained. Calculated differences were consistently well below 0.5% of the applicable influx, the qualifying criteria as suggested by van der Spuy (2011).

The fan static pressure rise (ΔP_{ts}) was determined in a like manner to the method used in the experimental case (the procedure is outlined in Appendix B). The determined performance of each of the numerical fan models is shown and compared to the experimental results of both Marincowitz (2018) and Fourie (2014) in Figure 17.

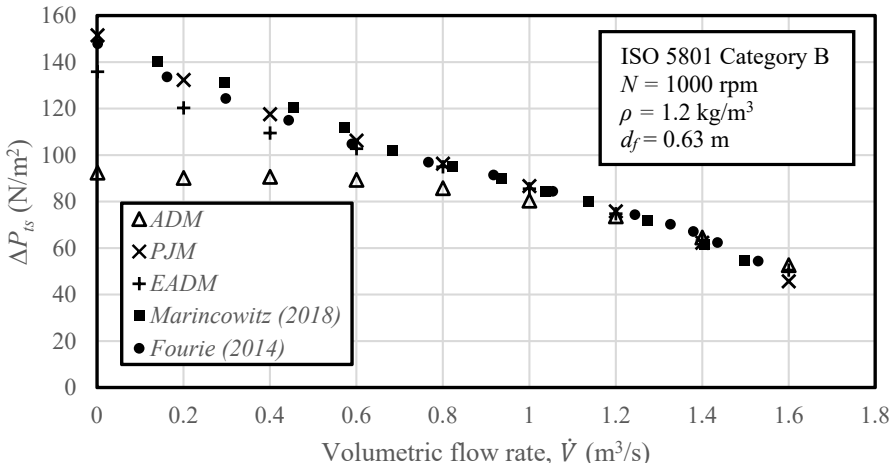

Figure 17: Comparison of fan model static pressure rise characterization

4.1.5 Discussion

The PJM is integrated into the numerical simulations through specification of the fan static-to-static pressure curve. Therefore, when looking solely at fan characteristic curve prediction under 'ideal' operating conditions the PJM offers superior performance over the ADM and EADM. Furthermore, it is seen that all the models accurately predict fan performance at high volume flow rates. However, the ADM and EADM underperform significantly at low flow rates. The ADM is unable to account for the radial flow effects; therefore, the stark deviation from the experimental results when tracing back through the lower flow rates is expected. At a volumetric flow rate of 0.4 m^3/s, the ADM predicts fan performance with an error (relative to the experimental value) of approximately 21.7%, while comparatively the ADM as used by van der Spuy (2011) was only able to predict the performance of the N-fan (fan of similar diameter and hub-to-tip ratio) within an error of approximately 19.5%. This suggests the ADM had been correctly formulated in this study. The EADM offers a better representation of fan performance at low flow

rates over the ADM. However, the EADM still under-predicts fan performance at very low flow rates, as it is expected that there exists additional energy transfer mechanisms, over and above the accounted for radial effects, that the EADM ignores (van der Spuy, 2011).

The tested fan models and mesh were deemed to deliver satisfactory results (based on expected behaviour). However, the high mesh element count hindered the timely completion of the simulations. Therefore, in an effort to lessen the computation time, the resultant element count was reduced to 1.15 million cells by polyhedral conversion of the tetrahedral cells. This was done through the standard routine available in ANSYS Fluent that was likewise utilized by both van der Spuy (2011) and Fourie (2014). The effect of this conversion was checked and, resultantly, no notable change was observed; details of this assessment are provided in Appendix D.

The results within this section, therefore, confirm that the fan models, as well as the fan tunnel meshing arrangements, could be extended into the full experimental facility simulations that are discussed in Section 5.

4.1.6 Fan operating points

In the subsequently discussed multiple fan and windscreen test facility simulations (Section 5) the ideal operating points of the fan tunnels are established through the specification of the fan tunnels' resistance. The resistance of the tunnels is manipulated through adoption of outlet-vent boundary conditions and adjustment of the attached loss coefficients. The loss coefficients needed to establish the required 'ideal' volumetric flow rate of approximately 1.45 m^3/s (as determined by Fourie (2014) and used by Marincowitz (2018)) were determined using the single fan installation model.

To this end, the velocity inlet boundary was replaced by a static pressure inlet and the total pressure outlet was replaced by the outlet-vent boundary condition. Each fan model case was re-simulated using the changed boundary conditions and the loss coefficients on the outlet-vent boundary were iteratively modified until the desired operation points were achieved. Convergence of the operating point simulations was set to a maximum volumetric flow rate magnitude change of 10^{-5} over 15 iterations. The resulting loss coefficients and the corresponding operating point volumetric flow rates ($\dot{V}_{idl}$, Equation 2.1) are presented in Table 3.

Table 3: Fan tunnel operating points

Fan Model	Loss coefficient	Volumetric flow rate, $\dot{V}_{ideal}$ (m³/s)
PJM	2.9	1.449
ADM	2.6	1.441
EADM	2.5	1.441

4.2 Windscreen model

Explicit modelling of the windscreen material is not viable in the present case as the small openings and the fine wireframes of the windscreen material cannot be accurately incorporated in the numerical model without significantly inflating mesh cell count and introducing quality complications. An implicit formulation using the porous-jump boundary condition (Section 3) was, therefore, chosen to represent the screens. The resistance (pressure drop) characteristics of the windscreens used in this study were determined experimentally by Marincowitz (2018). Three windscreen materials of differing solidity (ϵ = 0.5, 0.6 and 0.75) are used in this study. Solidity, ϵ , is defined by Equation 4.3.

$$\epsilon = \left(\frac{d_{ws}}{L_{ws}}\right)^2 \tag{4.3}$$

where d_{ws} is the diameter of the material's mesh wires and L_{ws} is the dimension of the square openings. Polynomial expressions were fitted to the data determined by Marincowitz (2018), and the resulting coefficients were converted to the needed parameters (Equation 3.14, Section 3) for input into Fluent (this conversion process is described in Appendix B). The used parameters for each material are listed in Table 4.

Table 4: Porous-jump parameters

Solidity (ϵ)	Face permeability (α_{sm})	Inertial resistance (C_2)
0.5	$1.6736 \cdot 10^{-5}$	94.9110
0.6	$3.3087 \cdot 10^{-6}$	262.8157
0.75	5.5651	$1.8715 \cdot 10^{3}$

The thickness specification (Δx, in Equation 3.14) has no effect on the application of the pressure drop (only the coefficient values), so this was arbitrarily set to 0.02 m. To verify whether the resistance parameters had been correctly deduced and to investigate the influence of various grid arrangements, a simple simulation using a straight duct geometry was created, details of which can be found in Appendix D. Figure 18 demonstrates the method's ability to capture the correct resistance characteristics of the used windscreens as determined through the straight duct simulations described in Appendix D. Furthermore, through these straight duct simulations, the ability of the porous-jump boundary condition to reproduce the correct flow resistance was found to be insensitive to mesh resolution.

It should be noted that the windscreens used in the experimental case (and replicated in the numerical case) can be considered to be in an 'as new condition'. In actual installations the windscreen materials' resistance characteristics would likely differ due to the accumulation of dirt and oil.

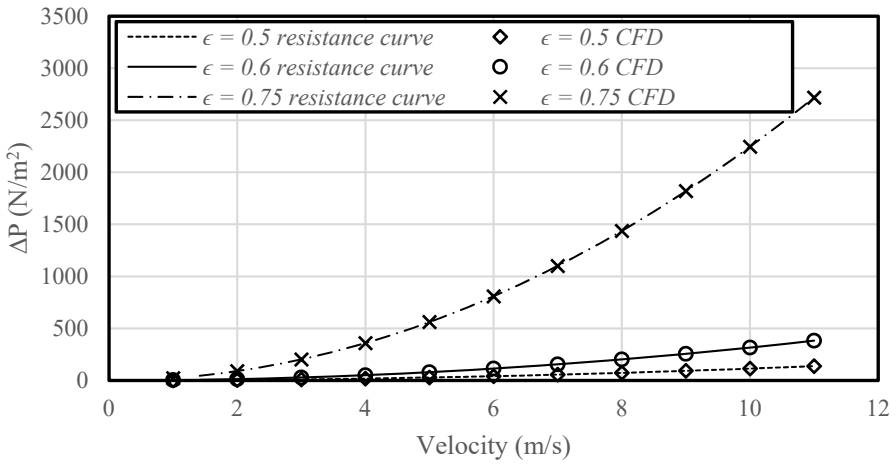

Figure 18: Prediction of windscreen material resistance characteristics using the porous-jump boundary condition

5 Experimental facility simulation details

This section details the compilation of the full multiple fan and windscreen test facility simulations that are used to replicate and numerically test the experimental findings of Marincowitz (2018). These simulations incorporate selected component models verified in Section 4. The resultant model is configured to utilize a numerical domain that mimics the experimental facility of Marincowitz (2018), and the details of the final meshing structures and solver configurations are presented within this section. The subsequent results from these simulations are addressed next in Section 6

5.1 Geometry and Meshing

The geometry resembles the internal dimensions of the facility shown in Figure 4 (Section 2), plus the inclusion of an exhaust outlet air space and the outlet diffuser section of the small coupled open-loop wind tunnel, shown in Figure 19. The outlet diffuser section of the wind tunnel was included in the geometry as Marincowitz (2018) measured a near uniform velocity profile at the entrance to this section; therefore, a known boundary condition could be established in the numerical simulations.

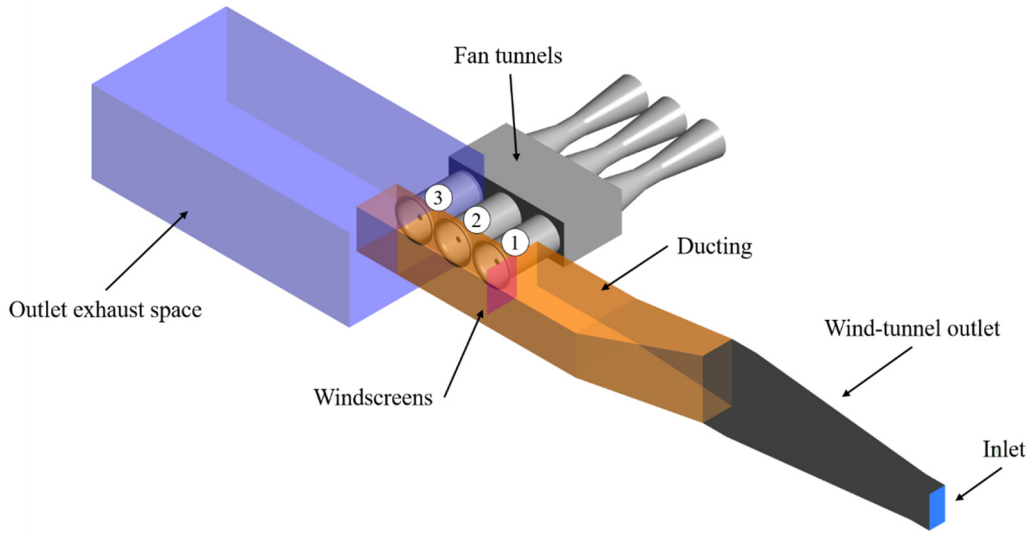

Figure 19: Numerical domain of experimental facility simulations

The geometry and meshing of each fan tunnel and the immediate region ahead of the fan bellmouths are identical to that adopted in the single fan installation simulations described in Section 4, with the exception that the upstream space is bounded by solid duct walls. Therefore, the exterior portions of the upstream region

meshes were slightly modified to accommodate the necessary inflation layers of the surrounding walled boundaries.

The dimensions of the outlet air space were confirmed through a domain dependency check and a discussion thereof is provided in Appendix D. The outlet air space was extended over the third tunnel in the fan row so that the imposed boundary conditions did not influence the flow field exiting the fan row. An additional element size restriction was enforced in the straightening section upstream of the fan row. Meshing within the remaining domains was generated using the global proximity and curvature sizing function with a fine relevance centre, slow transition and fine span angle centre specification. Selective body meshing was again adopted to generate the correct mesh structures across the domains.

Provision for the inclusion of the windscreens into the simulations was made by segmenting a plane coincident with the flange of the inlet chamber and the straightening section, matching the placement of the screens in the physical case. The segmented plane allowed windscreens of varying height to be incorporated into the simulations through assigning the porous-jump boundary condition to the respective faces. A face sizing was applied to the segmented plane so as to further limit the cell size within the immediate upstream region of the fan row.

Polyhedral conversion of the tetrahedral elements was again utilized to reduce the cell count, resulting in a mesh of 3.8 million cells. Partitioning of the mesh was structured such that the disks of the ADM and EADM models were always grouped into one partition. The number of processors used in the simulations changed depending on the particular configuration of fan models, albeit, no more than 8 were used at a time.

The refinement of the fan tunnels' meshing was already checked in the preceding single fan installation simulations (Section 4). All other meshed domains were considered conservative and removed from the area of interest, so a refinement assessment of the remaining domains was not considered necessary.

5.2 Simulation setup specifications

The steady, double-precision, three-dimensional pressure-based solver available in ANSYS Fluent, version 18.1, was again invoked for all the multiple fan and windscreen facility simulations. Multiple different fan model configurations for the three fan tunnels were trialled; however, initial simulations indicated that the best experimental agreement was attainable when using the EADM for the representation of the upwind edge fan (fan 1) and the PJM for the two downwind fans (fan 2 and fan 3). These initial simulations (the results and further discussion are available in Appendix D) showed that when the flow losses are primarily due to off-axis inflow, the PJM works well. This is expected as it has been shown that static-to-static pressure rise is independent of inflow angle (Hotchkiss *et al.,* 2006).

However, when there are also significant separated flow losses involved, the performance of the PJM breaks down considerably. The PJM is, therefore, adequate for representation of the inner fans; however, the EADM is better suited for the edge fan. The use of the PJM for fans 2 and 3 was favoured over the exclusive use of EADM on the basis that the use of the PJM relaxed the mesh partitioning requirements, enabling more computational processors to be more readily and effectively used, which assisted computation time. This limits the blade loading analysis to the edge fan only, consistent with Marincowitz's (2018) experimental analysis.

The boundary conditions used in the multiple fan and windscreen test facility simulations are detailed in Table 5.

Table 5: Boundary conditions experimental facility model simulations

Boundary/zone	**Type**	**Value**
Inlet	Mass flow inlet	Turbulence intensity = 5% Turbulence viscosity ratio = 10%
Fan hubs	Wall	Absolute rotational speed = 104.7 rad/s
Outlet fan tunnels	Outlet-vent	PJM : constant loss coefficient = 2.9 EADM: constant loss coefficient = 2.5
Outlet airspace	Pressure outlet	Gauge pressure = 0 N/m^2
Hex-core meshes	Porous zone	Inertial resistance: x-direction = 1000 m^{-1} y-direction = 1000 m^{-1} z-direction = 2.442 m^{-1} Viscous resistance: x-direction = 0 m^{-2} y-direction = 0 m^{-2} z-direction = 1173168 m^{-2}
Windscreens	Porous-jump	Table 4, Section 3

Turbulence properties of the wind tunnel exhaust flow were not known, so the default specifications as prescribed by Fluent were employed. Better approximation of the turbulent parameters was, however, not expected to affect the results of the investigation greatly, as the inlet is well removed from the fan row and turbulent properties of the windscreens are anyway omitted by use of the implicit porous media model. It is, however, recommended that further iterations of this study explore this assumption.

For the multiple fan and windscreen model simulations, convergence was again set to scaled residual magnitudes of less than 10^{-4} within a maximum of 3000 iterations.

Consistent solution scheme specifications as used in the single fan installation simulations were adopted.

It was discovered that solution convergence was significantly assisted through the use of the Full Multigrid (FMG) initialization process available within Fluent. The FMG initialization procedure constructs an approximate initial solution using ANSYS Fluent's Full-Approximation Storage (FAS) Multigrid technology. Detailed explanations on FMG initialization and FAS Multigrid technology is provided by Fluent (2009). FMG initialization was therefore used in all the multiple fan and windscreen simulations. The same convergence criteria as detailed in Section 4 was used for these simulations. Equation residuals converged in a similar fashion to the single fan installation simulations, with continuity again primarily converging to 10^{-3} to 10^{-4} orders of magnitude. Furthermore, the volumetric flow rates through the individual fan tunnels were monitored and each converged well within the 3000 iteration limit. The ensuing results and the relevant discussions thereof are presented in the following section.

6 Results and discussion

6.1 Effect of cross-flow and windscreens on fan performance

In this section the determined fan performance results from the experimental facility simulations (Section 5) are presented and discussed. In all the investigated cases, the numerical results are presented, where possible, relative to their experimental counterparts as determined by Marincowitz (2018). This section contributes to the objectives of validating the numerical modelling techniques for the purpose of analysing fan row performance under forced cross-flow and providing insight into the observed phenomena.

6.1.1 Performance metrics

Following what was done by both Marincowitz (2018) and Fourie (2014), fan performance is equated through volumetric effectiveness (ζ, Equation 2.1) and captured relative to the dimensionless cross-flow parameter β, described by Equation 6.1.

$$\beta = {}^{v_x}\!/_{v_{tip}} \tag{6.1}$$

where v_x and v_{tip} are the average cross-flow velocity beneath the fan platform and blade tip velocity respectively.

Marincowitz (2018) determined that a β value of approximately 0.1 marks an effective no-wind scenario. Flow had to be supplied from the wind-tunnel to compensate for the asymmetric inlet resistance on either side of the ducted fan row, allowing approximately symmetric velocity profiles beneath the fan platform (characteristic of a free-standing full-scale ACC in no-wind conditions) to be established. The relationship of β to approximate wind speed at the fan platform height, v_w, as determined by Marincowiz (2018), is given by Equation 6.2.

$$v_w = \frac{8\left[\left(\dot{V}_x - \dot{V}_{x(nw)}\right) + \sum_{i=1}^{3}\left(\dot{V}_{f(nw)i} - \dot{V}_{fi}\right)\right]}{7A_x} \tag{6.2}$$

where $\dot{V}_x$ and $\dot{V}_f$ are the cross-flow and fan volumetric flow rates at a certain cross-flow condition (β) and $\dot{V}_{x(nw)}$ and $\dot{V}_{f(nw)}$ are the corresponding flow rates at the no-wind scenario. Derivation of the constants in Equation 6.2 is available in Marincowtiz (2018).

6.1.2 Effect of cross-flow on fan performance with no windscreens

The capability of the numerical model to capture the effects of cross-flow in isolation is reviewed first. The determined effect of cross-flow on individual fan performance is shown in Figure 20.

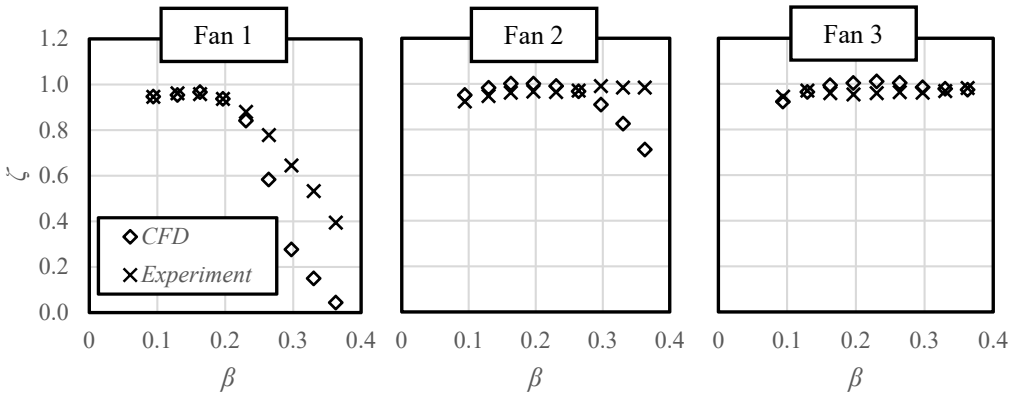

Figure 20: Effect of cross-flow on individual fan volumetric effectiveness (no windscreen)

From Figure 20, it is observed that close correlation between the experimental and numerical results exists for $\beta < 0.23$; however, the numerical results start to deviate significantly from their experimental counterparts thereafter. At these higher β values, the EADM can no longer accurately represent the axial flow fan. The deterioration of the EADM's performance at high cross-flow rates was likewise noted by van der Spuy (2011). It is, however, challenging to provide further insight into what is causing this deterioration, as the flow condition is a function of the EADM. Resultantly, the apparent mechanisms that are causing the deterioration of the model may only be artefacts of the EADM's performance. It can, therefore, only be inferred that there are additional energy-transfer mechanisms present at these high cross-flow conditions that the EADM ignores. To uncover what these mechanisms are, the flow needs to be more accurately modelled using the likes of an explicit formulation. Future studies are therefore encouraged to undertake this kind of analysis. Failure of the EADM to sufficiently entrain flow into the edge fan at the high cross-flow rates is also possible cause for the under prediction of the second fan, as underperformance of the edge fan encourages greater cross-flow velocities across the second fan, allowing separated flow and low pressure regions around the second fan's bellmouth intake to develop.

From Figure 20, it can be seen that the determined effects of cross-flow on fan performance are consistent with that described in the literature (Section 2). Increasing cross-flow is seen to have a distinctly deleterious effect on edge fan's (fan 1) volumetric effectiveness while having lesser to no influence on the downstream fans (fans 2 and 3). Figure 21 shows velocity magnitude contours and

streamlines beneath the fan row at $\beta = 0.2$, and indicates that the known mechanisms of exacerbated off-axis inflow and the formation of vortices (associated with flow separation) near the edge fan shroud are responsible for the reduction in edge fan performance.

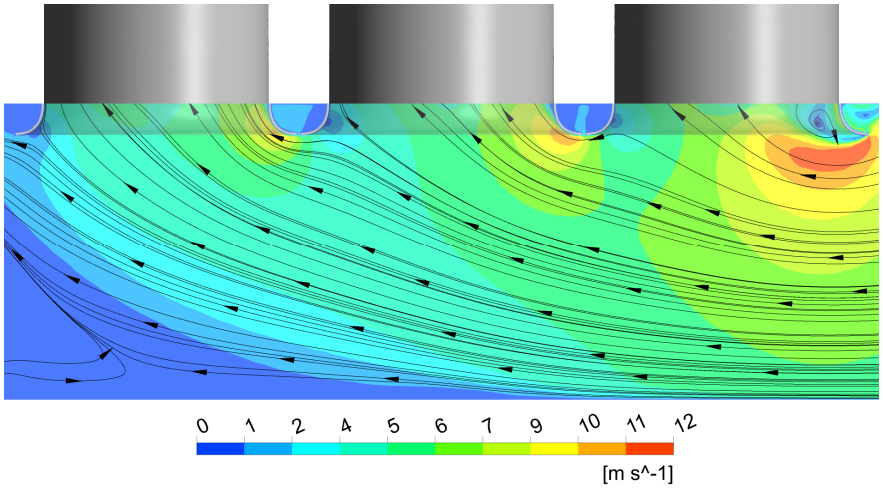

Figure 21: Flow visualization of cross-flow effects at $\beta = 0.2$ (streamlines and velocity magnitude contours)

6.1.3 Effect of windscreens on fan performance under cross-flow

The effect of incorporating peripheral windscreens into the numerical simulations is now addressed. In this study, the different windscreen materials (Section 4) are considered at three different windscreen heights, measured down from the fan platform. The windscreen height is normalized using Equation 6.3, where H_s is the windscreen length and H is the fan platform height. Heights of L = 0.25, 0.5 and 0.75 are considered.

$$L = H_s/H \tag{6.3}$$

6.1.3.1 Effect of windscreen solidity

The effect of windscreen material solidity and the ability of the numerical model to correctly replicate the experimental observations for each tested screen material are evaluated in this subsection. For this component of the discussion, only the $L = 0.25$ cases are reviewed. The material solidity effects and numerical model performance observed in the L = 0.25 cases are largely representative of the remaining cases which are available in Appendix E. The results from the simulations for each tested material at L = 0.25 are presented together with their experimental counterparts in Figures 22, 23 and 24.

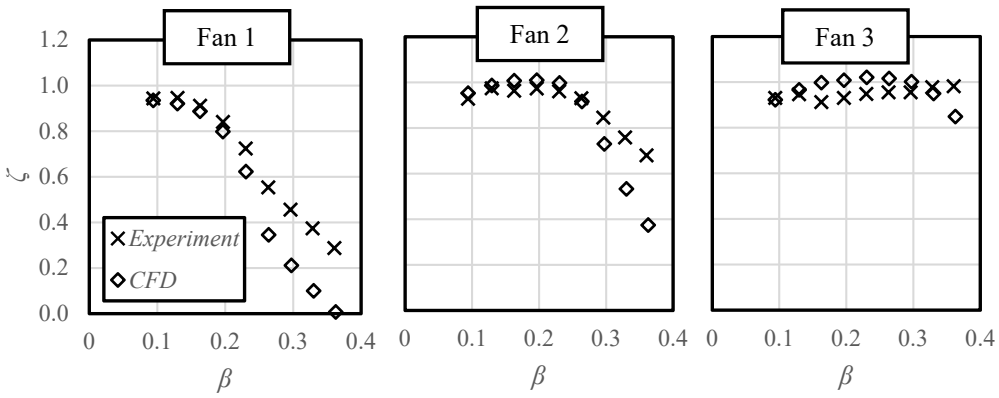

Figure 22: Effect of cross-flow on individual fan performance with $\epsilon = 0.5$ windscreen ($L = 0.25$)

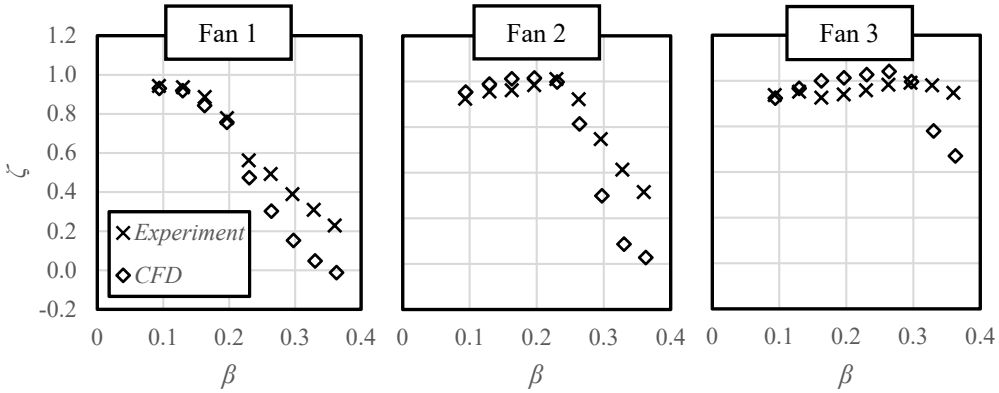

Figure 23: Effect of cross-flow on individual fan performance with $\epsilon = 0.6$ windscreen ($L = 0.25$)

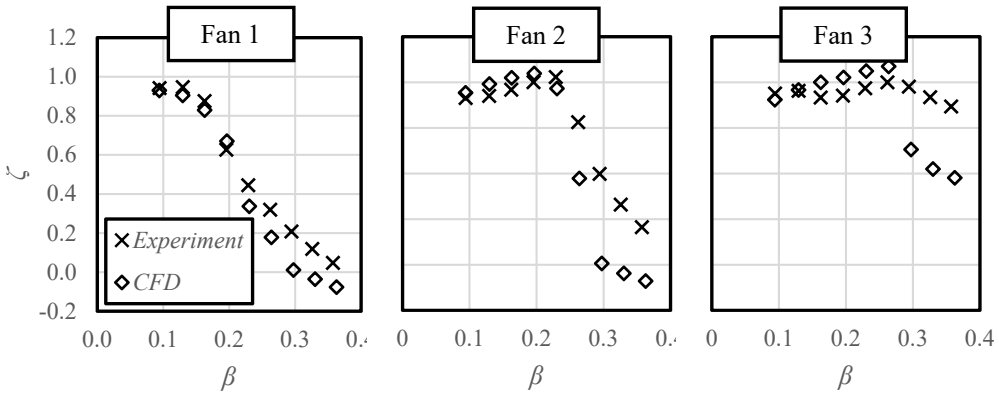

Figure 24: Effect of cross-flow on individual fan performance with $\epsilon = 0.75$ windscreen ($L = 0.25$)

The same behaviour of the numerical model as witnessed in the prior cross-flow (no screen) assessment is evident in the results given in Figures 22, 23 and 24. The numerical model is able to closely match the experimental results up to a $\beta = 0.23$, thereafter deviating significantly due to, expectedly, the same reasons suggested previously. The determined trends at the higher flow rates, however, continue to correspond to those of the experimental results.

For each material, the screens are observed to further degrade the volumetric effectiveness of the upwind edge fan relative to the no screen case, while also notably influencing the performance of the second fan. Insight into these occurrences is gained through visualization of the total pressure contours beneath the fan platform for each case, as shown in Figure 25. Figure 25 depicts that these occurrences emerge due to the screens exacerbating the extent of the low pressure region that develops at the entrance of the fan row further downstream.

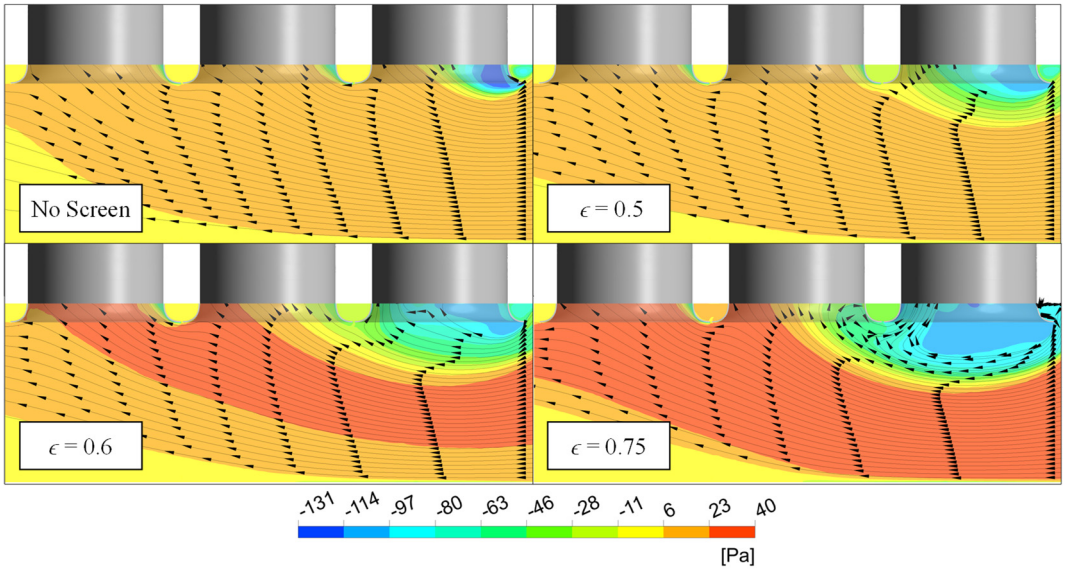

Figure 25: Total pressure contours beneath fan row at $\beta = 0.2$ (screens of different porosity, $L = 0.25$)

Furthermore, Figure 26 shows the velocity contours beneath the fan platform in each case and how the screens, by constricting the peripheral inlet area, form a high-speed flow region beneath them. As the screen solidity increases, the incoming flow near the platform is further constricted and the high-speed flow beneath the screen is further accelerated. This causes a deficit of flow within the wake of the screens resulting in an effective 'suffocation', as similarly observed by Owen (2010). The pressure losses associated with the recirculation of the flow on top of the accelerated flow region also underpins the exacerbation of the low pressure zone ahead of the fan inlets seen in Figure 25. Similar findings were ascribed in the analysis of Maulbetsch and DiFilippo (2016).

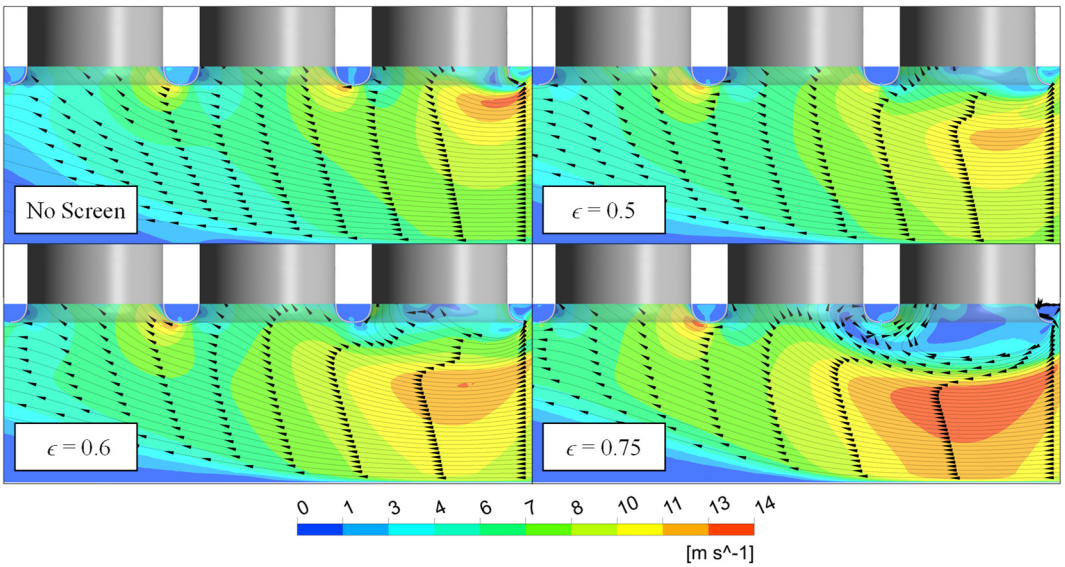

Figure 26: Velocity magnitude contours beneath fan row at $\beta = 0.2$ (screens of different porosity, $L = 0.25$)

Figure 26 further illustrates that without a windscreen, the cross-flow strikes the edge fan bellmouth at a greater velocity and, resultantly, sharper pressure gradients attach to the upstream portion of the bellmouth wall (as seen in Figure 25). Hence, in the absence of a screen, lower localized pressures are present within the edge fan inlet region; however, the low pressure zone is concentrated over a smaller portion of the face fan and performance is not as severely affected. The lower localized pressure is, however, a consequence of relevance to fan blade loading which is discussed in Section 6.2.

6.1.3.2 Effect of windscreen height

This subsection details the effect of windscreen height. The material with a 50% solidity ($\epsilon = 0.5$) was chosen for this component of the discussion; however, the results for the higher solidity materials can be found in Appendix E. To supplement the validation case of the numerical modelling techniques, the determined individual fan performance results are again compared to the experimental measurements of Marincowitz (2018). The individual fan performance results from this screen height analysis are depicted in Figures 27 and 28.

The results in Figures 27 and 28 show once more that the numerical model can accurately represent the experimental fan performance results up to $\beta = 0.23$. However, the numerical results again deviate from their experimental counterparts at the higher cross-flow rates.

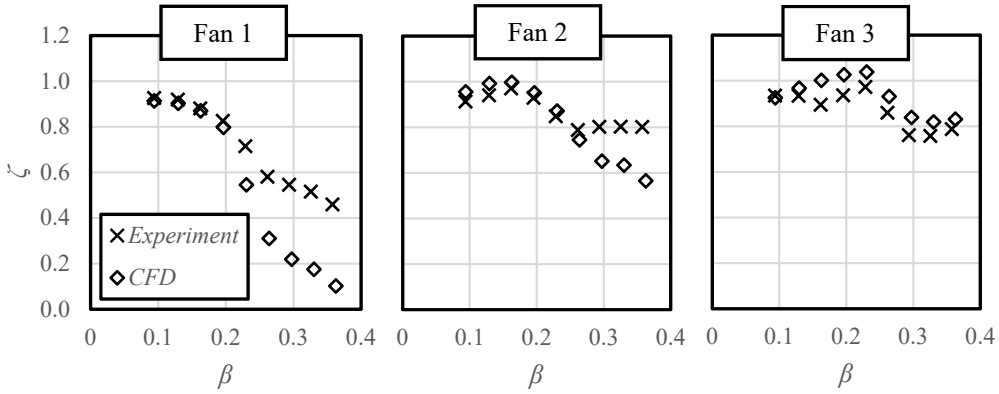

Figure 27: Effect of cross-flow on individual fan performance with windscreen at $L = 0.5$ ($\epsilon = 0.5$)

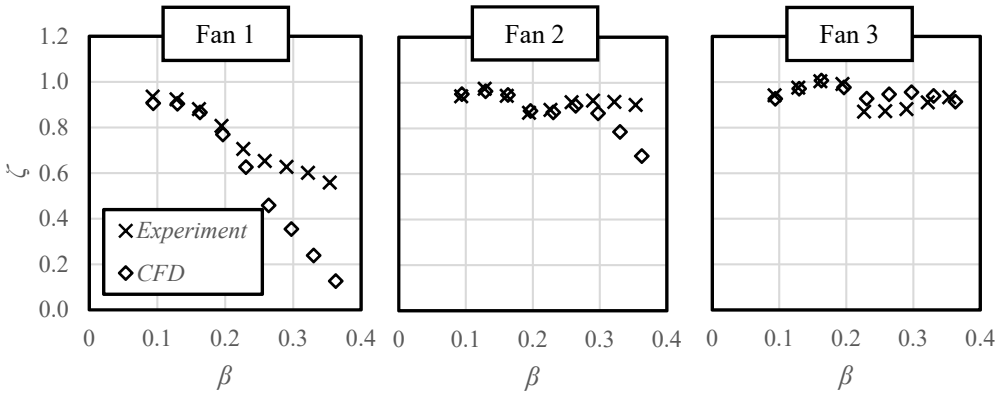

Figure 28: Effect of cross-flow on individual fan performance with windscreen at $L = 0.75$ ($\epsilon = 0.5$)

To further assess the ability of the porous-jump boundary condition to capture the dynamics of the physical windscreens, the numerically determined velocity fields immediately ahead of the edge fan were compared to those from the experimental analysis (determined by Marincowitz (2018) through PIV measurement). The comparison is shown in Figure 29. Close agreement between the numerical and experimental velocity fields is observed in Figure 29(a) and (b), which suggests that the porous-jump boundary condition is, at the very least, able to model the macro-structure flow features induced by the windscreens.

Furthermore, although fan performance is not accurately predicted at cross-flows beyond $\beta = 0.23$, the determined flow fields ahead of the fan row are still reasonably well captured; as demonstrated in Figure 30. Figure 30 shows the numerical and experimental mid-plane velocity fields ahead of the edge fan for $\beta = 0.33$. The close agreement of the velocity fields in Figure 30 further endorses the validity of using the porous-jump boundary condition for the representation of the windscreens.

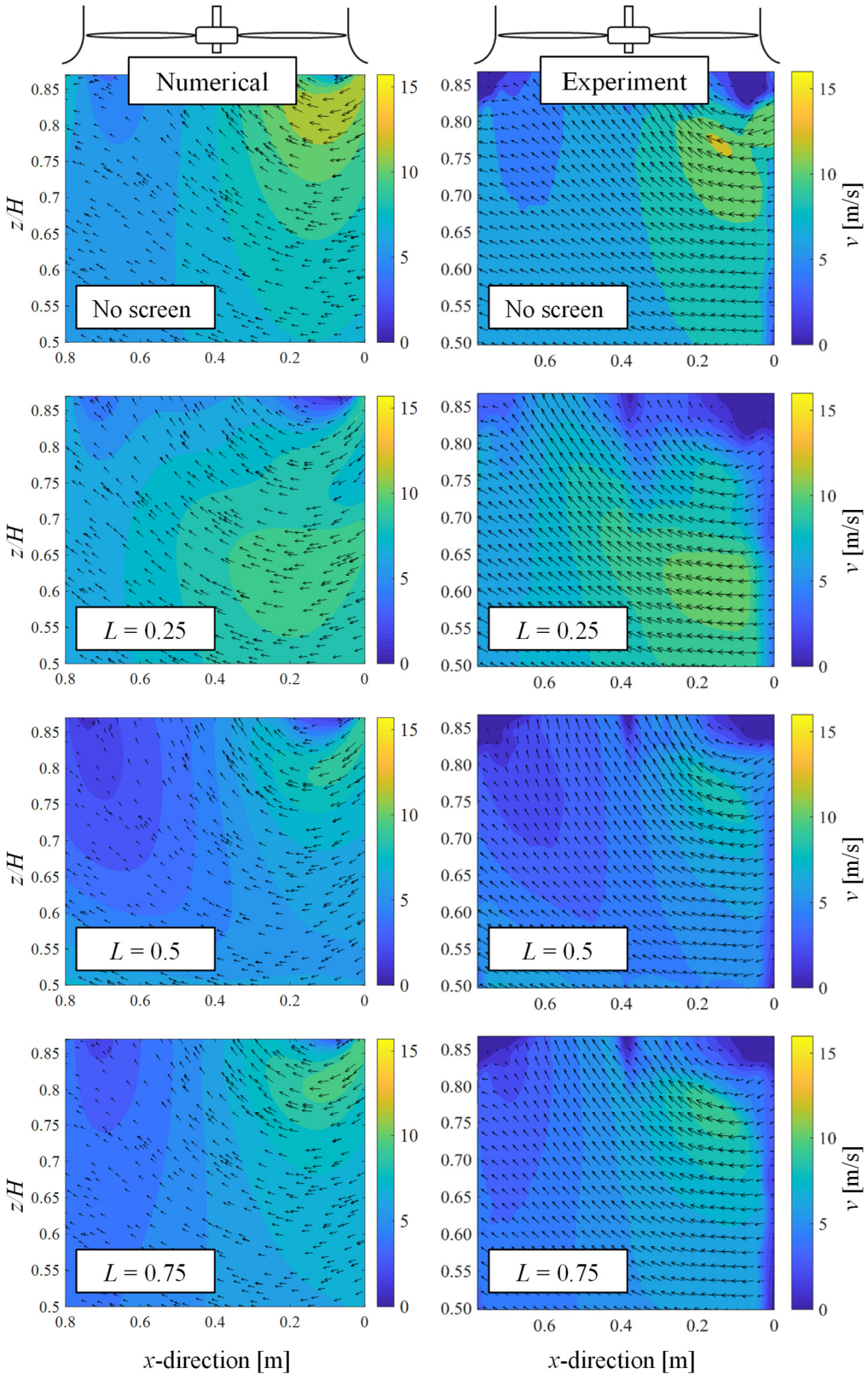

Figure 29: Comparison of mid-plane flow fields ahead of the edge fan at $\beta = 0.2$ (velocity magnitude contours and vectors, $\epsilon = 0.5$)

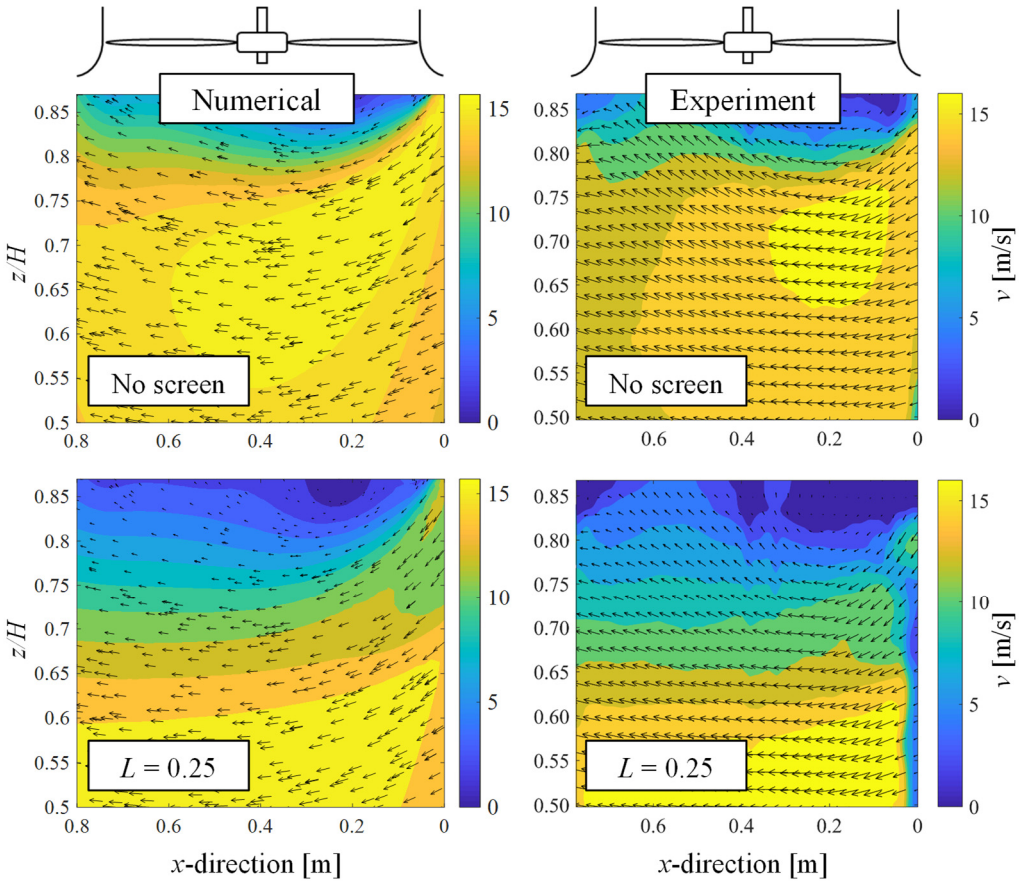

Figure 30: Comparison of mid-plane flow fields ahead of the edge fan at $\beta = 0.33$ (velocity magnitude contours and vectors, $\epsilon = 0.5$)

Figure 31 shows comparative figures for the numerical and experimental edge fan results. It is interesting to note that while the EADM struggles to predict fan performance at cross-flow rates beyond $\beta = 0.23$, the numerical model still reproduces very similar qualitative trends to those seen in the experimental measurements at the higher cross-flows, as shown in Figure 31. Accordingly, both the experimental and numerical results reveal that the edge fan's performance is improved by the windscreen at a height of $L = 0.75$ from $\beta = 0.3$; and at $\beta = 0.36$, both the $L = 0.5$ and $L = 0.75$ cases are beneficial.

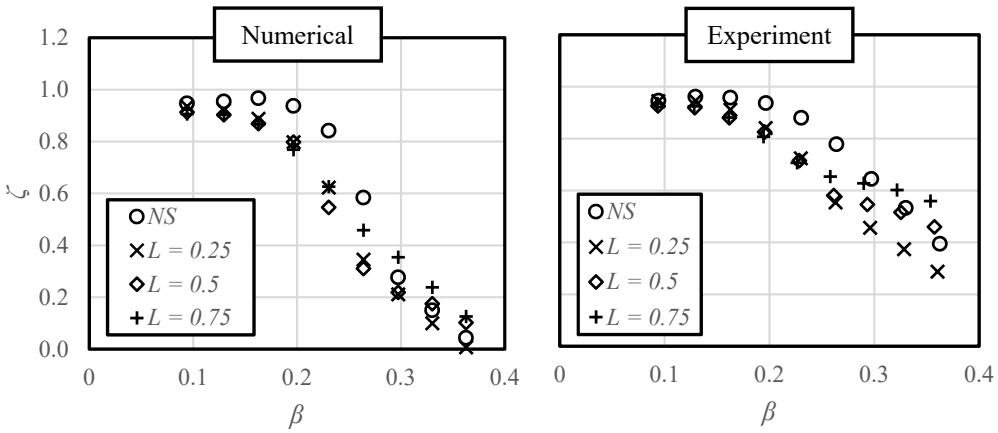

Figure 31: Comparative edge fan performance prediction ($\epsilon = 0.5$)

The contraction loss incurred by the accelerating flow is increased proportionately with the length of the screen. Therefore, at high L values (particularly at high cross-flow rates) the flow more readily permeates through the screen rather than deflects beneath it (Marincowitz *et al.* 2019). For $\beta > 0.3$, the $L = 0.75$ screen reduces the velocity at which the approaching cross-flow strikes the edge fan's bellmouth (reducing the inlet flow losses) while still allowing sufficient flow to permeate through and not choke the fan. Likewise, at high cross-flow rates, the screen at $L = 0.75$ effectively diverts the high speed flow region that forms beneath it past the fan row, shown in Figure 32. This reduces the cross-flow velocities upstream of fan 2 and fan 3, enabling the flow to be more axially entrained by these fans and higher static pressures to develop beneath them, as shown in Figure 33.

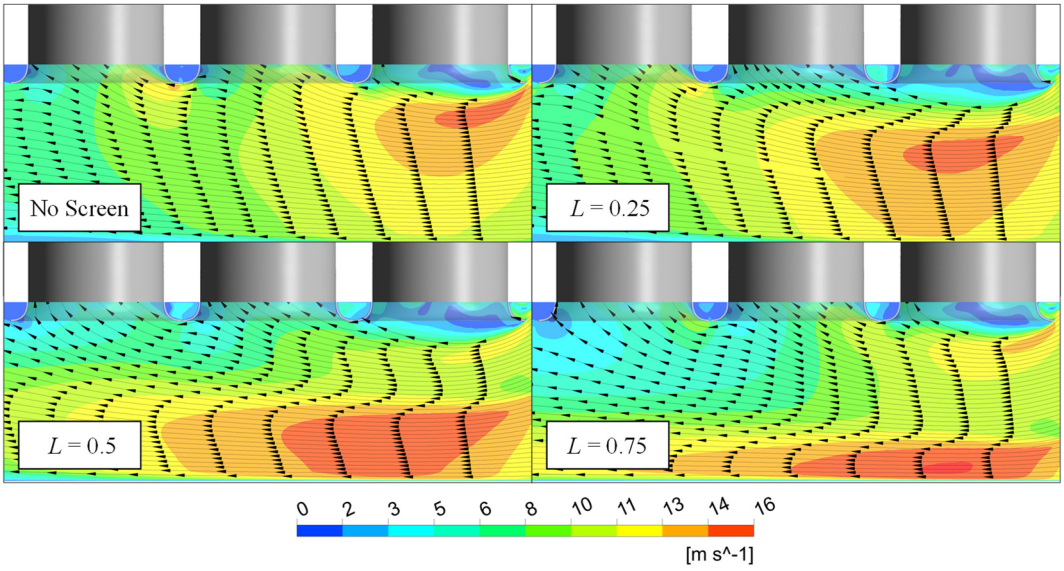

Figure 32: Velocity magnitude contours and pathlines beneath the fan platform with windscreens at different heights ($\beta = 0.3$)

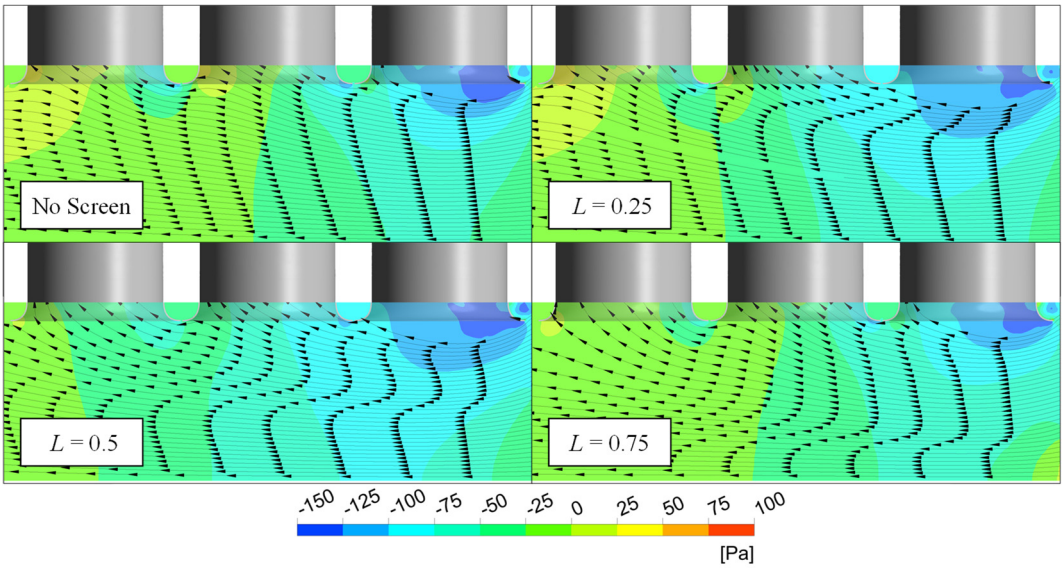

Figure 33: Static pressure contours and pathlines beneath the fan platform with windscreens at different heights (β = 0.3)

The higher static pressure and axially drawn downstream flow then assists in directing the flow into fan 1, causing a subsequent shrinkage of the low pressure/recirculating zone across the edge fan, thus further supplementing the edge fan's performance.

6.1.4 Summary of the fan performance analysis

The effects of cross-flow on fan row performance, with and without windscreens, were reviewed within this section. The numerical model was found to be successful in capturing the known effects associated with increasing cross-flow (that of exacerbated off-axis inflow and flow detachment around the edge fan shroud). Similarly, the numerical model was also shown to be able to successfully reproduce the experimental fan performance trends and flow field dynamics.

The numerical model demonstrates the ability to quantitatively represent fan row performance for moderate cross-flow conditions. Figure 34 shows that in terms of system volumetric effectiveness, described by Equation 6.4, the numerical model is able to predict the discussed experimental cases within a maximum error of 9.1% up to β = 0.25 (v_w ~ 6 m/s (Equation 6.2), full-scale ~ 9 m/s); error is defined by Equation 6.5 (prediction error for the remaining cases in presented in Appendix E). At higher cross-flow conditions, it is suspected that the EADM is no longer able to account for all the energy transfer mechanisms present within the flow field and, therefore, only a qualitative evaluation is possible. Degradation of the EADM's performance is linked to the development of the separated flow/low pressure region across the edge fan face. Therefore, with the higher solidity material windscreens exacerbating the size of this region to the greatest extent, the model's performance is poorest in these configurations (at L = 0.25).

$$\zeta_{sys} = \frac{\sum_{i=1}^{N_f} \dot{V}_{act,i}}{N_f \dot{V}_{ideal}} \tag{6.4}$$

$$\text{Error} = \frac{abs\left(\zeta_{sys,CFD} - \zeta_{sys,EXP}\right)}{\zeta_{sys,EXP}} \times 100 \tag{6.5}$$

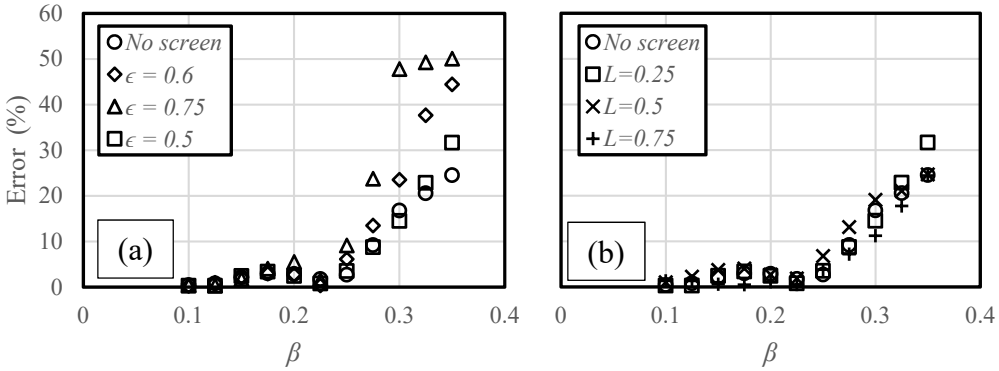

Figure 34: Numerical system volumetric effectiveness prediction error: (a) L = 0.25 (b) ϵ = 0.5

Whereas the effects of cross-flow are primarily prevalent on the upwind edge fan, it was observed that in some instances the windscreens had an effect on all the fans within the fan row. This warrants an assessment of the screens in terms of system volumetric effectiveness. The system performance results for the discussed cases are given in Figure 35.

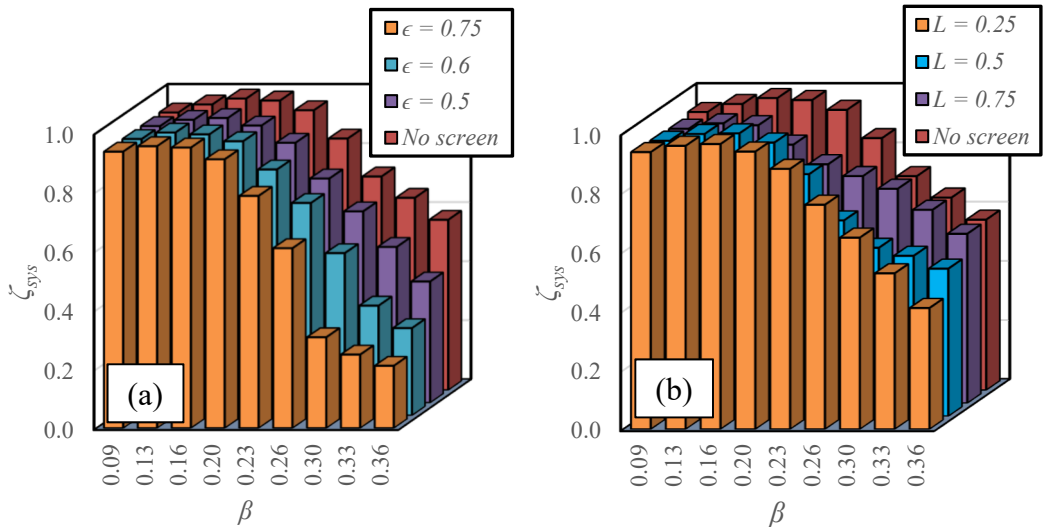

Figure 35: Effect of cross-flow on system volumetric effectiveness (numerical results): (a) L = 0.25 (b) ϵ = 0.5

From Figure 35, it is apparent that for the particular case investigated (characteristic of an ACC of low platform height), the installation of peripheral windscreens has a primarily negative effect on fan row performance. For the $\epsilon = 0.5$ windscreen material, a maximum system performance reduction of 18.9% (calculated using Equation 6.6) is uncovered at $\beta = 0.26$ with the screen at a height of $L = 0.5$. For the $\epsilon = 0.6$ material, a maximum performance deficit of 28.1% is uncovered at $\beta = 0.36$; and for the $\epsilon = 0.75$ material, a 41.6% reduction at $\beta = 0.3$. Slight performance enhancement (<1% improvement) is, however, offered by the $\epsilon = 0.5$ windscreen at $L = 0.75$ at very high cross-flow rates ($v_w > 11$ m/s, Equation 6.2). Similar improvements at high screen heights are observed for the $\epsilon = 0.6$ and 0.75 materials; the results of which are available in Appendix E.

$$\text{Performance difference} = \left(\zeta_{\text{sys,ws}} - \zeta_{\text{sys,ns}}\right) \times 100\% \tag{6.6}$$

The results within this section are, however, limited by the two-dimensional flow approximation upon which the replicated experimental fan row facility is based. It is assumed that flow only enters the fan row from the peripheral inlet and that the sides of the fan row can be treated effectively as symmetry planes. The current numerical model, therefore, does not make provision for the inclusion of possible edge effects, which may alter the drawn conclusions. The results of this section are further limited to only the particular case investigated, as the influence of platform height needs to be reviewed (platform height effects are discussed in Section 6.3).

6.2 Effect of cross-flow and windscreens on blade loading

The effect of increasing cross-flow on blade loading, with and without windscreens, was likewise evaluated as part of this study's objectives. This section serves to detail the ability of the employed numerical techniques to capture the experimental edge fan blade loading results measured by Marincowitz (2018), while again also providing insight into the observed phenomena..

6.2.1 Effect of cross-flow on blade loading with no windscreen

The influence of cross-flow on edge fan blade loading is investigated in isolation within this subsection (absence of windscreen effects). In the numerical analysis, blade loading is quantified through aerodynamic bending moment information measured in the flap-wise direction. Use of the EADM to represent the edge fan in the numerical model enabled the determined forces that are introduced by the model into the flow field to be extracted. The forces seen by the flow field is opposite to that which the fan blades would experience during a complete rotation; therefore, azimuthal bending moment distributions could be obtained by the product of the axial force at each cell of the rotor disk and its radial position relative to the rotation axis. Figure 36 references the consistent angular description used in the presentation of all the blade loading results.

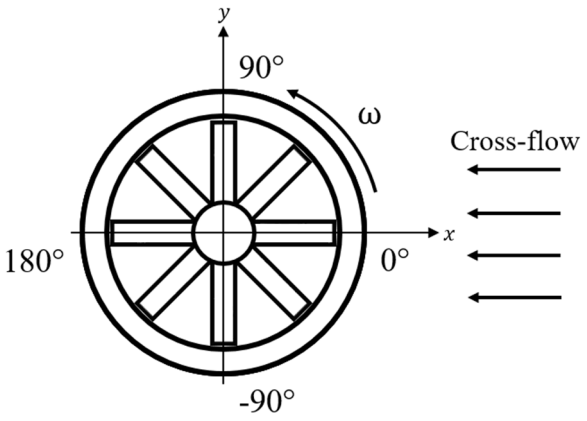

Figure 36: Angular reference for edge fan blade loading results

Direct comparison between the numerical and experimental results is challenging as the parameters used to quantify loading are not consistent. In the experimental analysis, loading is characterized through measurement of dynamic bending strain, ε, in the flap-wise (axial) direction. While it has been shown that aerodynamic loading is a major contributor to fan blade strain (Muiyser, 2016), strain quantifies the structural response and aerodynamic loading only quantifies the input force. When occurring dynamically, the response and input will not necessarily maintain the 1:1 relationship characteristic of the static case, as the response will vary depending on the harmonics of the input, the structural characteristics of the fan blade and damping effects. Therefore, it is suspected that qualitative assessment of fan blade strain can be reasonably inferred from aerodynamic loading; however, confirmation of the correlation between aerodynamic loading and strain through fluid structure interaction (FSI) simulation is a suggested topic for future research.

To characterize dynamic blade loading information, M_D, the resultant bending moments, M_R, at each azimuthal coordinate had to be first determined. Resultant bending moments were calculated through trapezoidal integration of the span-wise axial force distribution at each azimuthal coordinate, θ, as illustrated in Figure 37. The distributed axial loads depicted in Figure 37 are those extracted from the converged $\beta = 0.1$ solution. Reasons for its wayward shape are discussed in Section 6.2.3.

Numerical dynamic bending moment information (M_D) at each cross-flow condition could then be determined by first subtracting the resultant bending moment data mean (mean of the resultant moments at each θ position for a given cross-flow condition) from each resultant bending moment value, then calculating the root-mean-square (RMS) value of the data field, as described in Equation 6.7; where N_θ is the number of azimuthal positions in the rotor disk.

$$M_D = \sqrt{\frac{1}{N_\theta}\left[\sum_{i=1}^{N_\theta}\left(M_{R,i} - \overline{M_R}\right)^2\right]} \tag{6.7}$$

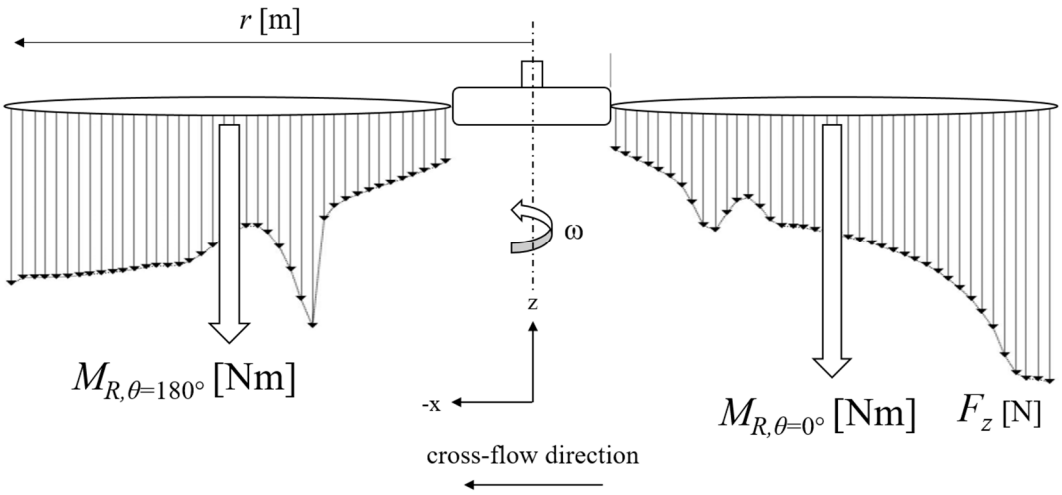

Figure 37: Visualization of resultant azimuthal bending moment determination

The numerical and experimental dynamic loading to increasing cross-flow relationships are compared in Figure 38. Both sets of results have been normalized relative to the respective value (denoted by superscripted *) at the no-wind ($\beta \sim 0.1$) scenarios.

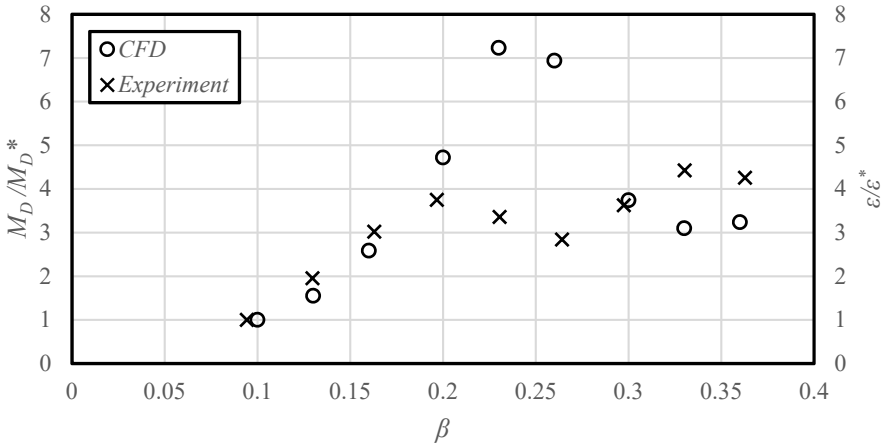

Figure 38: Effect of cross-flow on dynamic bending moment and strain (no windscreen)

Reasonable correlation between the numerical and experimental results is witnessed for low cross-flow conditions ($\beta < 0.2$), where the fan model performs well (Section 6.1). Thereafter, only partially similar trends are observed. The numerically determined dynamic bending moment results follow an initial exponentially increasing trend, then near $\beta = 0.23$ a dramatic decline in loading is

observed, which continues up to β = 0.33 before an increasing trend appears to resume. Similar trends are seen in the experimental strain measurements. The decline in the experimental results, however, is initiated at an earlier β value and the maximum normalized dynamic strain is significantly less.

Interestingly, a better numerical representation of the experimental trend is seen when considering instead peak bending moment, M_p, information, as shown in Figure 39. Peak bending moment refers to the maximum resultant bending moment present within the azimuthal distribution for a given cross-flow condition. A possible reason for this is that the strain (response) waveform is akin to that of a simple sinusoid, in which case the dynamic and peak loading trends would be proportional. This would then suggest that the numerical model is delivering a reasonable prediction of the peak loading trend, and the discrepancy between the dynamic loading trends is due to the input waveform being more complex than the response's waveform. The reason, however, is not fully understood and presents another question that can be investigated in a future FSI study.

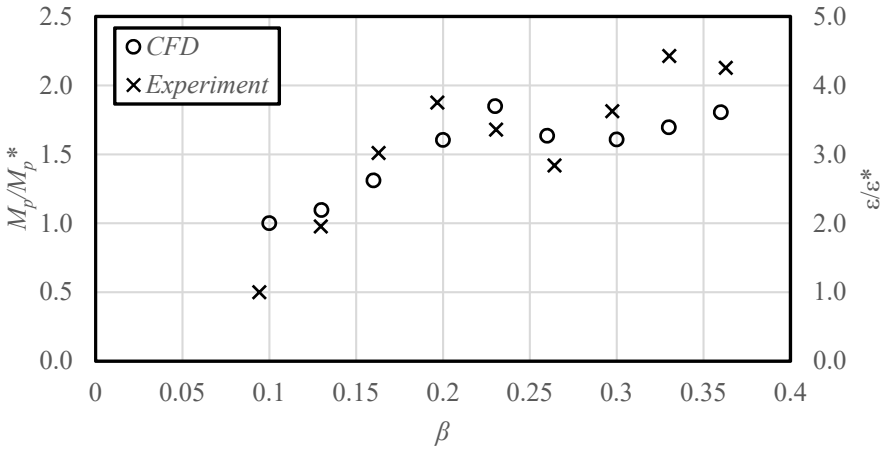

Figure 39: Effect of cross-flow on peak bending moment and dynamic strain (no windscreen)

Returning to Figure 38, differences in the dynamic loading magnitudes, just prior to the respective declines, are potentially a result of damping effects coming into play in the experimental case, or failure of the EADM to accurately determine the physical loading conditions. Continued discussion on the EADM's suitability to analysing blade loading is given in Section 6.2.3; however, focus first turns to exploring the numerical results to gain insight into the mechanisms that are determining the loading behaviour.

Figure 40 captures interpolated surfaces of the discrete bending moments, M, determined at each cell of the EADM rotor disk at increasing cross-flow conditions. The data surfaces have been normalized based on the maximum discrete bending

moment found in the azimuthal distribution at the no wind $\beta = 0.1$ solution (M^*). The dotted rings on the plots of Figure 40 coincide with RR = 0.4, indicating the point at which the augmented lift and drag characteristics of the EADM take effect. Furthermore, the white lines across the plots mark the azimuthal coordinate along which the maximum resultant bending moments (M_R) are found to occur.

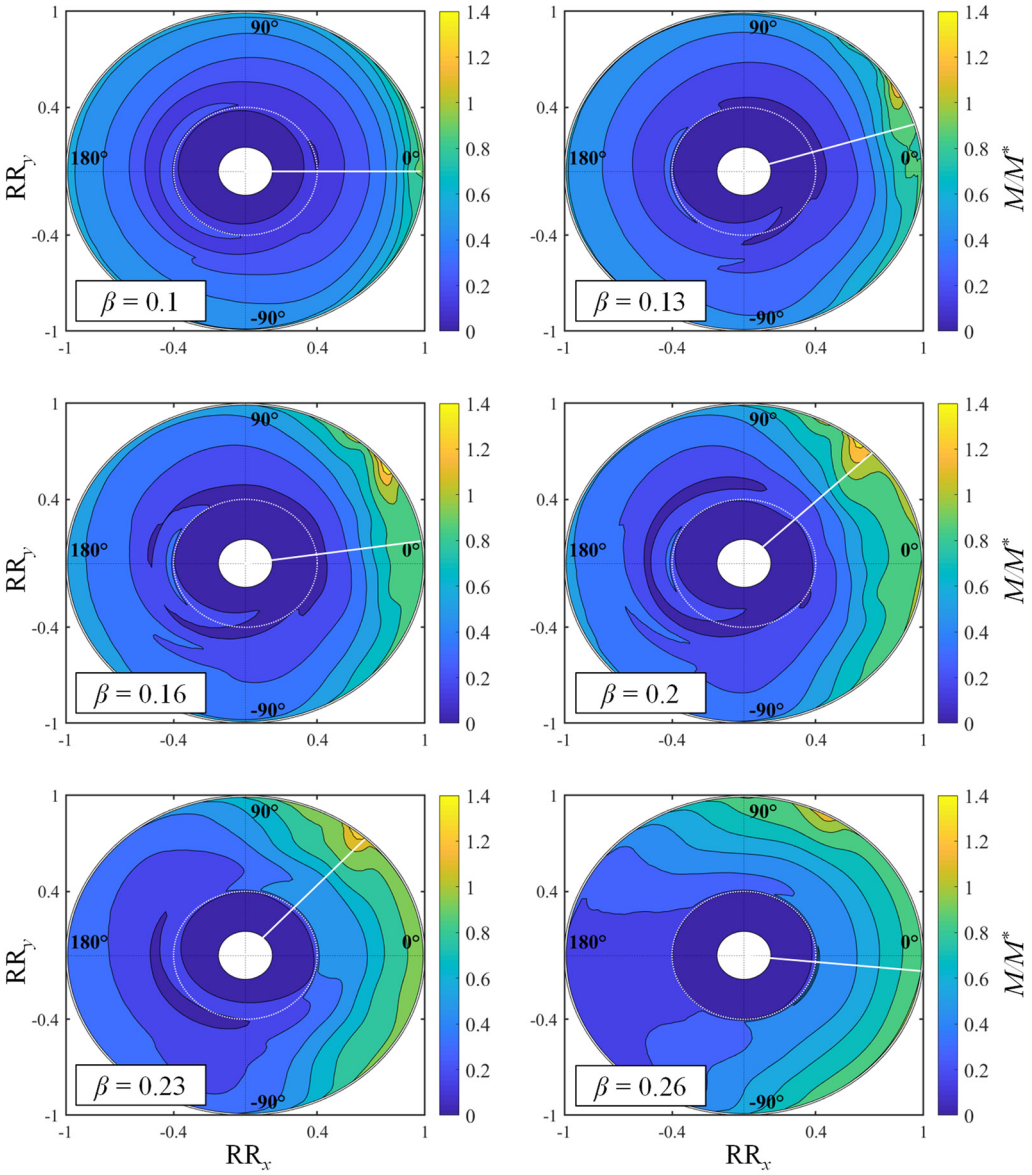

Figure 40: Azimuthal bending moment distributions over edge fan rotation plane at increasing cross-flow rates (no windscreen)

From the surface plots in Figure 40, it is evident that there exists an asymmetry to the azimuthal loading. This observation was likewise echoed in the investigations

of Heinemann and Becker (2014) and Hotchkiss *et al.* (2006). This variance is caused by the changing flow angle of attack and relative velocity magnitude with azimuthal position. Where the blade motion opposes the direction of the local inflow's horizontal component, greater angular momentum is introduced into the flow field. The kinematic effect is illustrated in Figure 41, where v_h is the local horizontal inflow velocity component. Figure 41 shows that opposing inflow introduces greater axial forces by virtue of increased relative velocity magnitudes and greater flow angles of attack.

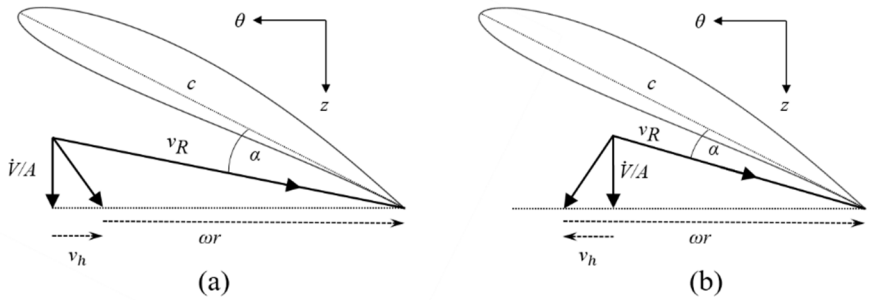

Figure 41: Kinematic effect of local inflow on the relative velocity magnitude and angle of attack (adapted from Hotchkiss *et al.* (2006)): (a) inflow opposing fan motion (b) inflow following fan motion

The surface plots in Figure 40 also show that high bending moments, as noted by Bredell (2006), Hotchkiss *et al.* (2006) and Muiyser (2012), are expectedly found within the windward midsection portion of the rotation cycle. Furthermore, high loading magnitudes and localized maxima are surprisingly found within the first quarter (0° to 90°) of the blade's rotation.

Visualization of the streamlines about and through the edge fan, at a representative cross-flow condition (β = 0.23), reveals that these large bending moment magnitudes occur where the recirculating flow tracing the outer edge of the separated flow region encroaches onto the fan rotation plane at the blade tip, as shown in Figure 42. The recirculating flow introduces a marked upstream tangential velocity component, or pre-swirl, which incites greater axial loads. The greater pre-swirl and corresponding low axial velocities enlarge the relative velocity magnitude and angle of attack in accordance with the kinematic effect detailed in Figure 41.

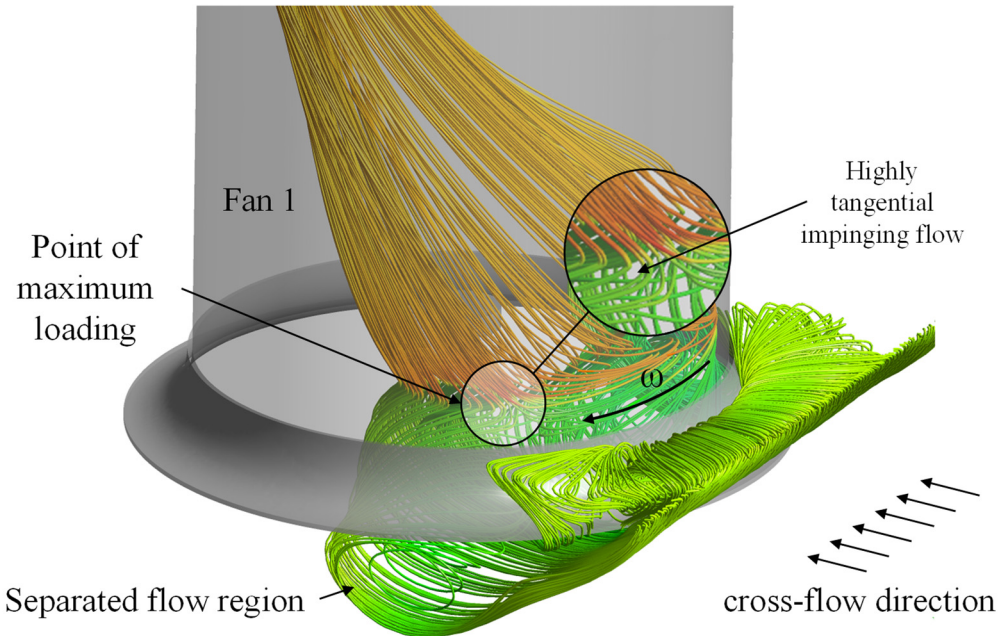

Figure 42: Flow visualization showing streamlines tracing the outer edge of the separated flow region and passing through the edge fan rotation plane (β = 0.23, no windscreen)

It is the upstream recirculation of the separated flow region in opposition to the direction of the global cross-flow and blade motion that is, therefore, responsible for the high bending moments observed in the first quarter of the fan rotation cycle. Correspondingly, in the fourth quarter (-90° to 0°), the blade motion follows the direction of the recirculating flow and the tangential velocities in this quadrant are resultantly lower.

This observation is supplemented by Figure 43, which shows a decomposition of the circumferential velocity components and angles of attack at the blade tip (where the maximum discrete bending moments occur) for the cross-flow condition of $\beta = 0.16$ (arbitrary, representative case). In Figure 43, all the velocity components and angles of attack have been arbitrarily normalized relative to their respective maximum circumferential value along the blade tip radius. The values are normalized only to assist visualization of the flow constituents' circumferential trends.

Figure 43 illustrates that where the maximum discrete bending moments (M) occurs ($\theta = 36.9°$), there is a high tangential flow presence (pre-swirl) and a localised drop in the axial velocity component (indicating that the flow becomes nearly entirely tangential), which in turn incites a high angle of attack and, hence, the spike in the loading. Likewise, the lower tangential velocities in the fourth quadrant of the fan rotation plane are also evident from the trends depicted in Figure 43.

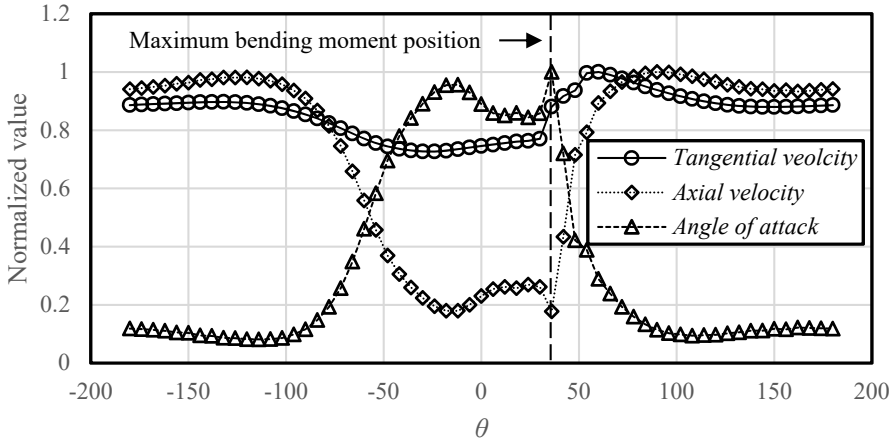

Figure 43: Circumferential flow constituents seen along the blade tip radius at β = 0.16 (no windscreen)

With the cause for the high bending moment presence in the 1st quarter of the fan rotation plane explained, reconsider the effect of cross-flow on blade loading shown by Figures 38 and 39. For a fan operating under 'ideal' inlet conditions, as the volume flow rate is reduced, the fan static pressure rise increases. In the absence of cross-flow effects, peak blade loading would therefore be expected to be proportional to the fan's static pressure curve (Muiyser, 2012). The introduction of cross-flow, however, distorts the peak loading relationship and the jagged profile depicted in Figure 39 results.

The initial increase in both the peak and dynamic loading trends is considered to correspond to the growth of the separated flow region across the windward portion of the fan face as the cross-flow increases. The flow rate through the fan is correspondingly lowered, leading to greater pressure differentials across the fan rotation plane and, hence, greater peak loading (as would be apparent under 'ideal' inlet conditions) and more variability (since this only occurs over concentrated portions of the fan face).

The decline in the loading results then follows and it is suspected (keeping in mind the caveat that the apparent mechanisms determining the loading behaviour may just be artefacts of the EADM's performance) that it is the variability of radial flow features within the windward midsection/first quarter portion of the fan rotation cycle (~ -5° to 90°, hereafter referred to as the critical region) that is responsible for this occurrence Radial flow features within the fan rotation plane are seen to be strongly linked to the interaction of the upstream separated flow region with downstream recirculating flow features.

To illustrate this, the numerically determined flow fields about and through the edge fan face are unpacked. Figure 44 shows the axial velocity distributions through the edge fan face at different cross-flow rates. Figure 44 shows that at low cross-flow

rates, the effect of cross-flow is to shift the hub wake region (distinguished by the low axial velocity region) into the leeward half of the fan rotation plane. This shift subsequently reduces the amount of downstream recirculation occurring in the windward half of the fan plane. Figure 44 also shows that as the cross-flow is intensified, the wake region starts to move back into the windward half of the fan face in a counter direction (clockwise) to the blade motion.

It is postulated that it is the development of the upstream separated flow region across the edge fan face that is responsible for this wake shift. As the mid-plane portion of separated flow region extends towards the far edge of the hub face, the flow becomes more axially entrained into the leeward half of the fan rotation plane, which more centrally aligns the hub's wake region and enables the occurrence of greater downstream recirculation around the hub in the windward half of the fan.

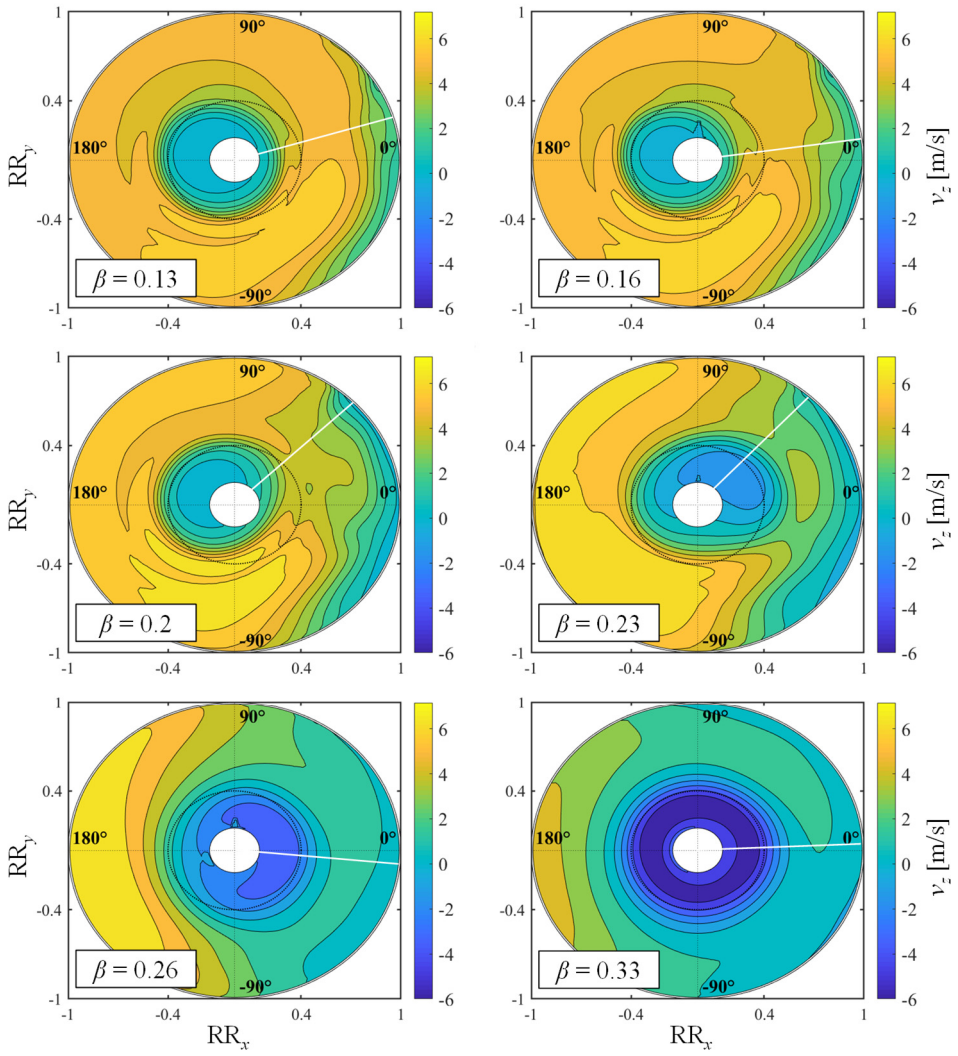

Figure 44: Axial velocity distributions through the edge fan rotation plane at increasing cross-flow rates (no windscreen)

Just prior to the decline in the peak loading trend (Figure 39), at the point where the numerically determined peak bending moment to increasing cross-flow relationship reaches a maximum ($\beta = 0.23$), a high radial flow presence is seen to be located within the critical region of the fan rotation cycle, as shown by Figure 45. It is these high radial flow velocities coupled with the high angles of attack and high tangential velocity components within this region (Figure 43), that are responsible for the high loading condition observed at $\beta = 0.23$.

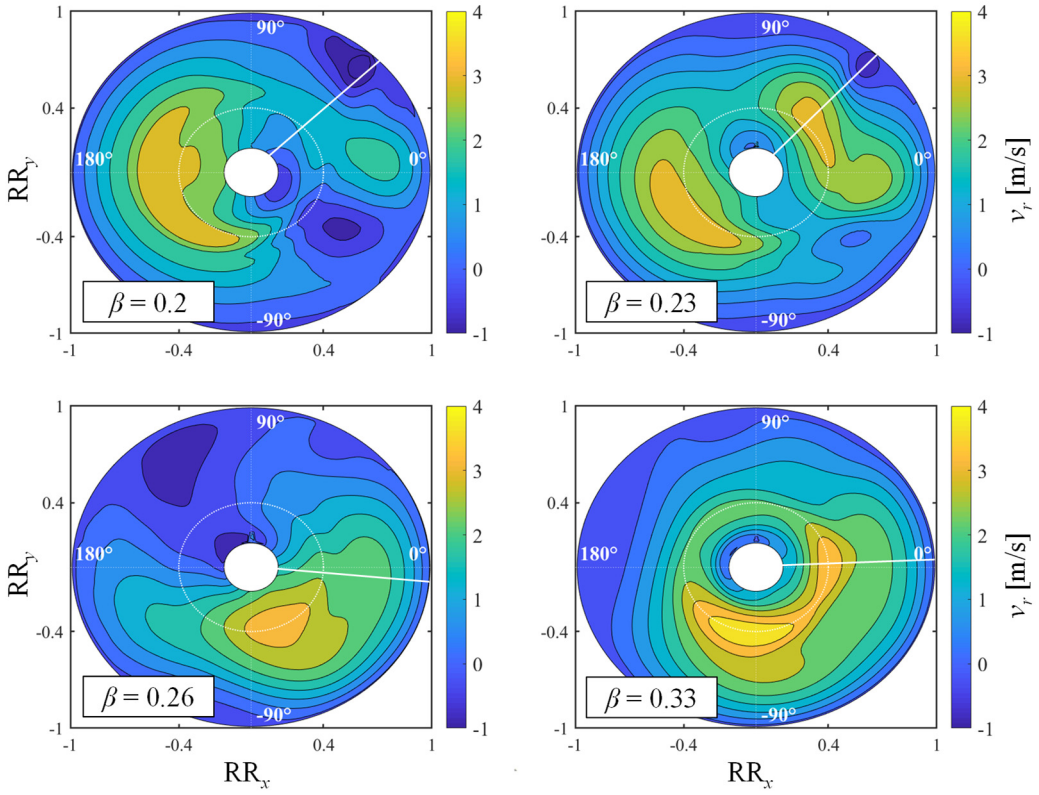

Figure 45: Radial velocity distributions over the edge fan rotation plane at increasing cross-flow rates (no windscreen)

Figure 46 provides a visualization of the mid-plane velocity vector field through the edge fan rotation plane and shows that it is the interaction between the downstream recirculating flow (within the hub wake region, shown in Figure 44) and the flow within the outer portion of the upstream separated flow region that is responsible for these significant radial flow velocities. The opposing flow regions up- and downstream of the fan rotation plane collide and deflect radially outward. The EADM recognizes this radial flow contribution by the exacerbation of the relative velocity vector and angle of attack and, hence, introduces greater aerodynamic forces in the flow field.

Following the peak at $\beta = 0.23$, as the cross-flow increases and the separated flow region continues to grow further, the upstream axial velocities on the windward side of the hub are reduced, and the downstream recirculating flow in the critical region does not experience as great a radial deflection as seen in the maximum loading case ($\beta = 0.23$), shown by Figure 46 for $\beta = 0.26$. The radial flow and, correspondingly, the Coriolis force contribution within the critical region is lessened and the decline in the peak bending moment is witnessed.

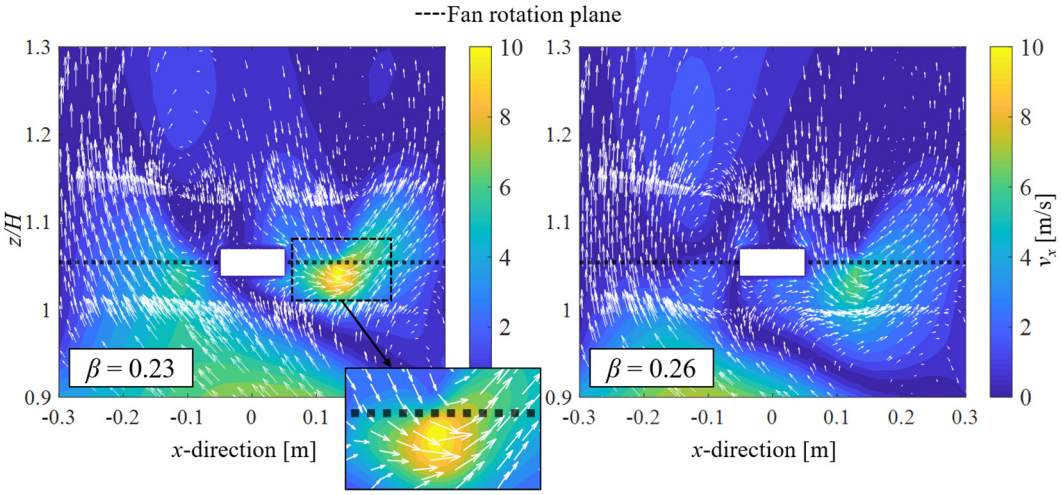

Figure 46: Visualization of the mid-plane velocity vector fields through the edge fan rotation plane, showing the interaction between up- and downstream flow features (coloured by absolute *x* (radial) velocity)

In the radial velocity plots of Figure 45, at $\beta = 0.26$ (point at which the decline in the loading occurs) it can be seen that the high radial flow velocities have shifted from the critical region into the fourth quarter of the rotation cycle. Figure 47 shows the total pressure contours ahead of the edge fan at $\beta = 0.23$ (clipped at -25 Pa for visualization) and illustrates that there exists an asymmetry to the upstream separated flow region. Therefore, it is suspected that similar reasoning holds for the exacerbation of the radial flow in the fourth quarter at $\beta = 0.26$, it is just that the interaction between the up- and downstream flow regions is occurring along different azimuthal coordinates. However, the tangential velocities within the fourth quarter of the rotation plane are not as great as those in the critical region. Therefore, even with the high radial velocity contribution, the loads are not as great; hence, the decline in the peak loading.

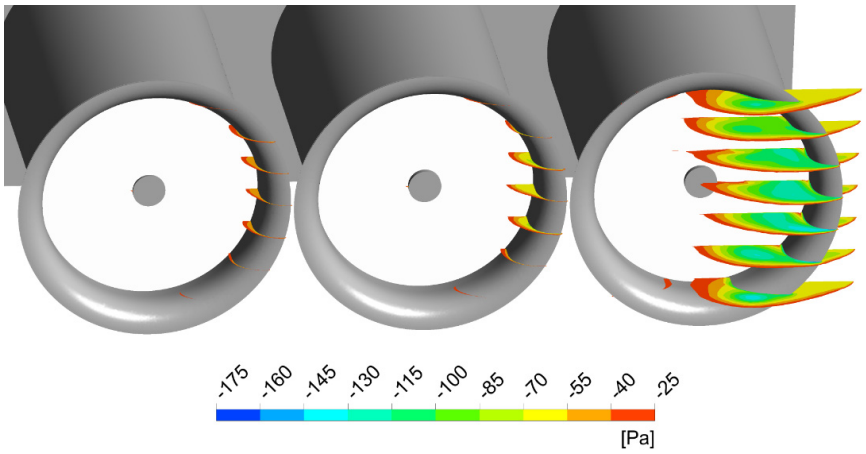

Figure 47: Total pressure contours ahead of fan platform showing asymmetry of separated flow region around edge fan bellmouth (β = 0.23, no windscreen)

The peak bending moment (Figure 39) then continues to rise from $\beta = 0.3$ following the momentary decline as the flow rate through the fan is reduced further with the continued growth of the separated flow region. The lowering fan flow rate also re-establishes high radial flow velocities in the critical region of the fan face, as observed in the radial flow plot for $\beta = 0.33$ in Figure 45.

The dynamic bending moment (M_D) results are dependent on the variance of the azimuthal bending moment distributions. As noted, there exists an asymmetry to the separated flow region that develops across the fan face. Therefore, localized portions of the fan face are subject to differing pressure and velocity conditions as the separated flow region develops. The large dynamic bending moments near $\beta = 0.23$(Figure 38) are considered to be likewise linked to the above detailed phenomenon, as the radial flow (and its effect on the magnification of the aerodynamic loads) only occurs over concentrated portions of the fan face, which extends the range between the maximum and minimum azimuthal bending moments, and the overall variability of the load distributions.

Following the maximum dynamic load at $\beta = 0.23$, the velocity fields through the face become more uniform (as seen in Figure 45 for $\beta = 0.33$). The greater inlet velocity uniformity corresponds to greater uniformity in the flow's angle of attack and, hence, the dynamic loading reduces.

Understanding of this discussion on the peak and dynamic loading behaviour is facilitated through an examination of the resultant azimuthal bending moment variations (described earlier in Figure 41) at increasing cross-flow rates, shown in Figure 48. The resultant azimuthal bending moment distributions in Figure 48 are normalized through division of the maximum resultant bending moment (M_R^*) present at the no-wind ($\beta = 0.1$) scenario.

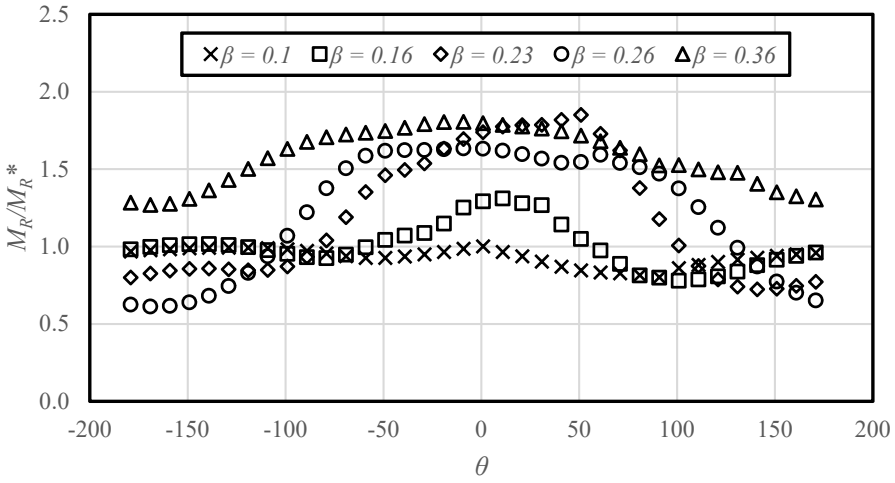

Figure 48: Resultant azimuthal bending moment variations at different cross-flow rates (no windscreen)

The phenomena detailed earlier in this section is repeated here, but now with reference to Figure 48. In Figure 48, it is observed that there is an increase in the peak loading with increasing cross-flow in accordance with the trend depicted in Figure 38 (maximum peak at $\beta = 0.23$, followed by a slight decline at $\beta = 0.26$ then continued increase up to $\beta = 0.36$). The increase in the peak loading corresponds to the lowering fan flow rates and, correspondingly, the pressures within the developing separated flow region. The large peak at $\beta = 0.23$ occurs due to the high radial flow presence within the critical region. Following the maximum peak at $\beta = 0.23$, the radial flow constituent in the critical region is weakened, so the drop in the peak loading at $\beta = 0.26$ occurs. However, the peak loading continues to increase again thereafter due to further development of the separated flow region and the re-establishment of high radial flow velocities in the critical region that accompanies the lowering fan flow rates.

It is also observed that the high midsection loading portions of the profiles widen as the cross-flow increases. This is due to the separated flow region spanning across an increasing percentage of the fan face, until it effectively bypasses the edge fan completely and near uniform inlet velocity profiles are established (seen in Figure 44 at $\beta = 0.33$). Hence, the loading becomes more uniform and there is a corresponding decline in the dynamic loading component.

6.2.2 Effect of cross-flow on blade loading with windscreens

The effect of incorporating peripheral windscreens is addressed within this subsection. For this component of the study, only the effect of the 50% solidity material ($\epsilon = 0.5$) and the effect of windscreen height is addressed. The $\epsilon = 0.5$ material was chosen based on the ability of the numerical model to deliver the best numerical fan performance prediction (Section 6.1) when configured with this

screen material. The numerically and experimentally determined effect of the cross-flow on blade loading with windscreens at varying heights is shown in Figure 49.

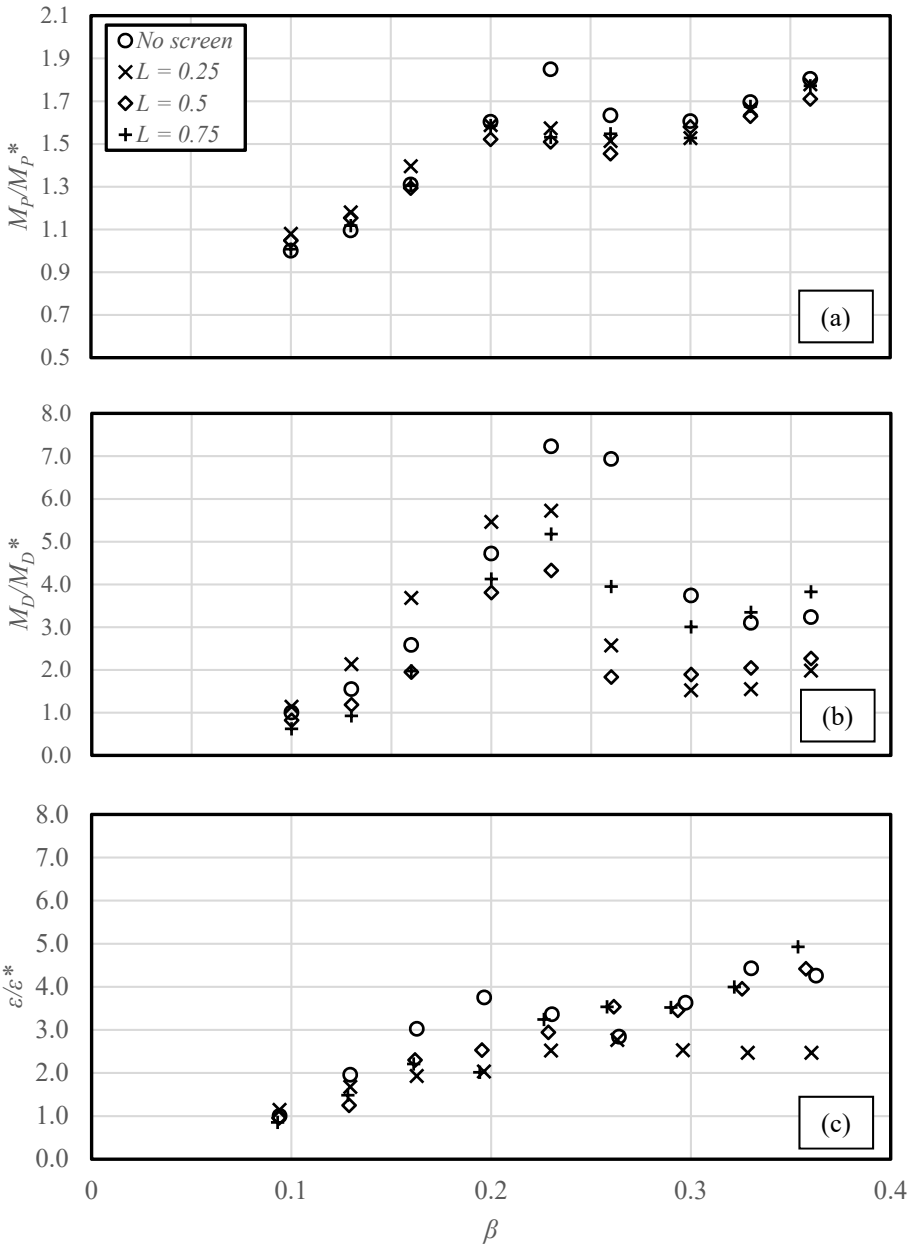

Figure 49: Effect of cross-flow on edge fan blade loading ($\epsilon = 0.5$): (a) peak bending moment (b) dynamic bending moment (c) dynamic strain (Marincowitz, 2018)

In the numerical results, the screen at $L = 0.75$ reduces both the peak and dynamic loading at low and intermediate cross-flow rates, but increases dynamic loading slightly at high cross-flow rates; the same trend is evident in the experimental results. The screen at $L = 0.25$ is seen to initially increase both the peak and dynamic loading notably (differing markedly from the experimental trend), but then offer considerable reductions in dynamic loading and slight reductions in peak loading from $\beta > 0.2$. The screen at $L = 0.5$ appears to always reduce the peak and dynamic loading. The $L = 0.5$ case offers similar dynamic loading benefits to the $L = 0.25$ case at high cross-flow rates. The numerical dynamic loading trend for the $L = 0.5$ case is largely representative of the experimental results; however, in the experimental results there is a brief increase in loading near $\beta = 0.25$ and the benefits at the higher cross-flows are subtle. Further discussion on possible reasons for the mismatch between the numerical and experimental results follows in Section 6.2.3.

Expectedly, the dips in the loading relationships occur at lower cross-flow rates when the screens are present. This is consistent with the earlier discussion on the mechanism that brings about this reduction. The presence of the screen enlarges the upstream low pressure zone ahead of the edge fan (shown in Section 6.1) and, resultantly, the recirculation of the downstream flow in the windward half of the fan rotation plane happens at a lower cross-flow rate.

Furthermore, while the screens extend the low pressure region further across the edge fan face, lower localized pressure zones are formed near the immediate upstream portion of the bellmouth wall in the absence of a screen (as discussed in Section 6.1). With no screen present, the approaching flow strikes the bellmouth lip at greater cross-flow velocities and the pressure in the detached flow region is resultantly lower. This produces more severe pressure differentials across and through the fan rotation plane which generates greater loads; hence, the greater load variability and magnitudes in the no screen case.

Marincowitz (2018) observed a linear dependence between the dynamic loading (strain) and negative difference between the mean velocity into the windward and leeward halves of the edge fan face (measured along a mid-plane $0.21d_f$ ahead of the fan platform), described by Equation 6.8.

$$\delta_z = \bar{\delta}_{z,w} - \bar{\delta}_{z,l} \tag{6.8}$$

where δ_z is the mean velocity difference, and $\bar{\delta}_{z,w}$ and $\bar{\delta}_{z,l}$ the velocities into the windward and leeward halves of the fan face respectively.

Marincowitz (2018) hypothesized that the dynamic loading can be interpreted from a knowledge of the inlet velocity profile distribution. This hypothesis holds clearly in the numerical case with respect to the determined peak bending moment data, as shown in Figure 50(a), but to a lesser extent for the dynamic loading data, shown in Figure 50(b). This is, however, consistent with the previous note (Section 6.2.1)

that a better experimental representation is uncovered through the peak bending moment to cross-flow relationship. The data points in Figure 50 have been taken at β = 0.1, 0.16, 0.2, 0.26 and 0.33. Figure 50 shows that once the mean velocity difference becomes negative ($\beta \sim 0.2$), a definite proportional relationship between the loading and velocity difference is apparent. This also provides further reasoning for the larger load magnitudes in the no screen case.

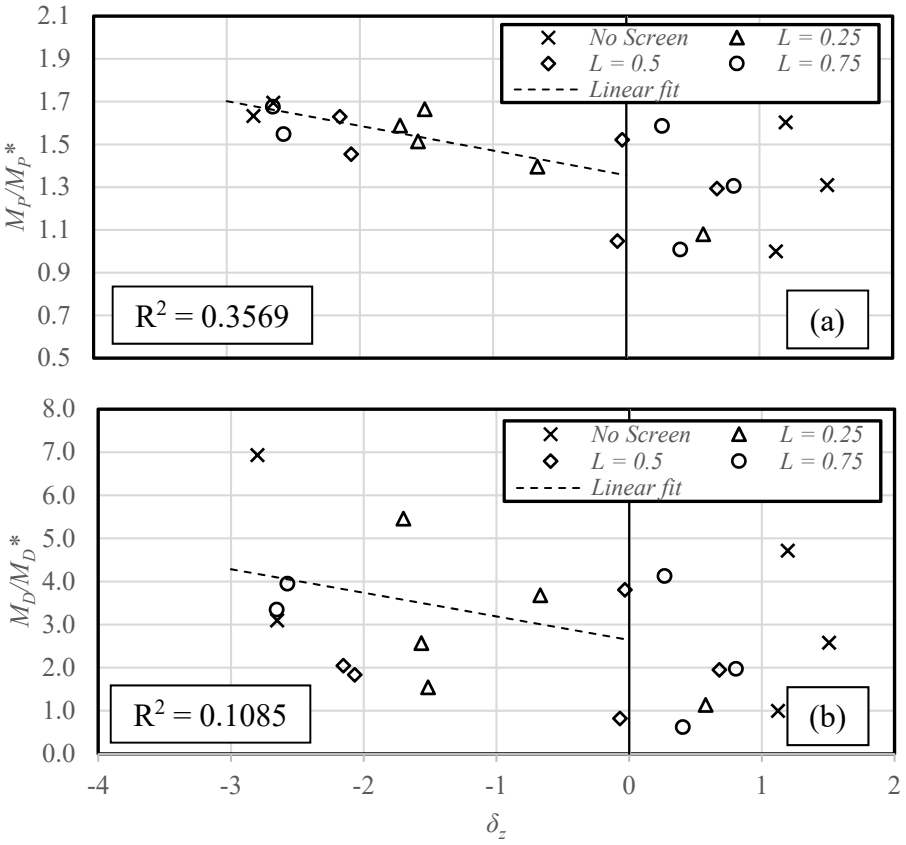

Figure 50: Blade loading dependency to mean axial velocity difference: (a) peak bending moment (b) dynamic bending moment

Returning to Figure 49, interpretation of the presented results is aided through inspection of the resultant azimuthal bending moment distributions for windscreen cases, depicted in Figure 51. Relative to Figure 48 (azimuthal distribution for the no screen case), it can be seen that the general effect of the windscreens is to produce more uniform and symmetric loading profiles. This resultantly lowers the dynamic loading component and is more prevalent at the higher cross-flow rates. The grey dashed lines on the graphs in Figure 51 indicate the maximum and minimum normalized resultant bending moment magnitudes for the no screen case.

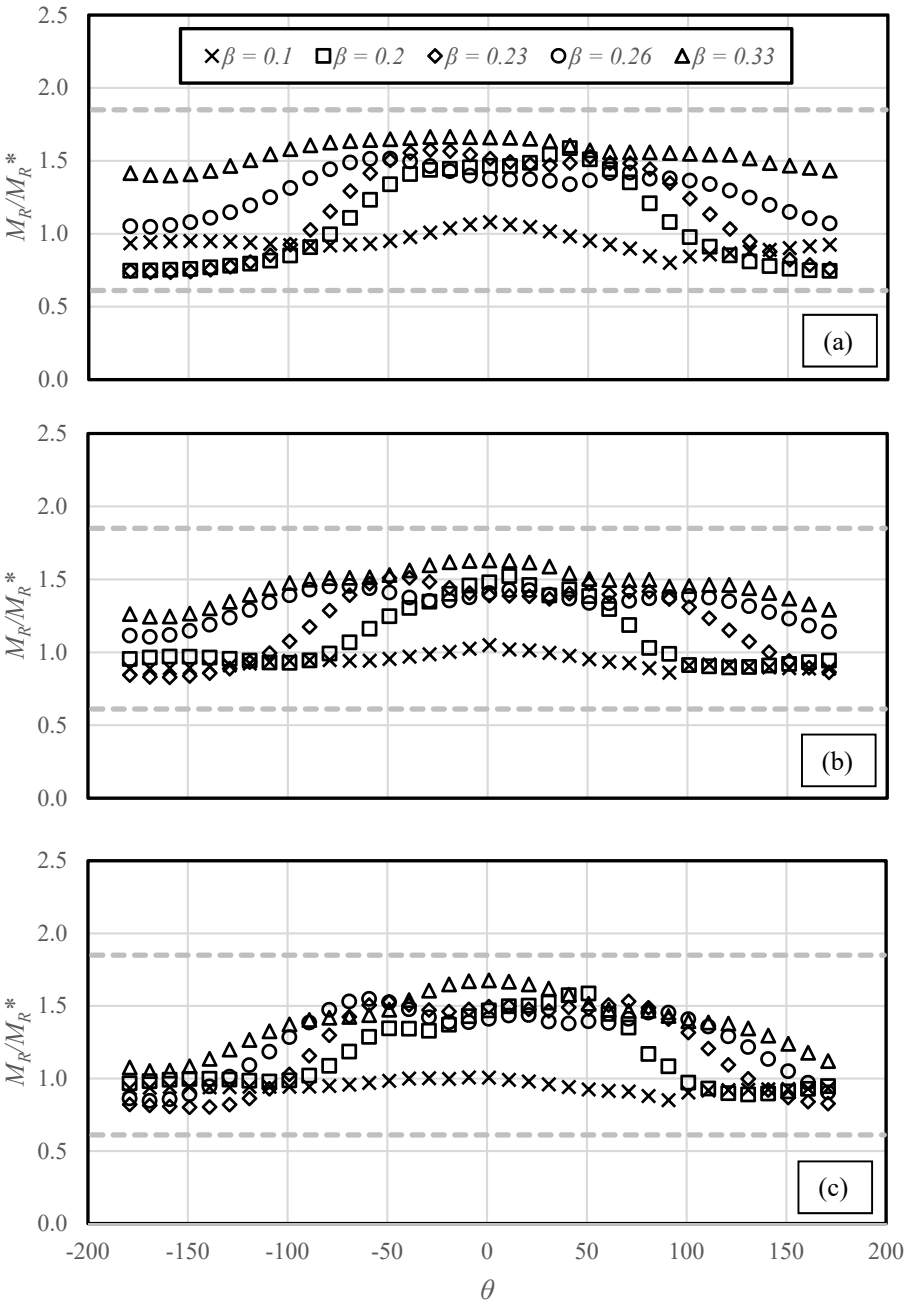

Figure 51: Resultant azimuthal bending moment distributions at different cross-flow rates ($\epsilon = 0.5$): (a) $L = 0.25$ (b) $L = 0.5$ (c) $L = 0.75$

This greater uniformity in the loading distributions is coupled to greater uniformity of the inlet velocity profiles into the fan face, as shown in Figure 52 (taking the screen height of $L = 0.5$ as the representative case). In Figure 52, this greater uniformity is particularly evident by the more centrally positioned hub wake regions relative to that seen in Figure 44. Consistent reasoning was provided by Maulbetsch and DiFilippo (2018) and Heinemann and Becker (2017).

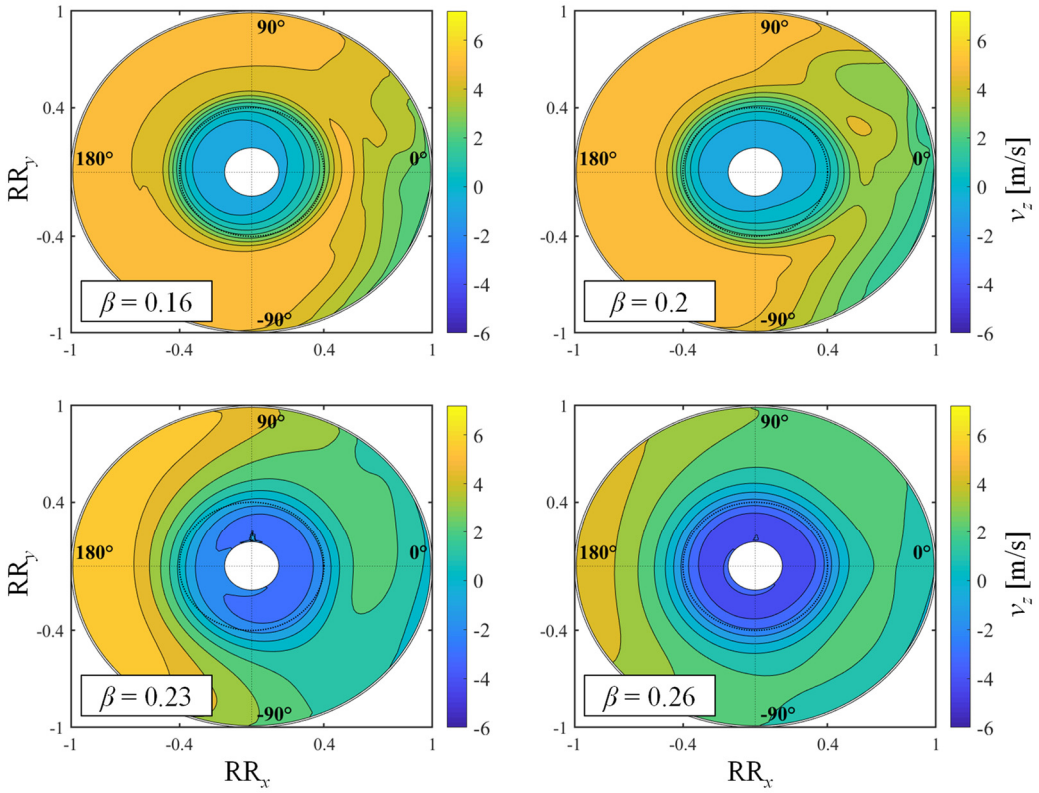

Figure 52: Axial velocity distributions through edge fan rotation plane at increasing cross-flow rates (ϵ = 0.5, L = 0.5)

6.2.3 Assessment of the EADM's ability to analyse blade loading

It has been shown that the EADM is able to deliver qualitative prediction of the dynamic loading trends to a reasonable degree; however, the lack of a strong correlation between the numerical and experimental results warrants further assessment of the appropriateness of using the EADM in an investigation into aerodynamic blade loading. While the exact correlation between aerodynamic loading and strain is not known and is a potentially dominant contributor to the discrepancy between the results, this subsection attempts to evaluate the contribution based on the EADM's performance.

This additional assessment of the EADM's ability to accurately predict blade loading results is done through inspection of the determined load profiles along the azimuthal coordinates of the maximum resultant bending moments (white lines show on Figure 40) at different cross-flow rates for the no screen case. Example load distributions are shown in Figure 53.

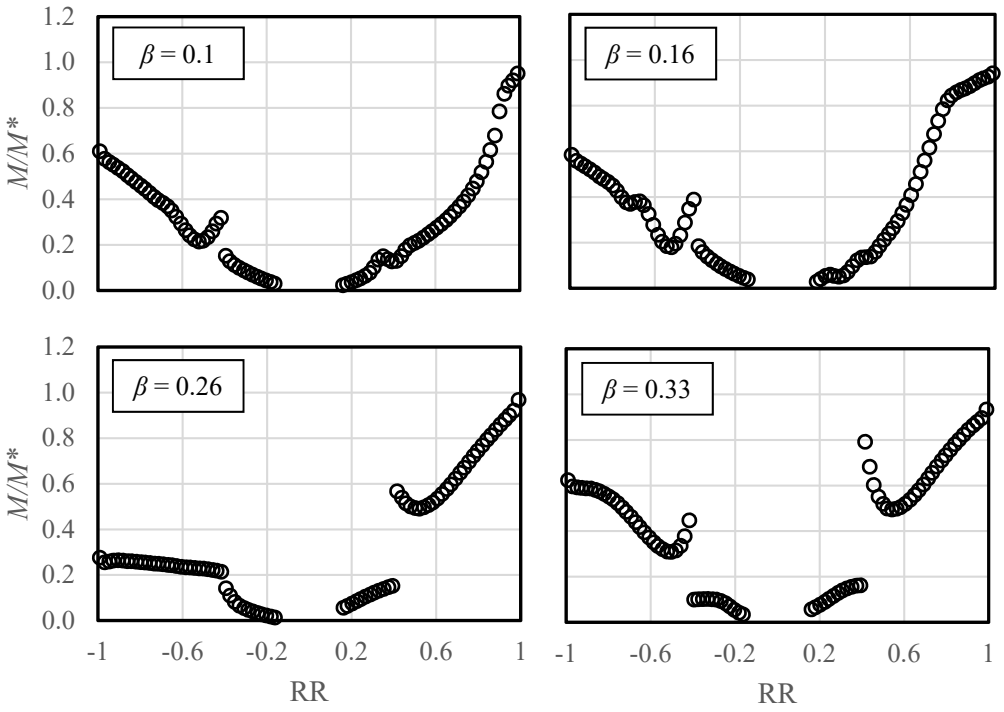

Figure 53: Load distributions across azimuthal coordinates of maximum resultant bending moments at increasing cross-flow rates (no windscreen)

Figure 53 shows that stark, non-physical discontinuities exist in the determined load distributions over the RR of 0.4 in each case. At a RR of 0.4, the modified lift and drag coefficients of the EADM take effect (as discussed in Section 3) and a pronounced step in the determined loads occurs across this zone. The load distributions predicted by the employed EADM are, therefore, not an accurate representation of the physical case, so the accuracy of the prior presented results is unfortunately limited in this regard.

Considering that the maximum moments occur at the blade tip, which is both removed from the discontinuities across the limiting RR and not dependent on the span-wise distribution, the EADM should be able to predict peak bending moment information fairly accurately. However, not possible to confirm this assumption, as only the experimental dynamic loading information given in Marincowitz (2018) is available for comparison; and the correlation between aerodynamic input and strain response remains obscure. It is, therefore, recommended that future studies investigate this assumption.

The discontinuities in the loading profiles highlight the need for an implicit fan model method that better captures blade loading effects under high cross-flow conditions. Investigation into alternative existing fan models or the formulation of a novel fan model for the use in characterizing blade loading under cross-wind conditions is, therefore, also suggested for future research.

6.2.4 Summary of the blade loading analysis

The effects of cross-flow on edge fan blade loading with and without windscreens were investigated in this section. Numerically determined aerodynamic bending moment information was compared to experimental strain measurements. It was noted that direct comparison between the numerical and experimental results is challenging as the parameters used to characterize blade loading were inconsistent. While it is inferred that reasonable correlation between the numerically determined bending moment information and experimental strain measurements should exist, the exact relationship between the two is not currently known for this case. Interestingly, it was noted that the trend of peak bending moment to increasing cross-wind was more akin to that of the dynamic strain measurements, over the trend produced when considering instead dynamic bending moment. Future research is, therefore, encouraged to explore reasons for this observation.

Cross-flow was found to increase both peak and dynamic bending moments up to $\beta = 0.23$ ($v_w \sim 6$ m/s, Equation 6.2), after which a decline and then continued increase followed. Promisingly, a similar trend is seen in the experimental strain measurements; however, the dynamic loading magnitudes and the cross-flow rates at which the declines occur are significantly offset. The loading trends were found to be strongly linked to the variability of the radial flow velocities in the windward portion of the edge fan's rotation plane. This variability was found to be caused by the interaction of the upstream separated flow region with the downstream recirculating flow region near the fan hub.

The windscreens were seen to primarily reduce both peak and dynamic loading. This was found to be attributable to the windscreens creating more uniform inlet flow profiles in the edge fan. Consistent reasoning was given by Heinemann and Becker (2017), and Maulbetsch and DiFilippo (2016).

A strong correlation between the numerical and experimental results was, however, absent and this prompted further assessment of the EADM's ability to accurately predict blade loading profiles under high cross-flow conditions. In this supplementary assessment, determined load profiles at some sample cross-flow rates were extracted and found to be unrealistic. This highlighted the need for a different or even novel implicit fan model that can be used to better investigate the effects of cross-flow and peripheral windscreens on ACC fan blade loading.

The conclusions within this section are also limited to the particular case investigated, as the influence of changing platform height, fan row edge effects and differing fan blade profiles have not been accounted for. The findings within this section, however, form a solid foundation upon which the suggested future research can be based. Future research is also encouraged to further unpack the postulated reasons for the reduction in the loading relations at intermediate cross-flow rates.

6.3 Influence of platform height on windscreen effects

In the prior analyses, it was mentioned that the conclusions are limited to the specific case investigated due, in part, to the influence of fan platform height having not been considered. Therefore, in an attempt to establish whether or not the previous findings are generalizable for any platform height, a preliminary assessment of the windscreens' effects in conjunction with changing platform height is offered in this section.

6.3.1 Platform height influence on fan performance effects

Modifications to the numerical model's geometry were made so that changes in platform height could be effected. The ducted inlet and outlet exhaust space were replaced by extension of the two-dimensional flow channel beneath the fan platform up- and downstream of the fan row, creating an external flow domain similar to the likes of Bredell (2005). Figure 54 shows the modified numerical geometry and how the floor height was extended in each case (the extended segments were removed from the numerical geometry when analysing the lower platform cases). The sides of this extended flow channel were specified to be symmetry planes while the opposing surface to the fan platform, 'the floor', was made to be a walled boundary. The domain was extended ~6 hydraulic diameters (based on the highest investigated platform height) upstream of the fan row in order to eradicate any potential inlet velocity profile development implications.

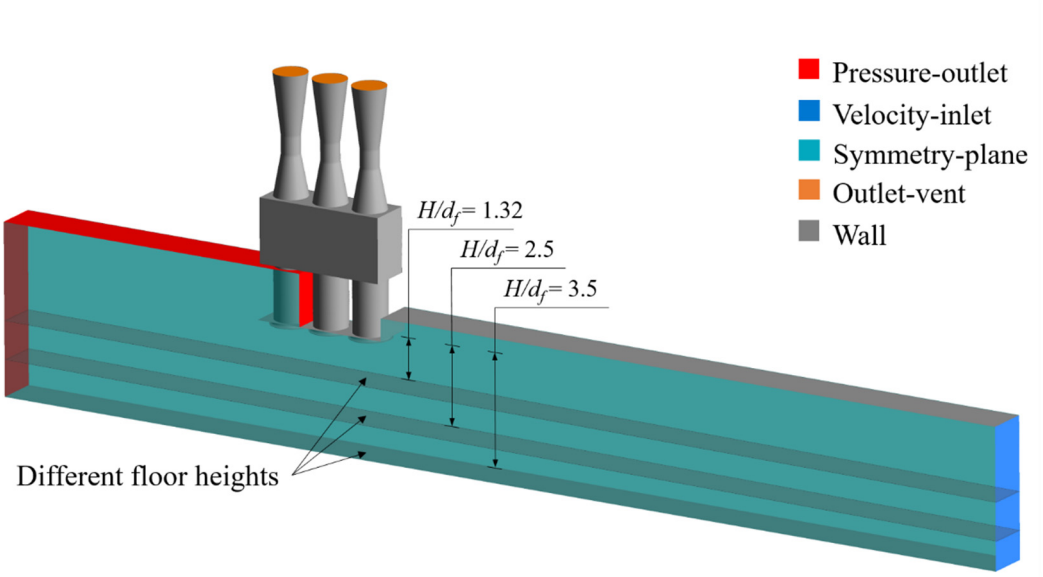

Figure 54: Numerical geometry for the changing platform height investigation

The height of the top upstream flow space boundary, relative to the fan platform, was left unchanged and kept as a walled boundary (consistent with the experimental facility simulations (Section 5)). It is known that as the platform height is adjusted, different peripheral inlet velocity profiles develop (van der Spuy, 2011). This boundary should, therefore, ideally change depending on the platform height and applicable cross-flow condition. However, for the purposes of this preliminary assessment, it was considered sufficient to maintain the top boundary as a fixed walled surface.

To compensate for this limitation, the assessment is made based on relative performance difference. For each platform height considered, the effect of the windscreens on system volumetric effectiveness (expressed as a percentage difference) relative to the respective no screen scenario is determined. The inlet boundary was specified as a velocity inlet and adjusted so that the same average velocity beneath the fan platform could be established in each case. The 50% solidity ($\epsilon = 0.5$) windscreen material was again used and the effect of windscreen height addressed. Three platform heights were considered ($H/d_f = 1.32$, 2.5 and 3.5). This assessment attempted only to uncover whether platform height would influence the observed windscreens effects; therefore, the investigated platform heights were arbitrarily selected. The ensuing results are presented in Figures 55, 56 and 57.

Through this preliminary assessment, it is seen that the platform height has a definite influence on the fan performance related windscreen effects. While the primary effect of the windscreens remains to negatively impact fan row performance (up to the maximum wind speed investigated); the beneficial influence of the higher screen height cases ($L \geq 0.5$) takes effect at lower cross-flow rates at the increased platform heights.

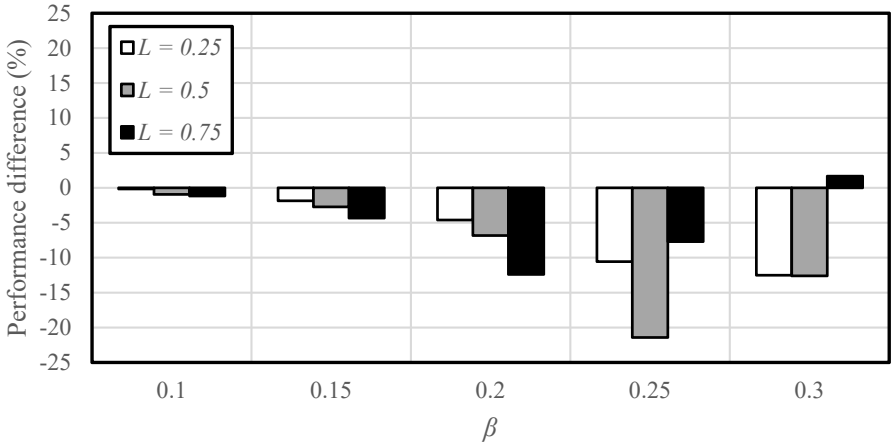

Figure 55: Effect of cross-flow on system performance relative to the no screen case, $H/d_f = 1.32$ ($\epsilon = 0.5$)

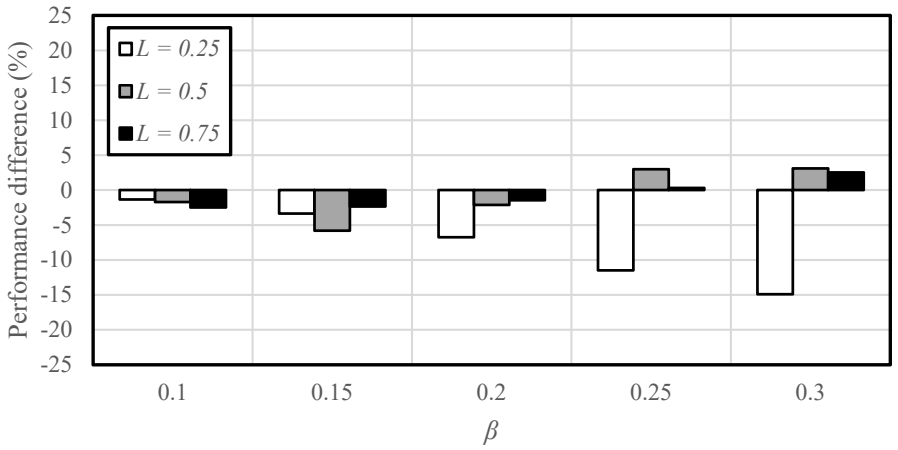

Figure 56: Effect of cross-flow on system performance relative to the no screen case, H/d_f = 2.5 (ϵ = 0.5)

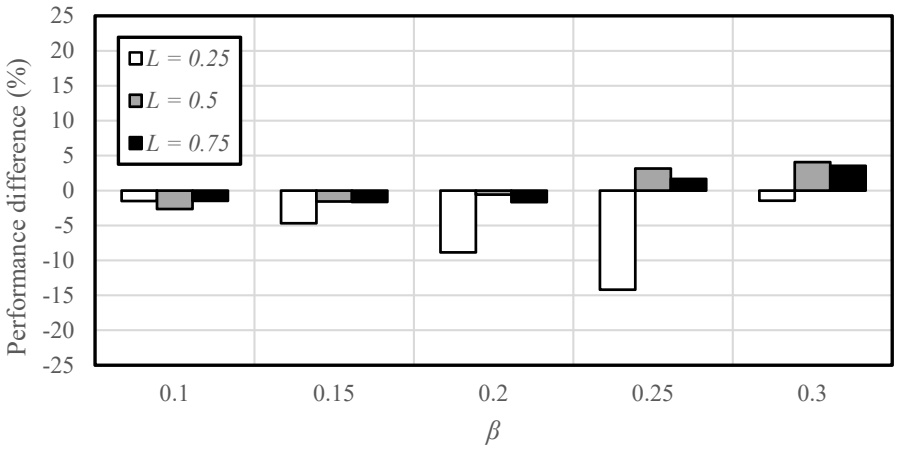

Figure 57: Effect of cross-flow on system performance relative to the no screen case, H/d_f = 3.5 (ϵ = 0.5)

Figure 58 shows the flow fields beneath the fan platform at β = 0.25 with the screen at a height of L = 0.5 for each platform height case. Similar observations to that discussed in Section 6.1 are apparent in Figure 58. In the higher platform cases, the large area screens are successful in reducing the velocity of the approaching cross-flow while still allowing sufficient flow to permeate through the screen and not choke the edge fan. Furthermore, the accelerated flow regions beneath the screens are farther removed from the fan inlet regions and, hence, do not experience as great an axial deflection into the fan row (relative to the H/d_f = 1.32 case). The high speed flow regions therefore bypass the fan row (made possible due to sufficient permeation of the flow through the large area screens) and the cross-flow velocities immediately upstream of the second and third fan are reduced, recovering the static pressure beneath these fans and their performance. The higher static pressure and

axially drown downstream flow then assists in reducing the separated flow/low pressure region across the edge fan which suspectedly also boosts the performance of the edge fan. Likewise, more uniform velocity profiles are established in the wake of the screen in the higher platform cases and, resultantly, there are less pressure loss mechanisms.

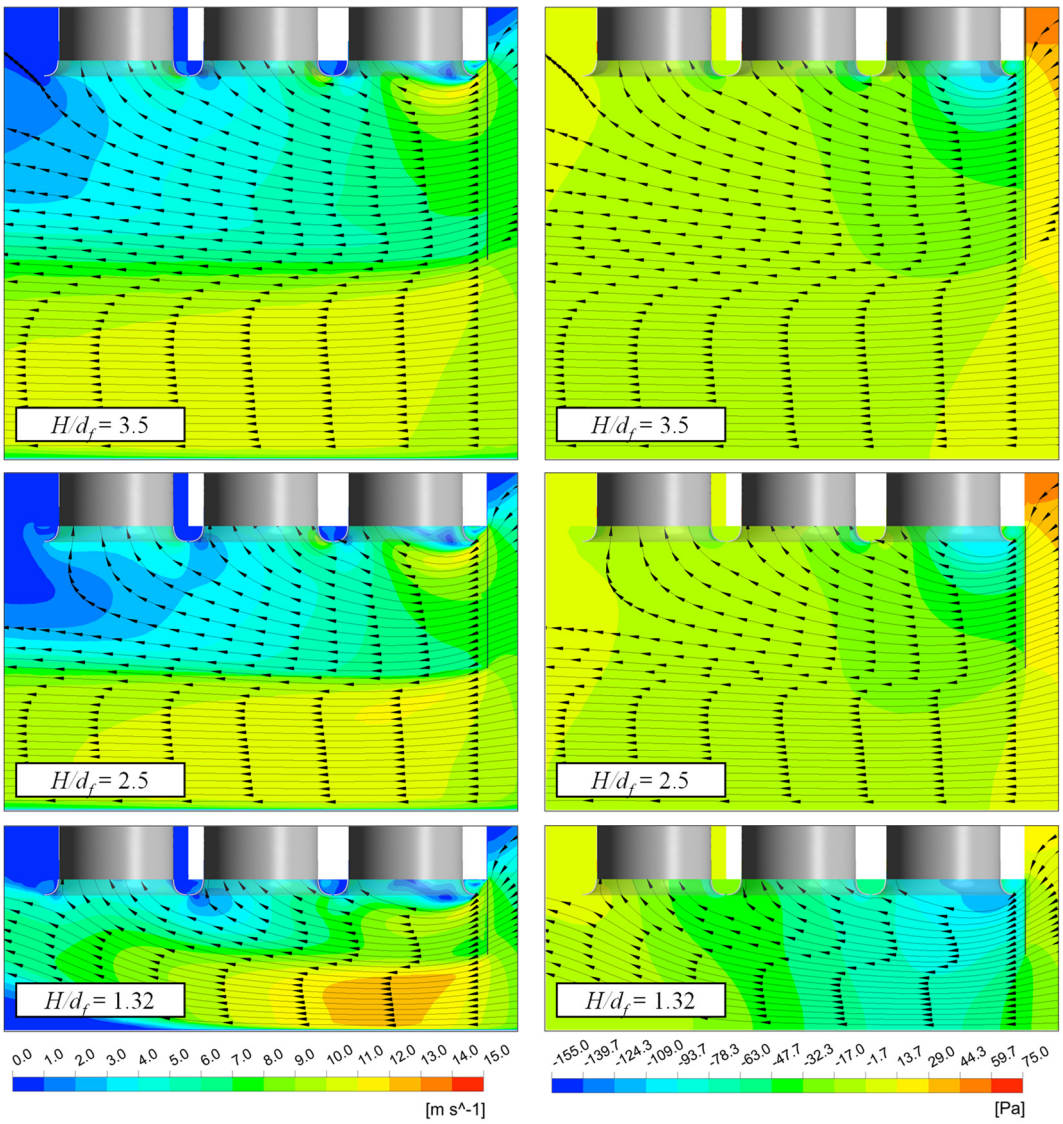

(a) (b)

Figure 58: Visualizations of the flow fields beneath the fan row at different platform heights (β = 0.25, L = 0.5): (a) Velocity magnitude contours (b) Static pressure contours

The determining factor underpinning the beneficial offering of the windscreens, therefore, appears to be based on the ability of the screens to sufficiently divert the

high-speed flow region that forms beneath them past the fan row. Once achieved, further extension of the screen or platform height is not expected to offer any substantial improvements to fan row performance.

These results highlight that both windscreen height, platform height and wind speed are important considerations in the assessment of windscreen effects. It is suspected that platform height and wind speed differences underpin the discrepancy between the results of the investigations discussed in Section 2. For instance, the investigation by Zhang and Chen (2015) concerned an ACC of very tall platform height ($H/df > 3.5$) subjected to a platform height wind speed of approximately 10 m/s. This positions the case in a condition in which the windscreens would likely prove favourable (based on the trends in Figures 55, 56 and 57); hence, the reported enhancement in fan performance. An investigation concerning an ACC of lower platform height or wind speed may fall outside of the beneficial range, e.g. Bredell (2005), and Maulbetsch and DiFilippo (2016).

6.3.2 Platform height influence on blade loading effects

The effects of windscreens in conjunction with changing platform height on blade loading was also reviewed, taking the screen height of $L = 0.5$ as a representative case. The blade loading information is presented in Figure 59.

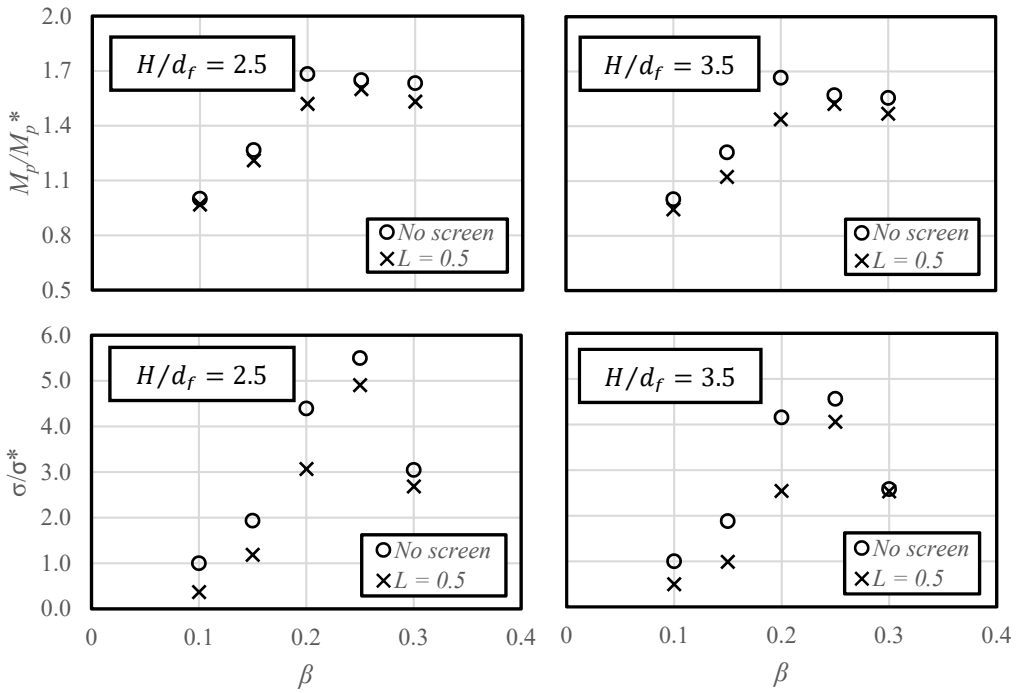

Figure 59: Effect of cross-flow on blade loading at different platform heights: (Top) peak bending moment (Bottom) dynamic bending moment

Promisingly, similar trends are uncovered in the higher platform cases to that witnessed in Section 6.2. Both peak and dynamic loading exhibit the same initial increase, followed by a reduction thereafter. In all cases, the windscreen at $L = 0.5$ offers favourable reduction of both dynamic and peak loading relative to the no screen scenario. Consequently, it appears that the results of the experimental blade loading analysis are arguably representative of the general case. However, such appraisal based on the presented numerical results is cautioned, on account of the discussed limitations of the EADM (Section 6.2.4) and the simplification of the peripheral inlet conditions. The loading behaviour may also be limited to the applicable L2-fan used in these simulations. The observed loading behaviour, discussed in Section 6.2, has been recognized to be strongly dependent on the radial flow velocities that develop over the fan face under increasing cross-flow. The radial velocities develop due to the interaction between the up- and downstream recirculating flow features near the fan hub. It is, therefore, suspected that fan type, particularly fan hub-to-tip ratio, will have a pronounced effect on the loading relationships. Future research is therefore encouraged to repeat this analysis using different fan types to further establish the generalizability of these results. Nonetheless, the results presented here suggest that blade loading related windscreen effects are less dependent on platform height in comparison to the fan performance effects.

6.3.3 Summary of platform height influence

The influence of platform height on the windscreen effects was evaluated in this section. This was done by modifying the experimental facility model so that different platform heights could be simulated.

Platform height was found to have a considerable influence on the fan performance related windscreen effects. It was uncovered that the windscreens become beneficial at lower cross-flow conditions with taller platform heights. This observation potentially explains the inconsistency in the literature regarding the effect of windscreens (Section 2). The results show that peripheral windscreens may prove beneficial in investigations concerning ACCs of high platform height and high wind speeds, while the windscreens may be harmful in investigations on lower platform heights and/or wind speeds. The results, therefore, highlight that platform height and wind speed are important considerations in the assessment of peripheral windscreen effects.

Blade loading effects were found to be largely independent of platform height. In each case, the windscreen at $L = 0.5$ always reduced the dynamic and peak bending moment components, as similarly observed in Section 6.2.

7 Conclusions and recommendations

7.1 Summary of study

This study numerically replicated and extended the experimental analysis of Marincowitz (2018), and validated numerical modelling techniques for the purpose of analysing peripheral windscreen effects on ACC fan performance and dynamic blade loading. The validated techniques were then used to provide key insights into the experimental phenomena and partially settle the uncertainty in the literature surrounding the impact of windscreens.

The resultant numerical model was found to be able to deliver quantitative prediction of windscreen effects on fan row performance for low and moderate cross-flow conditions (up to an equivalent full-scale platform height wind speed of approximately 9 m/s). However, at higher cross-flow rates, the accuracy of the numerical model deteriorated significantly due to the limitations of the employed implicit axial fan models.

For the particular case investigated, the windscreens were found to have a primarily negative impact on ACC fan row performance. Insight into the fan performance related windscreen effects included the detection of a low pressure wake that develops behind the screens under windy conditions, caused by deflection of the incoming flow nearer to the ground and farther downstream. For the discussed cases, an inversely proportional relationship between system volumetric effectiveness and windscreen solidity was observed. It was found that as the solidity is increased, the size of the low pressure wake that develops behind the screen is exacerbated. The effect of windscreen height was also reviewed. For a 50% solidity material, slight fan row performance enhancement (< 1% improvement) is offered at high cross-flow rates (from an approximated full-scale platform height wind speed of 12 m/s) with a high windscreen height (75% coverage of the peripheral inlet area). At these high cross-flow rates, the high 50% solidity windscreen increases the static pressure beneath the fan row due to the screen sufficiently diverting the high speed inlet flow past the fan row.

An assessment of the numerical model's ability to capture the experimental edge fan blade loading results then followed. Numerically determined peak bending moment and dynamic bending moment information were compared to the experimental strain measurements of Marincowitz (2018). Similar trends in loading behaviour were uncovered between the numerical and experimental results. The dynamic bending moment (all cases) was found to initially increase at low cross-flow rates, dramatically decline at intermediate cross-flow rates and subtlety increase again at high cross-flow rates. Likewise, the peak bending moment was shown to follow a similar initial increase, proceeded by a momentary decline then continued increase. The loading trends were found to be strongly linked to the variability of the radial flow velocities in the windward portion of the edge fan's

rotation plane. The reduction in both the peak and dynamic loading at intermediate cross-flow rates was attributed to the reduction of the radial flow velocities in the first quarter portion of the edge fan's rotation plane. Just prior to the respective declines, the interaction of the upstream separated flow region and the hub wake region in the windward half of the fan face produces pronounced radial flow velocities (Coriolis force) within the first quarter region (the region where the greatest angles of attack and tangential velocities reside), which results in high loading conditions. However, as the cross-flow rate increases further, the radial flow, and correspondingly the Coriolis force contribution, is weakened and the reduction in loading witnessed. Following the declines, the loading increases again due to the fan flow rates (and the static pressure) lowering further with continued development of the separated flow/low pressure region.

Windscreens were found to primarily reduce edge fan dynamic loading. The general reduction in dynamic loading was attributed to the establishment of more uniform and symmetric velocity profiles into the edge fan face. While the exact correlation between aerodynamic bending moment and strain is not known for the current case, notable differences between the numerical and experimental results raised suspicion regarding the validity of the EADM to capture blade loading effects. An assessment of the determined load profiles for some representative cases highlighted that the EADM predicts non-physical radial loading discontinuities. It was, therefore, established that the EADM is not well-suited for dynamic blade loading analysis. Further research into alternative or novel axial fan models for this purpose is, therefore, encouraged.

This study made no attempt to extend the numerical analysis into full-scale simulations, so as to richly detail the experimental observations (albeit for a limited scenario) and comprehensively assess the validity of the numerical techniques. A preliminary assessment of the influence of platform height on the windscreen effects was, however, considered to establish a sense of the generalizability of the experimental results.

Resultantly, platform height appears to have a definite influence on fan performance related windscreen effects and a lesser influence on blade loading effects. It was again determined that a peripheral windscreen can offer improved fan row performance once the accelerated flow region beneath its length is sufficiently deflected past the fan row. Passage of the high-speed flow region past the fan row enables slower and more uniform velocity profiles to be established in the wake of the screen, which increases the static pressure ahead of the fan row and encourages fan performance. This condition is attainable at lower wind speeds with a taller platform height. Peripheral windscreen effects therefore appear to be dependent on platform height, wind speed and windscreen height (the screens may or may not enhance performance depending on these parameters). This observation offers a partial explanation for the inconsistency in the literature surrounding the impact of windscreens.

The generalizability of the results, however, remains in question due to the two-dimensional inlet flow assumption inherent within the model. The influence of fan row edge effects, therefore, remains obscure. It was also noted that the blade loading results may be more strongly influenced by the fan type, so it is recommended that the analysis is repeated using different fans.

Conclusively, it has been shown that quantitative assessment of windscreen effects on fan row performance is realizable, while qualitative assessment of blade loading effects is likewise possible using the presented modelling techniques. Follow on studies are now encouraged to either extend these techniques to full-scale analyses or to derive alternative axial fan models that can be used for quantitative assessment of the effects at higher cross-flow conditions.

7.2 Recommendations for future work

The shortcomings inherent within this study are embedded within the above discussion. Recognition of these shortcomings gives rise to a number of recommendations for future works that wish to continue/build upon this study. The key recommendations are listed below.

1. Explore alternative implicit axial flow fan models, or use the presented data to construct a novel fan model for better representation of blade loading and fan performance effects at high cross-flow conditions. It is believed that explicit modelling of the edge fan is possible. Simulations using an explicit edge fan formulation can be used to derive and appraise a new implicit model.

2. Characterize the correlation between aerodynamic loading and strain through FSI simulation. This is necessary to enable better comparisons to be drawn between the experimental and numerical blade loading analyses.

3. Extend the presented modelling techniques to full-scale simulations to allow for case-specific analysis of windscreen effects with resultant increased practical value.

4. Characterize how peripheral inlet profiles change with platform height and wind speed, then use that knowledge to modify the model's geometry to better explore the dependency of the windscreen effects on fan platform height.

5. Repeat the presented analyses using different fan types. This is necessary to establish whether the observed effects are generalizable across fan type.

6. Incorporate additional fan rows into the simulations to model fan row edge effects. This is necessary to address the shortcoming of the two-dimensional inlet flow assumption inherent in this study's model.

Appendix A Overview of numerical infrastructure

An overview of the numerical methods used in this study is presented in this section. While the body of CFD related analysis techniques and methodologies is vast, the discussion here has been limited to give only a brief overview of that applicable to the current study.

A.1 Governing equations

In the absence of heat transfer and compressibility effects, fluid flow is governed by the following system of partial differential equations, describing mathematically the conversation principles of mass and momentum. The applicable equations are expressed below in a fourth-dimensional Euclidean time-space coordinate system using index notation.

The scalar continuity equation governing the conservation of mass for an incompressible fluid is presented without derivation in Equation A.1 (Schobeiri, 2010).

$$\nabla \cdot \vec{v} = 0 \tag{A.1}$$

The velocity vector $\vec{v}$ can be expanded into its components as $\vec{v} = v_1 + v_2 + v_3$, where the subscripted numerics designated the principle spatial coordinates in three-dimensional Cartesian space.

A condensed version of the full derivation of the transport equation governing the conservation of momentum, as provided by Schobeiri (2010), follows. The derivation begins with the Cauchy equation of motion, given by Equation A.2, which expresses the differential form of the linear momentum equation as it applies to any fluid. Equation A.2 is derived through application of Newton's 2nd law of motion to an infinitesimal fluid element.

$$\frac{\partial \vec{v}}{\partial t} + \vec{v} \cdot \nabla \vec{v} = \frac{1}{\rho} \nabla \cdot \vec{\Pi} + \vec{g} \tag{A.2}$$

where ρ and $\vec{g}$ are the fluid density and gravitational acceleration vector respectively. The second term on the right-hand side, $\nabla \cdot \vec{\Pi}$, is the divergence of the stress tensor field, which represents the normal and shear stresses, π_{ij}, acting on the surface of the fluid element, shown in Cartesian space in Equation A.3.

$$\pi_{ij} = \begin{pmatrix} \pi_{11} & \pi_{12} & \pi_{13} \\ \pi_{21} & \pi_{22} & \pi_{23} \\ \pi_{31} & \pi_{32} & \pi_{33} \end{pmatrix} \tag{A.3}$$

Surface forces cause deformation of the fluid element; therefore, a functional dependence between the stress tensor and the velocity gradient is apparent, as captured by Equation A.4:

$$\vec{\Pi} = f(\nabla\vec{v}) \tag{A.4}$$

The tensor product of ∇ and $\vec{v}$ can be separated into the deformation tensor $\vec{D}$ and the vorticity tensor $\vec{\Omega}$, as shown in Equation A.5:

$$\nabla\vec{v} = \frac{1}{2}\left(\nabla\vec{v} + \nabla\vec{v}^{T}\right) + \frac{1}{2}\left(\nabla\vec{v} - \nabla\vec{v}^{T}\right) = \vec{D} + \vec{\Omega} \tag{A.5}$$

However, $\vec{\Pi}$ is a frame indifferent property and accordingly its arguments must likewise satisfy this characteristic. This holds true only for the first argument in Equation A.5; therefore, the functional dependence is adapted, as shown in Equation A.6:

$$\vec{\Pi} = f\left(\vec{D}\right) \tag{A.6}$$

Further discussion is limited to isothermal, incompressible Newtonian fluids, in which a linearly proportional relationship exists between $\vec{\Pi}$ and $\vec{D}$, as shown in Equation A.7:

$$\vec{\Pi} = f_1\vec{I} + f_2\vec{D} \tag{A.7}$$

For moving fluids this generalized expression reduces to Equation A.8:

$$\vec{\Pi} = -P\vec{I} + 2\mu\vec{D} \tag{A.8}$$

Substitution of Equation A.8 into Equation A.2 yields the Navier-Stokes equation for incompressible fluids, given by Equation A.9:

$$\frac{\partial\vec{v}}{\partial t} + \vec{v}\cdot\nabla\vec{v} = \frac{1}{\rho}\nabla\cdot\left[-P\vec{I} + 2\mu\vec{D}\right] + \vec{g} \tag{A.9}$$

More conventional representation is uncovered through performing the differentiation of the first term on the right-hand side, arriving at Equation A.10:

$$\frac{\partial\vec{v}}{\partial t} + \vec{v}\cdot\nabla\vec{v} = \frac{1}{\rho}\nabla P + \nu\Delta\vec{v} + \vec{g} \tag{A.10}$$

where Δ is the Laplace operator. Within CFD environments the contributions of body forces and other external momentum sources are included as separate source terms, S_m, shown by Equation A.11:

$$\frac{\partial\vec{v}}{\partial t} + \vec{v}\cdot\nabla\vec{v} = \frac{1}{\rho}\nabla P + \nu\Delta\vec{v} + S_m \tag{A.11}$$

Continuity, together with the Navier-Stokes equation and the omitted energy equation describe Newtonian fluid flow completely. Within the present study, fluid flow is assumed to be incompressible and there is an absence of any heat sources or sinks; therefore, solution of the energy equation is not warranted.

A.2 Turbulence modelling

Turbulent flow features are accounted for through the assumption that any turbulent quantity, ϕ, can be decomposed into a mean (designated by the over bar) and fluctuating component (designated by the apostrophe), as shown in Equation A.12:

$$\phi = \bar{\phi} + \phi' \tag{A.12}$$

Decomposing the flow variables in Equation A.1 and Equation A.10 in an according fashion and applying time-averaging operations results in the modified forms given by Equation A.13 and Equation A.14:

$$\nabla \cdot \vec{v} = \nabla \cdot \bar{v} = 0 \tag{A.13}$$

$$\frac{\partial \bar{v}}{\partial t} + \bar{v} \cdot \nabla \bar{v} = -\frac{1}{\rho}\nabla \bar{P} + \nu \Delta \bar{v} + \mathrm{g} - \nabla \cdot (\overline{v'v'}) \tag{A.14}$$

Equation A.13 is the continuity equation for the mean flow, since $\overline{v'}$ is identically zero. Equation A.14 is known as the Reynolds-averaged Navier Stokes equation (RANS) and the additional uncovered term, $\overline{v'v'}$, is aptly termed the Reynolds stress tensor. In this study, the Reynolds stresses are resolved through the Boussinesq approach, described by Equation A.15, which is based on the same prior analogy that fluid element stresses are proportional to the mean velocity gradient.

$$\rho\overline{v'v'} = \mu_t \bar{D} - \frac{2}{3}\rho k \delta_{ij} \tag{A.15}$$

where δ_{ij} is the Kronecker delta, μ_t is the turbulence or eddy viscosity and k is the kinetic energy equation as defined in Equation A.16:

$$k = \frac{1}{2}\left(\overline{{v'_1}^2 + {v'_2}^2 + {v'_3}^2}\right) \tag{A.16}$$

Solving the Reynolds stress tensor now focuses on determining an approximation for μ_t. In this study the realizable k-ε turbulence model (Shih *et al.,* 1995) is used for this purpose. The realizable k-ε turbulence model is a two-equation model that solves μ_t through determination of the kinetic energy and kinetic energy dissipation rate in accordance with Equation A.17.

$$\mu_t = \rho C_\mu \frac{k^2}{\varepsilon} \tag{A.17}$$

where C_μ is a variable discussed further on (Equation A.22). The realizable k-ε model was chosen based on the recommendations made by van der Spuy (2011) for use with the fan models this study employs (as discussed in Section 3). Furthermore, the realizable k-ε model offers an improvement over the standard k-ε model through its ability to handle large flow field strains and homogeneous rotating shear flows, and enhanced numerical stability (Shih *et al.,* 1995). The prescribed transport equations for the realizable k-ε model are presented in Equation A.18 and Equation A.19.

$$\frac{\partial k}{\partial t} + (\bar{v} \cdot \nabla)k = \frac{\partial}{\partial x_j}\left(\left(\nu + \frac{\nu_t}{\sigma_k}\right)\frac{\partial k}{\partial x_j}\right) - G_k - \varepsilon + S_k \tag{A.18}$$

$$\frac{\partial \varepsilon}{\partial t} + (\bar{v} \cdot \nabla)\varepsilon = \frac{\partial}{\partial x_j}\left(\left(\nu + \frac{\nu_t}{\sigma_\varepsilon}\right)\frac{\partial k}{\partial x_j}\right) - C_1 S\varepsilon - C_2 \frac{\varepsilon^2}{k+\sqrt{\nu\varepsilon}} + S_\varepsilon \tag{A.19}$$

where

$$G_k = \overline{v_i' v_j'}\frac{\partial \bar{v_i'}}{\partial x_j} \tag{A.20}$$

$$C_1 = \max\left[0.43, \frac{\eta}{\eta+5}\right],\ \eta = S\frac{k}{\varepsilon},\ S = \sqrt{2\bar{D}\bar{D}} \tag{A.21}$$

The G_k term in Equation A.20 captures the generation of turbulent kinetic energy due to the mean velocity gradients. In Equation A.21, S is the modulus of the mean deformation tensor (Shih *et al.,* 1995), S_k and S_ε are source terms offering provision for the accountability of additional influences, and σ_k and σ_ε are the turbulent Prandlt numbers. The values for the turbulent Prandlt numbers and the remaining coefficients not explicitly mentioned are given in Table 6.

Table 6: Realizable k-ε turbulence model coefficients

$C_2 = 1.90$	$\sigma_k = 1.00$	$\sigma_\varepsilon = 1.20$

A prominent distinction of the realizable k-ε model over the standard k-ε model is the treatment of the C_μ coefficient as a variable in Equation A.17; $C_\mu$is calculated according to Equation A.22:

$$C_\mu = \left(A_0 + A_s\frac{kU^*}{\varepsilon}\right)^{-1} \tag{A.22}$$

where A_0 = 4.0. Further details of the variable coefficient A_s and the function $U^*$are described in (Shih *et al.,* 1995).

In this study, the realizable k-ε model is used in conjunction with the enhanced wall function treatment functionality (Fluent, 2009) available in ANSYS Fluent. The

enhanced wall treatment is a two-layer model approach offering improved resolution of the near-wall regions and greater y^+ insensitivity over standard wall treatments (Fluent, 2009). With this approach the calculation domain is subdivided into a fully turbulent region and viscosity-affected region, differentiated based on the turbulent wall-based Reynolds number, Re_y^+, described by Equation A.23:

$$Re_y^+ = \frac{\rho y^+ \sqrt{k}}{\mu} \tag{A.23}$$

Where $Re_y^+ < 200$, enhanced wall functions are used; whereas, where $Re_y^+ > 200$, a modified low Reynolds number approach is used (Fluent, 2009). The use of the enhanced wall treatment is recommended for all two-equation wall-function turbulence models (Augustyn, 2013).

A.3 Discretisation

The finite volume formulation of the CFD code used to perform the flow field calculations divides the computational flow domain in discrete control volumes. Solution of the partial differential equations (discussed in A.2) over the finite volumes requires the equations to be discretised into algebraic form (van der Spuy, 2011). The discretisation process aims to express the value of a scalar quantity, ϕ, at a control volume node, p, as a linear combination of the value of ϕ at neighbouring nodes, n, according to Equation A.24:

$$a_p \phi_p = \sum a_n \phi_n + S_\phi \tag{A.24}$$

The influence coefficients, a, are dependent upon the relevant governing conservation principle, the geometrical characteristics of the control volumes (cells) and the chosen interpolation scheme used to equate the scalars and scalar gradient values at the cell interfaces. The nature of the finite volume formulation requires knowledge of the flow variables at cell boundaries. Resultantly a host of different interpolation schemes are available to calculate these inter-cell face variable values from the known cell node values. This study utilizes a combination of second-order and first-order upwind differencing interpolation schemes. First-order upwind schemes determine cell face values based on only a single cell node value upstream of the relevant face, while the second-order scheme bases face values on a weighted average of two upstream cell node values. The first-order schemes are more computational stable, while second-order schemes offer greater accuracy, in terms of Taylor series truncation (Fluent, 2009). Details of the employed discretisation schemes used in this study are provided in Section 4.

Appendix B Sample Calculations

B.1 Fan curve characterization

The ability of the numerical fan models (Section 3) to correctly determine fan performance was evaluated through the described single fan installation simulations in Section 4. These simulations mimicked the equivalent experimental process, in which a single tunnel from the multiple fan test facility (Section 5) is used in isolation. Fan performance is determined through measurement of the total-to-static pressure rise across the fan rotation plane, described by Equation B.1:

$$\Delta P_{ts} = P_{s2} - P_{t1} \tag{B.1}$$

where subscripts 1 and 2 designate the fan entry and exit planes respectively.

In the experimental case, pressure rise is determined by measurement of the static gauge pressure aft of the hex-core mesh (Figure 9, Section 2). Pressure measurements are then processed using the equations prescribed by the ISO 5801 standard (ISO, 2007) to determine the static pressure at the fan exit plane and to detail the fan pressure rise in accordance with Equation B.1. To ensure consistency and to enable direct comparison between the numerical and experimental results, the numerical measurements were recorded and determined in the same manner to the experimental case. The mathematical procedure used to consistently determine the fan static pressure rise is outlined below.

The sample calculation is demonstrated using the results from the PJM simulation at a volumetric flow rate of 1.2 m^3/s, with ambient air at a density, ρ, of 1.2 kg/m^3 and dynamic viscosity, μ, of 1.8 x 10^{-5} kg/ms.

The utilized alternative correlation to Equation B.1, which explicitly accommodates the details of the experimental facility (and, hence, the numerical model) and the static pressure measurement location is given by Equation B.2.

$$\Delta P_{ts} = P_s + P_{pipe} + P_{hex} + P_{d3} - P_{d2} - P_{t1} \tag{B.2}$$

where P_s is the static pressure measured at the location plane, aft of the hex-core mesh. The second last term of Equation B.2, P_{d2}, is the dynamic pressure at the fan exit plane, and it is described by Equation B.3. Determination of P_{d2} requires knowledge of the velocity through the fan duct, v_2, which is calculated based on Equation B.4 where A_2 is the area:

$$P_{d2} = \frac{1}{2}\rho_{amb}v_2^2 = \frac{1}{2}(1.2)(3.8496)^2 = 8.8914\ Pa \tag{B.3}$$

where

$$v_2 = \dot{V}/A_2 = 1.2/(\pi(0.315)^2) = 3.8496\ m/s \quad \text{(B.4)}$$

Likewise, P_{d3}, is the dynamic pressure within the plenum chamber and it is calculated using the applicable velocity, v_3, through the plenum chamber, shown by Equations B.5 and B.6:

$$v_3 = \dot{V}/A_3 = 1.2/(0.8^2) = 1.8750\ m/s \quad \text{(B.5)}$$

$$P_{d2} = \frac{1}{2}\rho_{amb}v_2^2 = \frac{1}{2}(1.2)(1.8750)^2 = 2.1094\ Pa \quad \text{(B.6)}$$

Pressure loss over the hex-core mesh is accounted for by the P_{hex} term. Van der Spuy (2011) determined the polynomial describing the resistance characteristics of the hex-core mesh as a function of velocity, which is given by Equation B.7:

$$P_{hex} = 0.0981v_3^2 + 1.4782v_3 = 3.1165\ Pa \quad \text{(B.7)}$$

The ISO 5801 standard correlation for pressure loss between the measurement plane and fan exit plane, P_{pipe}, is given by Equation B.8. Solution of Equation B.8 requires calculation of the respective Reynold's numbers at the different tunnel sections, described by Equations B.9 and B.10; where d_f is the fan diameter and D_3 is the hydraulic diameter of the plenum chamber.

$$P_{pipe} = (0.1 + 0.005 + 0.42Re_2^{-0.3})P_{d2} + (0.005 + 0.42Re_3^{-0.3})P_{d3} \quad \text{(B.8)}$$

$$P_{pipe} = 1.0744\ \text{N/m}^2$$

where

$$Re_2 = \frac{\rho v_2 d_f}{\mu} = \frac{(1.2)(3.8496)(0.63)}{1.8\cdot10^{-5}} = 1.6168 \cdot 10^5 \quad \text{(B.9)}$$

$$Re_3 = \frac{\rho v_3 D_3}{\mu} = \frac{(1.2)(1.8750)(0.8)}{1.8\cdot10^{-5}} = 1 \cdot 10^5 \quad \text{(B.10)}$$

Provision for the sudden expansion of the plenum chamber is accounted for by the 0.1 loss factor in Equation B.8.

Lastly, P_{t1} is recorded at a plane $1.25d_f$ upstream of the fan rotation plane. The values for P_s and P_{t1} are extracted from the numerical domain and substituted, along with the remaining terms, into Equation B.2 to equate the final static pressure rise, as shown in B.11:

$$\Delta P_{ts} = 21.71 + 1.07 + 3.12 + 2.11 - 8.89 - (-56.49) \quad \text{(B.11)}$$

$$\Delta P_{ts} = 75.61\ \text{N/m}^2$$

B.2 Pressure jump method polynomial derivation

The polynomial expression used in the formulation of the pressure jump method (PJM) used in this study was taken from Fourie (2014). The PJM is used in this study for the representation of fans 2 and 3 in the experimental facility simulations (Section 5). The PJM is utilized by assigning a static-to-static pressure rise function (polynomial) to Fluent's fan boundary condition (details of which are discussed in Section 3). Herewith is the derivation undertaken to arrive at the static-to-static pressure rise polynomial used to effect the operation of the 630 mm L2-fan using the PJM.

Firstly, a third order polynomial is fitted to the L2-fan's characteristics curve that have been determined on a ISO 5801 type B test facility, as illustrated in Figure 60. The resulting polynomial for the fitted curve is given by Equation B.12.

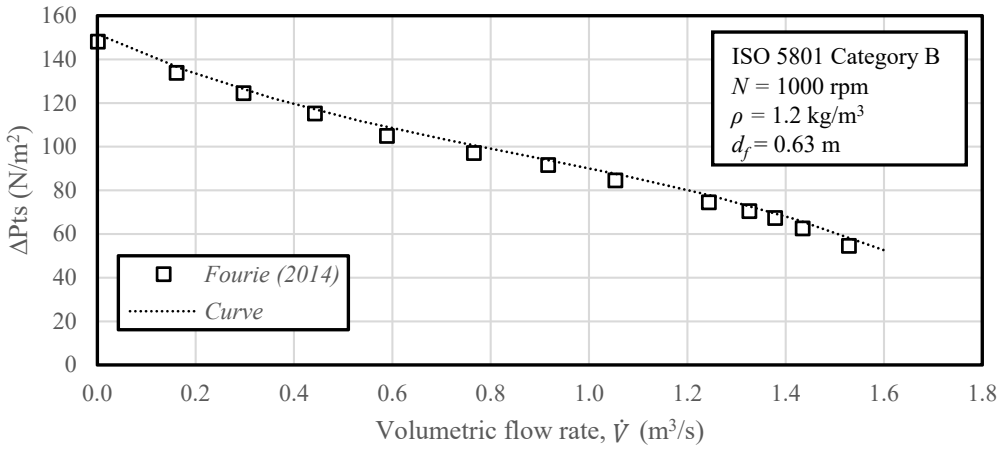

Figure 60: L2-fan static pressure rise curve fit (Fourie, 2014)

$$\Delta P_{ts} = -26.9334\dot{V}^3 + 69.3258\dot{V}^2 - 103.8657\dot{V} + 151.6 \qquad \text{(B.12)}$$

Fluent's fan boundary condition requires specification of the static-to-static pressure rise in terms of normal velocity, v. Equation B.12, therefore, needs to be adapted. This is done through expansion of the volumetric flow rate term, $\dot{V}$, into its products, which resulting in Equation B.13:

$$\dot{V} = Av$$

$$\Delta P_{ts} = -26.9334A^3v^3 + 69.3258A^2v^2 - 103.8657Av + 151.6 \qquad \text{(B.13)}$$

where the fan annulus area, A, is determined using Equation B.14:

$$A = \pi(r_{shroud}^2 - r_{hub}^2) = \pi(0.315^2 - 0.0475^2) = 0.305\ m^2 \quad \text{(B.14)}$$

Multiplying the coefficient products in Equation B.13 produces the total-to-static pressure jump function in terms of normal velocity, as described by Equation B.15:

$$\Delta P_{ts} = -0.762v^3 + 6.4340v^2 - 103.8657Av + 151.6 \quad \text{(B.15)}$$

Conversion of Equation B.15 to a static-to-static pressure rise function requires the dynamic pressure component and the bellmouth inlet losses to be added to the expression, as shown in Equation B.16:

$$\Delta P_{ss} = -0.76v^3 + 6.43v^2 - 31.65v + 151.6 + \frac{1}{2}\rho v^2 + \frac{1}{2}\rho K_{in} v^2 \quad \text{(B.16)}$$

where the loss coefficient, K_{in}, is obtained using Equation B.17 (van der Spuy, 2011):

$$K_{in} = 0.06\left(\frac{\pi(r_{shroud}^2 - r_{hub}^2)}{\pi r_{shroud}^2}\right) = 0.06\left(\frac{0.3047}{0.3117}\right) = 0.0587 \quad \text{(B.17)}$$

Taking air at a density (ρ) of 1.2 kg/m^3 and substituting Equation B.17 into Equation B.16 then delivers the needed static-to-static pressure polynomial function for the 630 mm L2-fan. The resulting expression, as determined by Fourie (2014), is shown in Equation B.18:

$$\Delta P_{ss} = -0.762v^3 + 7.072v^2 - 31.649v + 151.6 \quad \text{(B.18)}$$

B.3 Porous-jump parameters

The procedure used to convert the windscreen materials' resistance characteristics into the needed porous-media model coefficients is shown here. A polynomial expression in the form of Equation B.19 is first fitted to the pressure loss versus velocity characteristic of the relevant material.

$$\Delta P = av^2 + bv \quad \text{(B.19)}$$

The resulting coefficients are then equated to those of Equation B.20 which describes the pressure loss as it is interpreted by Fluent.

$$\Delta P = -\left(\frac{\mu}{\alpha_{sm}} v + C_2 \frac{1}{2}\rho v^2\right)\Delta x \quad \text{(B.20)}$$

where the negative sign indicates that the porous-jump is a momentum sink.

The inertial resistance term (C_2) is then obtained as shown in Equation B.21.

$$C_2 = \frac{a}{\left(\frac{1}{2}\rho \Delta x\right)} \quad \text{(B.21)}$$

and the face permeability term, α_{sm}, through Equation B.22.

$$\alpha_{sm} = \frac{\mu \Delta x}{b} \tag{B.22}$$

Appendix C L2-fan lift and drag characteristics

The ADM and EADM calculate the implemented source terms using blade element theory. This requires knowledge of the relevant fan blade's airfoil lift and drag characteristics.

By virtue of flow distortions and reserve flow near the hub, axial flow fans can be exposed to flow angles ranging from -90° to 90° (Bredell, 2005). Therefore, in order to obtain lift and drag characteristic information across the full range of interest, two-dimensional isolated airfoil CFD simulations are performed.

At a reference density of 1.2 kg/m^3 and dynamic viscosity of 1.8×10^{-5} kg/ms, the 630 mm diameter L2-fan, with a constant chord length of 76 mm, a hub-to-tip ratio of 0.15 and rotating at 1000 rpm will experience Reynolds numbers ranging from 1.6×10^3 to 2.5×10^5 along its blade span. However, the lift and drag characteristics used in this study's ADM and EADM are based on a singular Reynolds number at an arithmetic mean radius, as similarly done by Bredell (2005). For the present case, the lift and drag coefficients were found to be relatively insensitive to Reynolds number over the applicable span-wise range, so use of only the mean characterization was deemed satisfactory.

At the arithmetic mean radius, the Reynolds number is approximately 0.96×10^5. This Reynolds number is slightly lower than the critical value of 1×10^5 defined by Çengel and Cimbala (2014); therefore, the use of transitional models in the analysis is warranted. Van der Spuy (2011), however, argues that while ideally the transitional turbulence model should be employed, considering that one of effects of blade rotation is to delay separation of the boundary-layer, the airfoil characteristics are more appropriately determined using full turbulence models. Therefore, (consistent with van der Spuy (2011)) the Spalart-Allmaras turbulence model was used for all airfoil simulations. The Spalart Allmaras turbulence model involves solution of one transport eqution for kinematic eddy viscosity (ν_t), and is especially sutied to extenal aerodynamic applications with adverse pressure gradients (Spalart and Allmaras, 1994).

C.1 Geometry and meshing

The analysis adopted an approached similar to that used by Van der Spuy (2011). The airfoil profile was located in the center of a circular domain with a radius of 20 chord lengths; van der Spuy (2011) verified that a domain size beyond 20 chord lengths had no discernable effect on the results.

Immediately surrounding the airfoil was an elliptical domain constructed using triangular elements, shown in Figure 61. Van der Spuy (2011) noted that when the analysis involves a variation of angle of attack from -10° to 10° (in the 'normal'

range) hexahedral elements are usually preferred; however, for an extended angular range, triangular elements may be more suited.

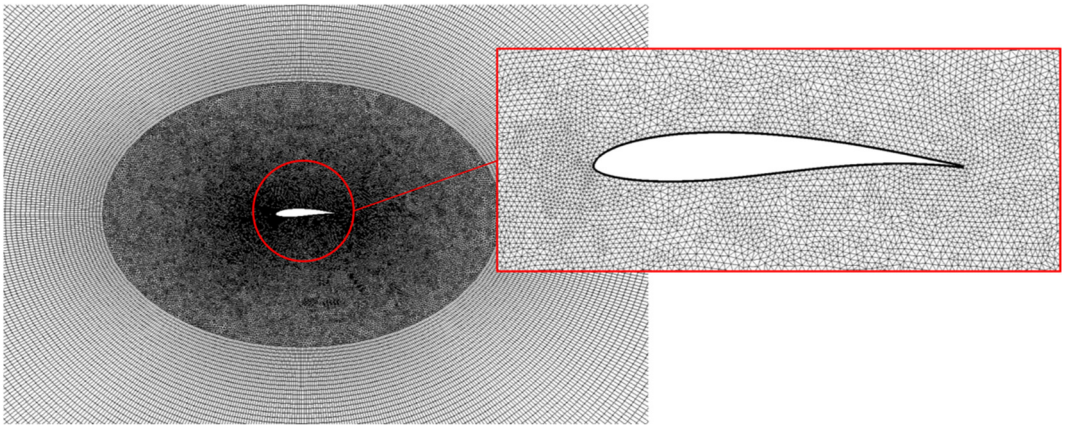

Figure 61: Numerical mesh of airfoil profile simulations

For the correct implementation of the Spalart-Allmaras turbulence model, the boundary layer at the airfoil surface must have a y^+ value of approximately 1. This was achieved using an inflation sizing option on the profile. Based on the recommendations by LEAP CFD Team (2012), in order to sufficiently resolve the boundary layer around the airfoil the inflation option was set to include 10 layers that expanded from the defined first layer at a growth rate of 20%.

C.2 Simulation

It was found that the Coupled pressure-velocity coupling algorithm (with the pseudo-transient formulation enabled) together with second-order spatial discretization schemes resulted in the fastest and most stable convergence. This configuration was, therefore, chosen for the analysis. Furthermore, the default least-squares cell-based gradient evaluation option and the default relaxation factors as prescribed by Fluent were used.

The outer boundary of the circular domain was given a prescribed absolute velocity magnitude (corresponding to the Reynolds number of interest) and direction depending on the angle of attack. The turbulence parameters were set to be consistent with those used in the single fan installation simulations (described in Section 4).

The lift and drag forces at various angles of attack between -90° and 90° were extracted and the subsequent lift and drag coefficients determined. The results of the simulations are shown in Figure 62.

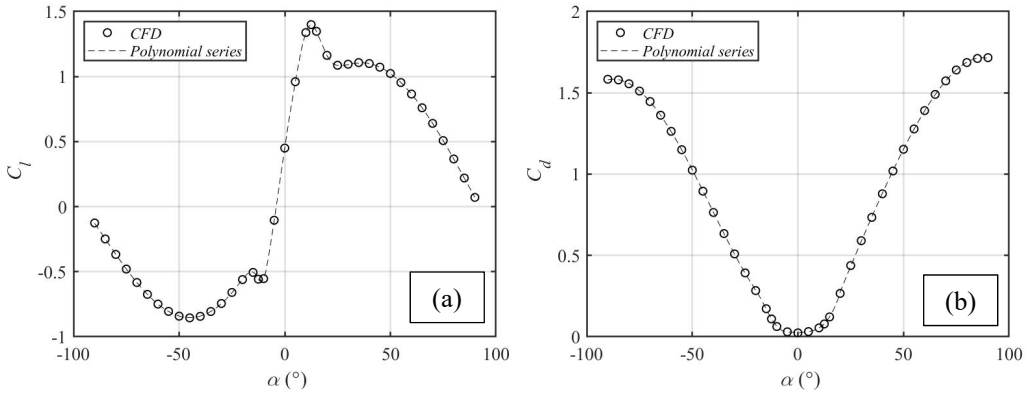

Figure 62: Determined lift and drag characteristics of L2-fan airfoil: (a) lift coefficient (b) drag coefficient

Mesh dependency was verified through the creation of a coarser (78 290 elements) and finer (217 997 elements) mesh, the results from which are presented in Figure 63. No significant change to the results was observed and the original mesh of 132 143 elements was deemed satisfactory.

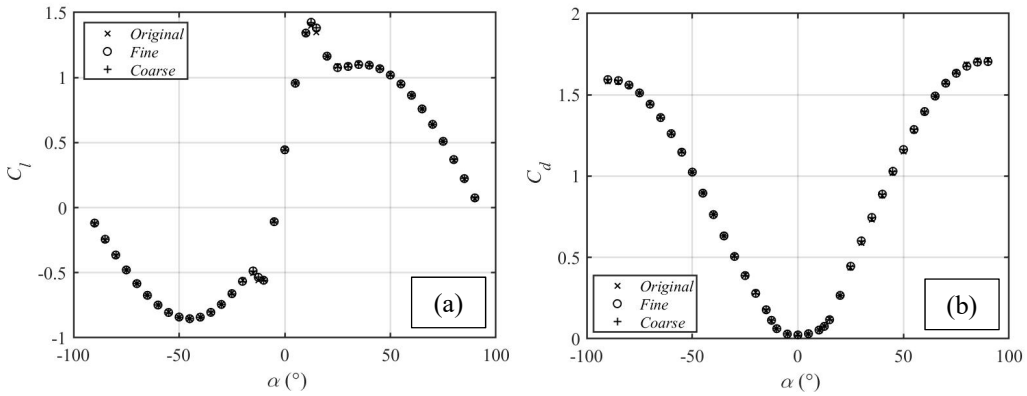

Figure 63: Mesh refinement assessment for airfoil simulations: (a) lift coefficient (b) drag coefficient

The simulation results within the 'normal' angular range were validated against results determined using XFOIL. XFOIL employs a panel method in conjunction with an integral boundary layer formulation for the analysis of subcritical airfoils, and is particularly complementary to low Reynolds number analyses (Drela, 1989). XFOIL, however, cannot handle separated flow regimes and prediction of the airfoil characteristics falters near the extremities of the 'normal range' (van der Spuy, 2011). The comparison is, therefore, limited to the range of $-10° \leq \alpha \leq 13°$ and shown in Figure 64.

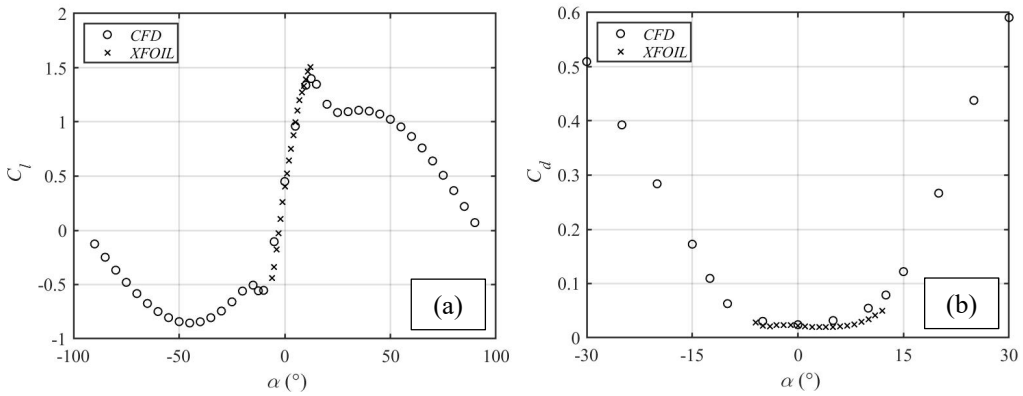

Figure 64: Comparison of CFD derived profile characteristics to XFOIL data: (a) lift coefficient (b) drag coefficient

The CFD results were considered to agree satisfactorily to the comparative data, thus endorsing its validity. Furthermore, the results within the extended angular range are similar to those of a flat plate, which is consistent with expected behavior (Thiart and von Backström, 1993). Slight inaccuracies in the determined CFD relations did not warrant concern; as within the context of the inherit simplifications of the ADM and EADM formulations, greater accuracy of the lift and drag coefficients would not necessarily translate to notably improved fan performance prediction. Polynomial expressions as used for the ADM (and EADM at low RR values) were, therefore, fitted to the CFD relationships depicted in Figure 64 and fed into the respective models coding.

Appendix D Additional numerical simulation considerations

D.1 Windscreen model

Verification of the correct windscreen material pressure drop characterization and the correct implementation of the porous media model into the solver environment needed to be ascertained. Additionally, the influence of computational grid arrangements on the prediction of the pressure drop was not known a priori and any potential grid density sensitivities needed to be identified. To this end, simple CFD simulations using a straight duct geometry, as shown in Figure 65, were conducted.

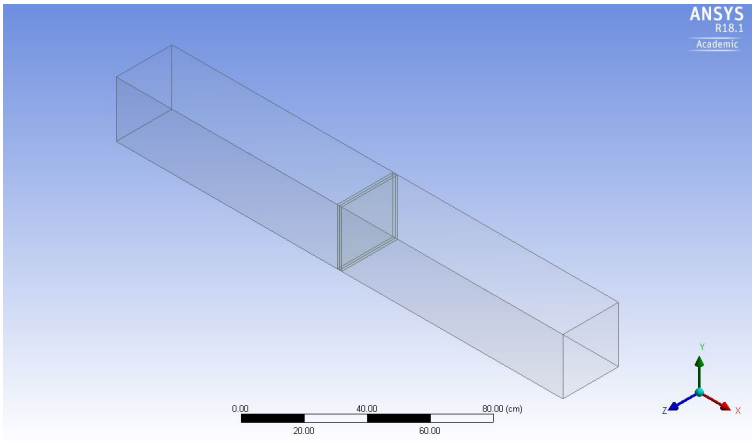

Figure 65: Windscreen model simulation geometry

The replicated windscreen material used in this analysis was that of a 40% solidity ($\epsilon = 0.4$) type; solidity is defined in accordance with Equation 4.3 (Section 4). The porous-jump boundary condition (porous media model applied to a surface boundary), which implicitly implements the pressure drop characteristics of the windscreen material into the numerical simulations, was applied to an interior surface found midway along the duct geometry shown in Figure 65.

The sides of the domain were modelled as symmetry planes and slip walls. The inlet was prescribed a velocity magnitude and the outlet boundary was set as a pressure-outlet of 0 N/m^2 gauge pressure. The employed turbulence model was fixed by that prescribed for the full experimental facility simulations (discussed in Section 5). Therefore, compatibility of the windscreen model with the experimental facility simulations' setup specification could also be partially verified through these straight duct geometry simulations. The realizable k-ε turbulence model was

accordingly used in all the windscreen model simulations. Likewise, second-order upwind differencing interpolation schemes, the least square cell-based gradient calculation scheme and the SIMPLE pressure-velocity coupling algorithm were used.

Unstructured grid arrangements (as found in the resulting full facility simulations) were used. The dependency of the pressure drop prediction on grid resolution was evaluated. The ducted geometry was specified to have tetrahedral elements of 0.02 m size, while refinement was restricted to a central 2 cm, symmetric zone surrounding the porous-jump boundary face. Refinement was done by modifying the local body sizing specification on the central zone. The results from these investigations are shown in Figure 66.

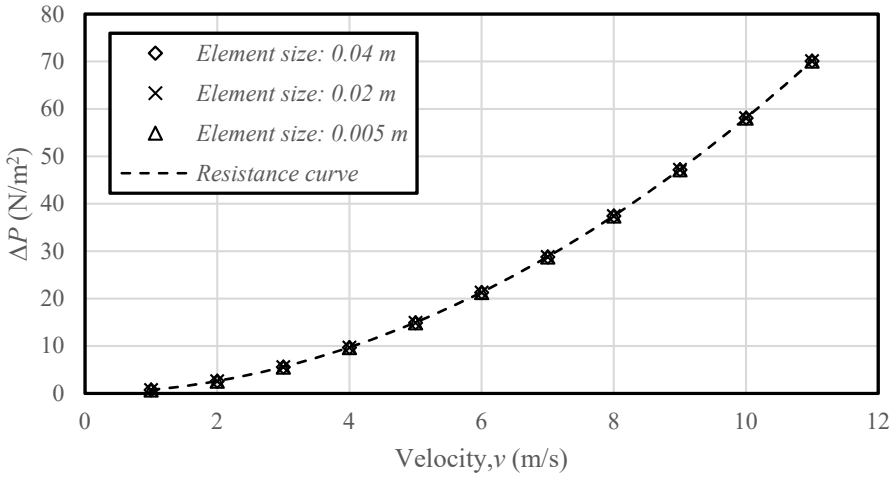

Figure 66: Effect of mesh resolution on porous-jump boundary condition functionality ($\epsilon = 0.4$)

Resultantly, it is apparent that the procedure undertaken to numerically characterize the pressure drop characteristics of the screen material, outlined in Appendix B, was correctly executed. Furthermore, the porous-jump boundary condition demonstrates an insensitivity to unstructured grid density. It was, therefore, established that the porous-jump boundary condition could be confidently applied in the full facility simulations (Section 5) with little regard for the grid structure about it.

D.2 Single fan installation model mesh refinement assessment

Mesh independency for the single fan installation model simulations (Section 4) was confirmed using the PJM on three different meshes of various refinement. The

ADM/EADM structured disks were constructed based on the specifications prescribed by van der Spuy (2011); therefore, further mesh refinement analysis of the disks was deemed unnecessary. Resultantly, the refinement assessment of the mesh was limited to the tetrahedral elements found up- and downstream of the structured fan model disks. The size of the tetrahedral elements in the mesh were both coarsened and refined by a factor 1.3, such that the grid convergence index as detailed by Roache (1994) could be potentially determined. This resulted in a coarse mesh of 2.4 million elements and a fine mesh of 6.2 million elements. Fan static pressure rise was numerically measured and calculated in a consistent manner as done in the experiments, details of which are provided in Appendix B. The results of the investigation are shown in Figure 67.

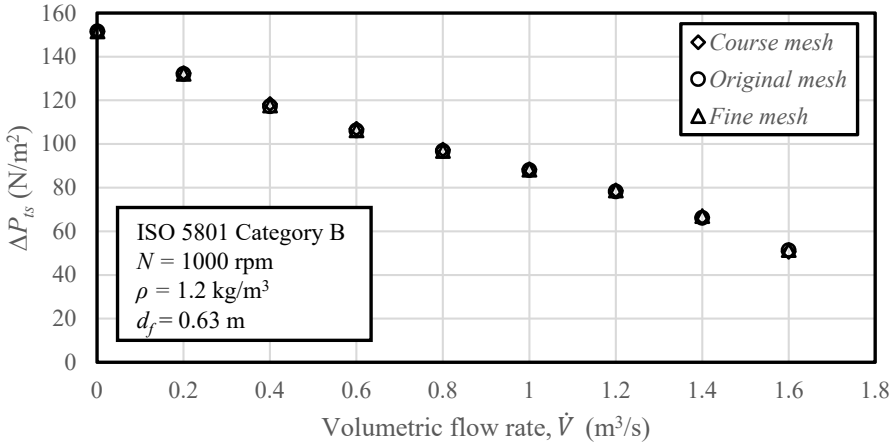

Figure 67: Mesh refinement assessment for single fan installation simulations

An attempt to quantify mesh convergence uncertainty based on the Grid Convergence Index (GCI) method as proposed by Roache (1994) was undertaken. However, due to the use of unstructured grids and non-systematic refinement and coarsening of the mesh elements, no quantifiable grid refinement index could be uncovered. Resultantly, the GCI calculation was omitted. Nonetheless, the results in Figure 67 show that negligible change accompanied a change in mesh resolution; consequently, the mesh as described in Section 4 (original mesh) was deemed satisfactory.

D.3 Blade setting angle

The blade setting angle refers to the angle of the blade's chord relative to the plane of rotation at the root of the blade. Fan characteristic curves are highly dependent on the blade setting angle; therefore, it is a parameter of significant importance in the mathematical specification of the ADM/EADM UDF. The means used by Marincowitz (2018) to set the setting angle in the physical facility was consider

crude and defined differently to that of the ADM/EADM coding. There was, therefore, uncertainty surrounding the correct angle to implement into the ADM subroutine. Marincowitz (2018) reported a blade tip angle of 10.5°, which corresponds to 32.3° at the hub (Augustyn, 2013). Based on the definition of the tip angle reported by Marincowitz (2018), it was suspected that a setting angle greater than 32.3° may be more appropriate. Therefore, simulations at higher setting angles were investigated. These simulations were performed using the single fan installation simulation model described in Section 4 and the ADM for representation of the axial flow fan. The results from this investigation are shown Figure 68.

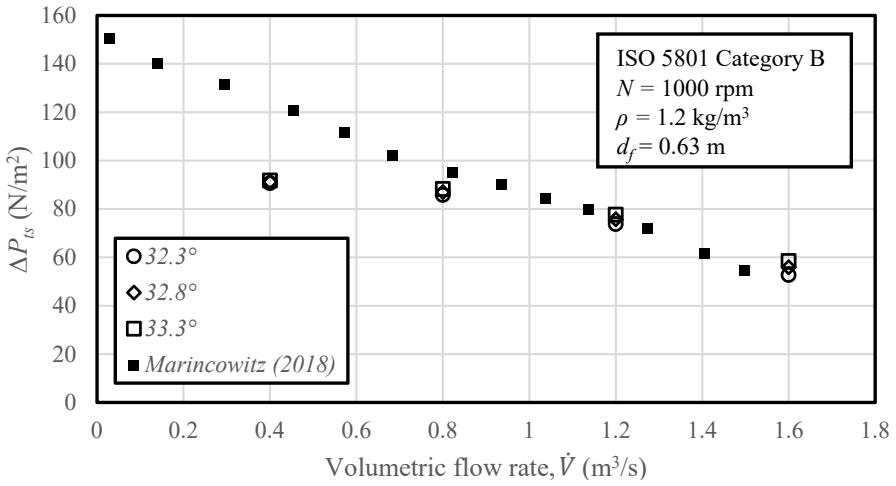

Figure 68: Effect of blade setting angle on ADM fan static pressure rise determination

The results show that the original setting angle of 32.3° best matched the experimental performance. The original setting angle was therefore maintained in all subsequent ADM and EADM simulations.

D.4 Fan tunnel support inclusion effects

While simplification of the fan tunnel details in the single fan installation simulations (Section 4) was not expected to affect fan performance prediction (van der Spuy, 2011), the same could not be implied for the blade loading prediction; as it is known that downstream obstructions effect fan blade vibrational response (Muiyser, 2016). To qualify whether inclusion of the downstream fan shaft support struts (the most prominent features within the immediate downstream vicinity of the fan rotation plane) would have any effect on determined blade loading, the fan tunnel geometry as used in the single fan installation simulations was modified and re-simulated. The modified geometry is shown in Figure 69.

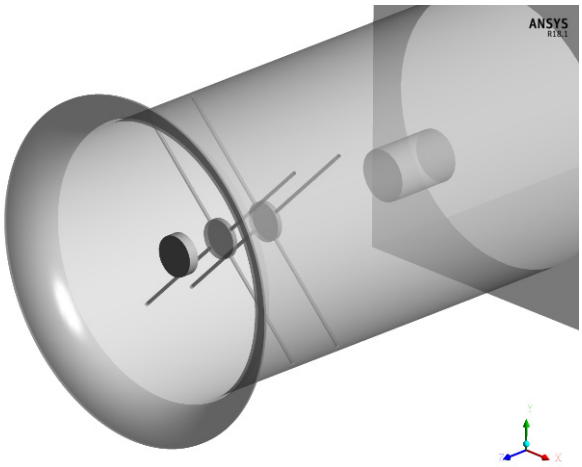

Figure 69: Modified fan tunnel geometry incorporating downstream fan shaft supports

Meshing specifications were consistent with those outlined in Section 4, with the exception that the soft local body sizing function applied to the tunnel domains, downstream of the ADM/EADM disks, was set to a smaller element size. This was done in an effort to counteract the significant element count increase that accompanied inclusion of the support strut walls. The gross element size within the immediate downstream fan vicinity is finer than that in the simplified geometry case, as a very small cell size was necessary to adequately resolve the curved support geometries, as shown in Figure 70. Therefore, the mesh density within the area of interest was not coarsened by the larger element size specification in the tunnel domains.

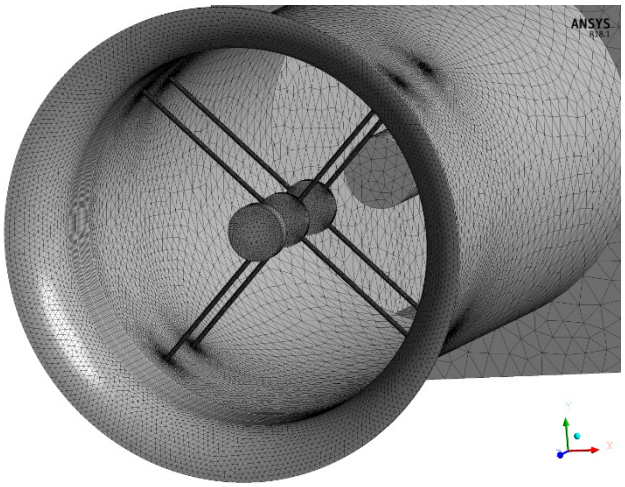

Figure 70: Surface mesh of modified fan tunnel geometry

The potential blade loading influence could be established through examination of the downstream fan static pressure profiles (Muiyser, 2016). If the supports were to have any effect on the resultant blade loading, then notable changes in the determined static pressure profiles at the fan exit plane should exist in line with the positions of the supports.

The simulations in this investigation were performed using the ADM and consistent setup conditions as detailed in Section 4. The determined downstream static pressure profiles for the two extremes of the measured flow rate range ($\dot{V}$ = 0.001 and 1.8 m^3/s) are shown in Figure 71.

(a) (b)

Figure 71: Static pressure profiles determined at fan exit plane showing the absence of downstream obstruction effects: (a) $\dot{V}$ = 0.001 m^3/s (b) $\dot{V}$ = 1.8 m^3/s

Resultantly, uniform downstream pressure profiles were uncovered, suggesting that the inclusion of the fan shaft support struts will not influence the determined blade loading. The simplified fan tunnel geometry was, therefore, utilized for the subsequent simulations.

D.5 EADM limiting radius ratio selection

In Section 3 it was noted that the modified lift and drag coefficients adopted in the EADM are only utilized above a set radius ratio (RR). According to van der Spuy (2011), the limiting RR is set to ensure that predicted fan characteristic behaviour follows measured data from 30% to 100% of the maximum measured flow rate ($\dot{V}$ = 1.8 m^3/s). Selection of the appropriate of RR for use in this study's EADM, applicable for the employed 630 mm L2-fan, was determined through trial of multiple limiting RRs. The results from these trials are shown in Figure 72.

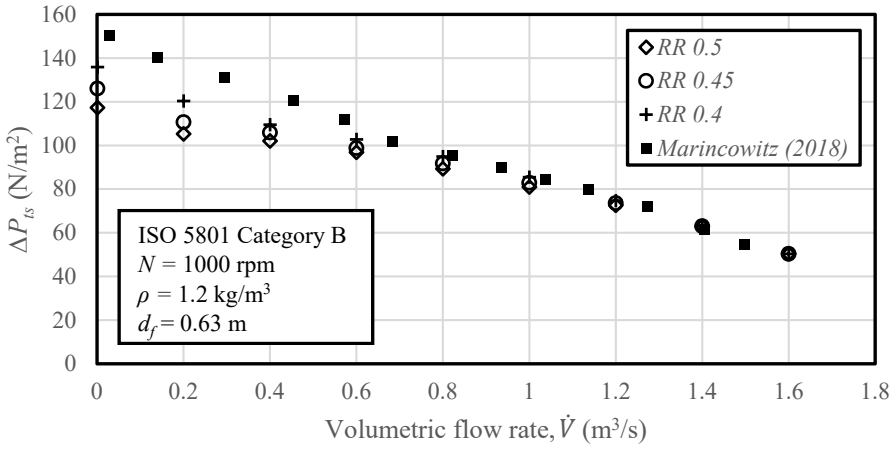

Figure 72: Effect of the EADM's limiting radius ratio on fan static pressure prediction

The chosen limiting RR was capped at a value at 0.4, as a caution against overly suppressing the occurrence of stall along too great a percentage of the blade span. The specification as set by van der Spuy (2011) for simulations using the N-fan was used as a reference case in making this determination. The N-fan has a similar hub-to-tip ratio as the L2-fan used in the current study. Recirculation around the hub region is more pronounced for low hub-to-tip ratio fans; therefore, the EADM as built for the N-fan served as the best comparison in attempting to assess up to what percentage blade span stall effects would most likely feature. Van der Spuy (2011) set the N-fan's limiting RR to 0.52; it was, therefore, considered that the chosen RR for the L2-fan should not be set significantly lower than this value, even though the numerical prediction does not accurately fit the measured results down to 30% of the measured maximum (~0.48 m^3/s). Unfortunately, no detailed velocity profiles could be sourced for the purpose of better setting the limiting RR. This highlights an aspect of the investigation that future studies can look to improve upon.

D.6 Mesh structure conversion effect

In an effort to lessen computation time, the element count of the fan tunnel meshing, described in Section 4, was reduced by converting the tetrahedral cells to polyhedral elements. This was done using the standard routine available in ANSYS Fluent, used by both van der Spuy (2011) and Fourie (2014). The effect of this conversion on fan static pressure rise prediction was checked using the PJM as the reference case. This investigation was performed using the single fan installation model described in Section 4. Consistent setup and simulation procedures, as described for the PJM in Section 4, were adopted for this investigation. The effect of the polyhedral conversion is shown in Figure 73.

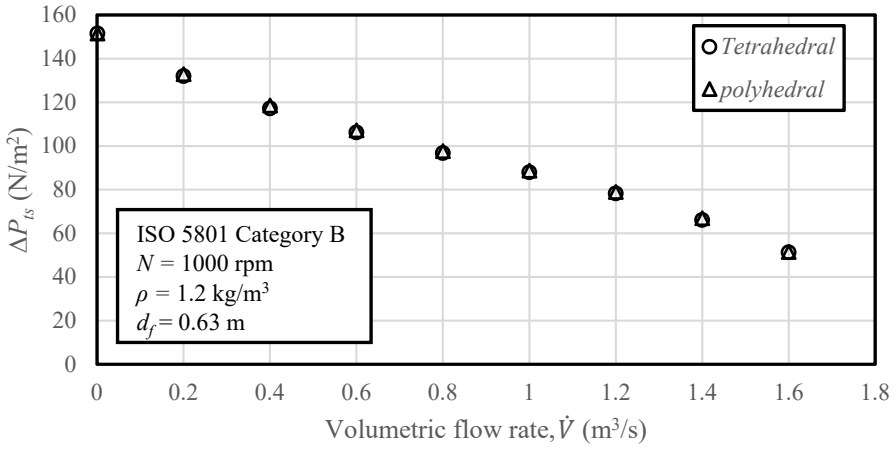

Figure 73: Effect of mesh structure on fan static pressure prediction using the PJM

The tetrahedral and converted polyhedral meshes predict nearly the exact same fan performance behaviour over the entire considered flow rate range. The polyhedral conversion of the mesh, therefore, had negligible effect on the model's fan performance prediction accuracy. The converted mesh was, therefore, use in all subsequent simulations (as described in Sections 5 and 6).

D.7 Domain dependency

In the experimental facility simulations (Section 5), the dimensions of the outlet air space were confirmed through a domain dependency check. The dimensions of the two investigated cases are shown in Table 7.

Table 7: Dimensions of trialled outlet exhaust space domains

Case	x (m)	y (m)	z (m)
1	4.1	1.6	2.5
2	5.35	1.7	2.8

Domain dependency was evaluated based on edge fan performance prediction over the cross-flow range of $0.1 \leq \beta \leq 0.26$ with no included windscreen. The results from the two investigated cases are shown in Figure 74.

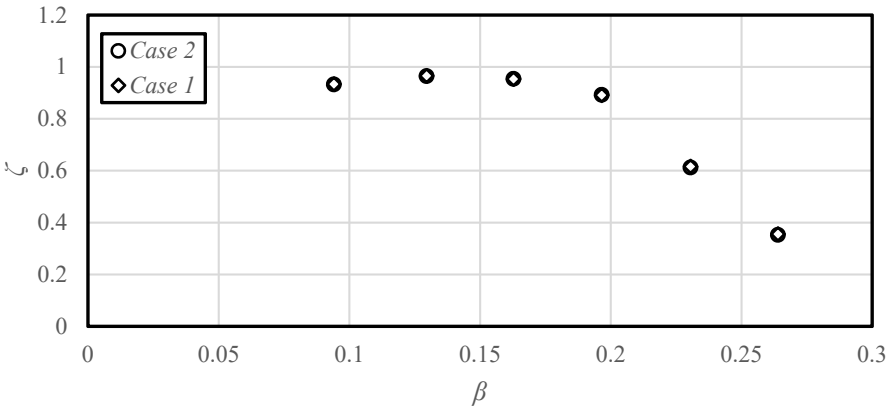

Figure 74: Domain dependency investigation: effect of cross-flow on edge fan performance

Negligible difference between the two cases was observed. However, since the greater outlet volume of Case 2 did not significantly complicate the mesh nor inflate simulation time, it was chosen for further simulations.

D.8 Experimental facility fan model selection

The single fan installation simulations (Section 4) enabled verification of the candidate fan models' construction and accuracy to be resolved; however, these simulations could not indicate which models and in what configuration (i.e. whether to model all fans using the same model or to use a combination of models) the models should be used in the full experimental facility simulations (Section 5). The experimental facility was, therefore, simulated using a host of different fan model configurations. These simulations were used to determine which configuration offered the best experimental representation (in terms of individual fan performance prediction). Details of the trialled fan configurations are presented in Table 8 and the results from this investigation are shown in Figure 75.

Table 8: Trialled axial fan model configurations

Case	Fan 1	Fan 2	Fan 3
1	ADM	ADM	ADM
2	EADM	EADM	EADM
3	PJM	PJM	PJM
4	EADM	PJM	PJM

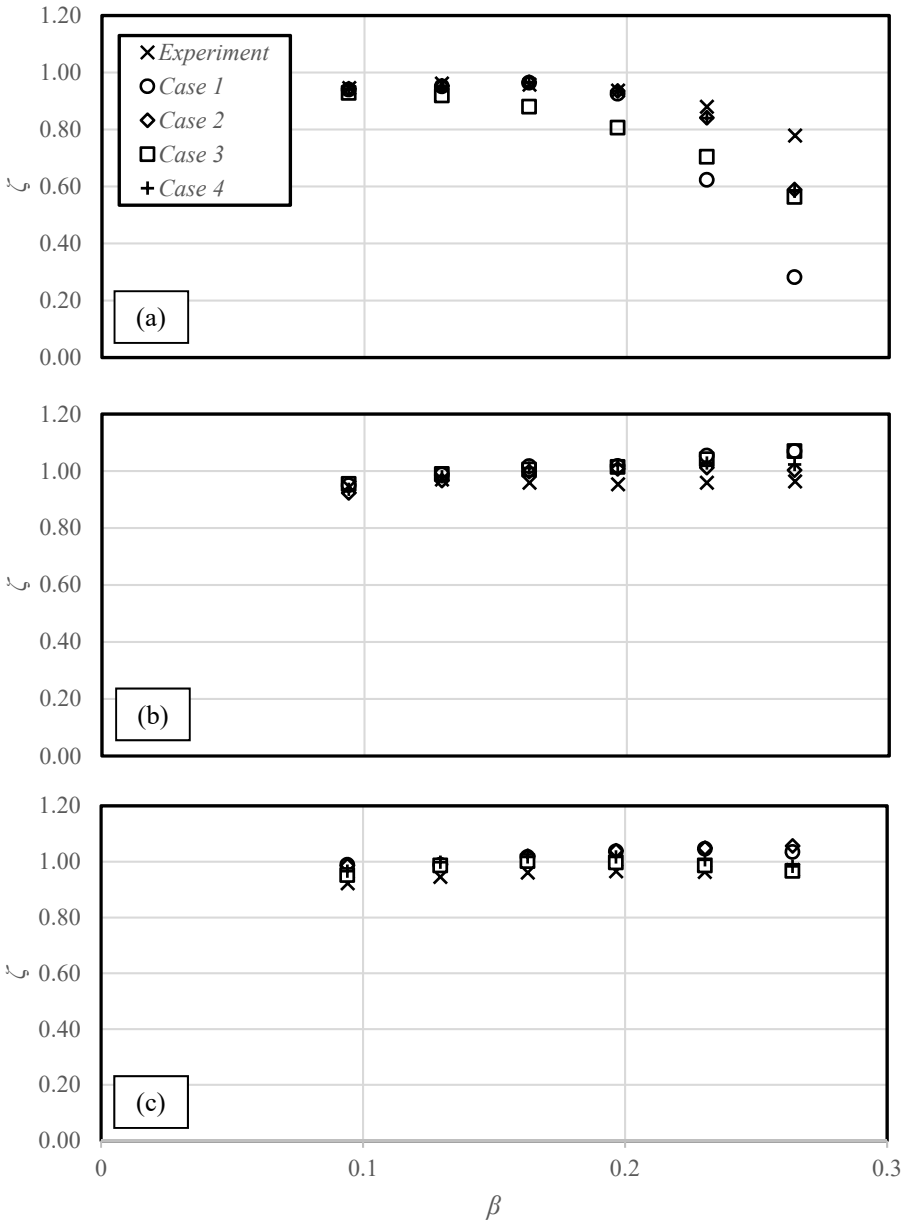

Figure 75: Effect of cross-flow on individual fan performance determined using different axial fan model configurations: (a) fan 1 (b) fan 2 (c) fan 3

Case 3 is not suited for the totality of this study, as use of the PJM on the edge fan does not enable dynamic blade loading to be comprehensively investigated (as addressed in Section 3). Case 3, however, was still trialled so as to provide a comparison to previous studies of a similar nature and for future studies that are concerned only with fan volumetric performance.

Resultantly, case 4 was selected for further use. Case 4 was favoured over case 1 and 2 on the basis that use of the PJM for fans 2 and 3 relaxed the mesh partitioning

requirements, enabling more computational processors to be more readily and effectively used. Van der Spuy (2011) likewise used the PJM to model fans 2 and 3 in his simulations of the same multiple fan tunnel installation (facility employed a different inlet chamber to that of the present study).

Appendix E Additional windscreen fan performance results

For the sake of brevity, the fan performance results and discussions in Section 6.1 are limited to only a few representative cases. The results of the remaining cases (not discussed in Section 6.1) are included here. The individual fan performance results for the $\epsilon = 0.6$ and 0.75 material cases at lengths $L = 0.5$ and 0.75 are given in Figures 76 and 77 respectively. The system volumetric effectiveness results for the omitted cases are given in Figure 78.

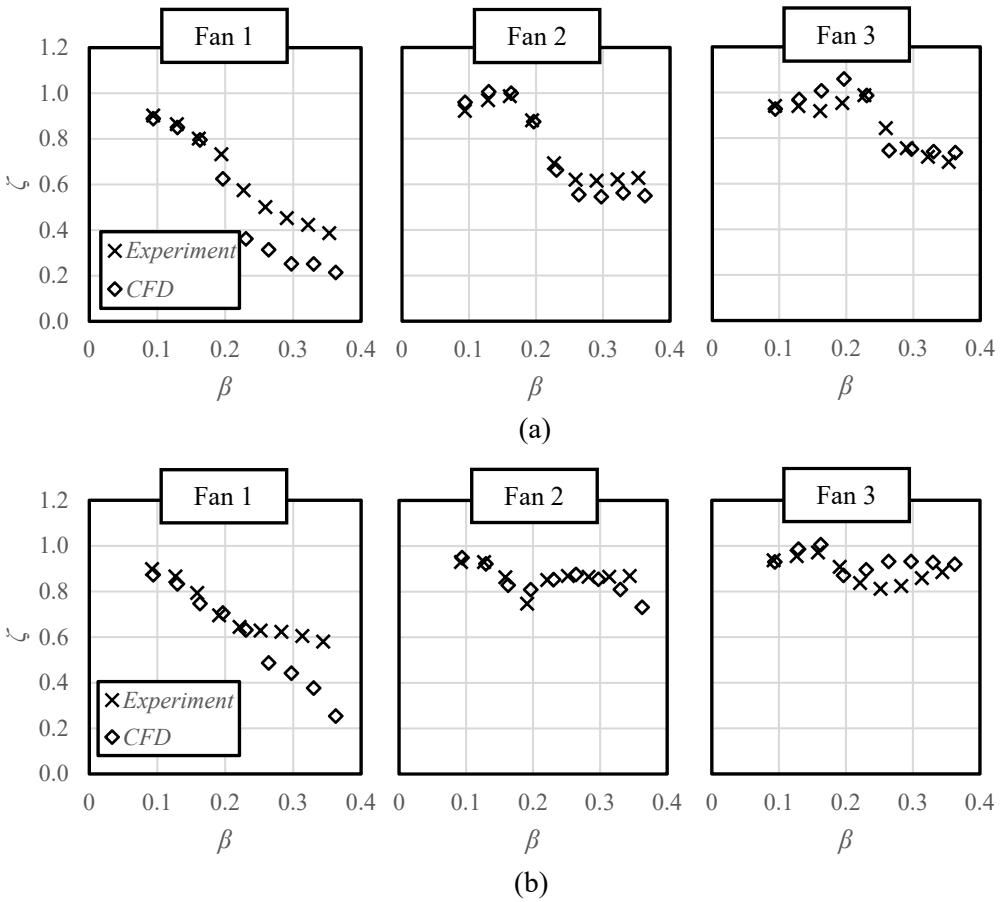

Figure 76: Effect of cross-flow on individual fan performance, $\epsilon = 0.6$: (a) $L = 0.5$ (b) $L = 0.75$

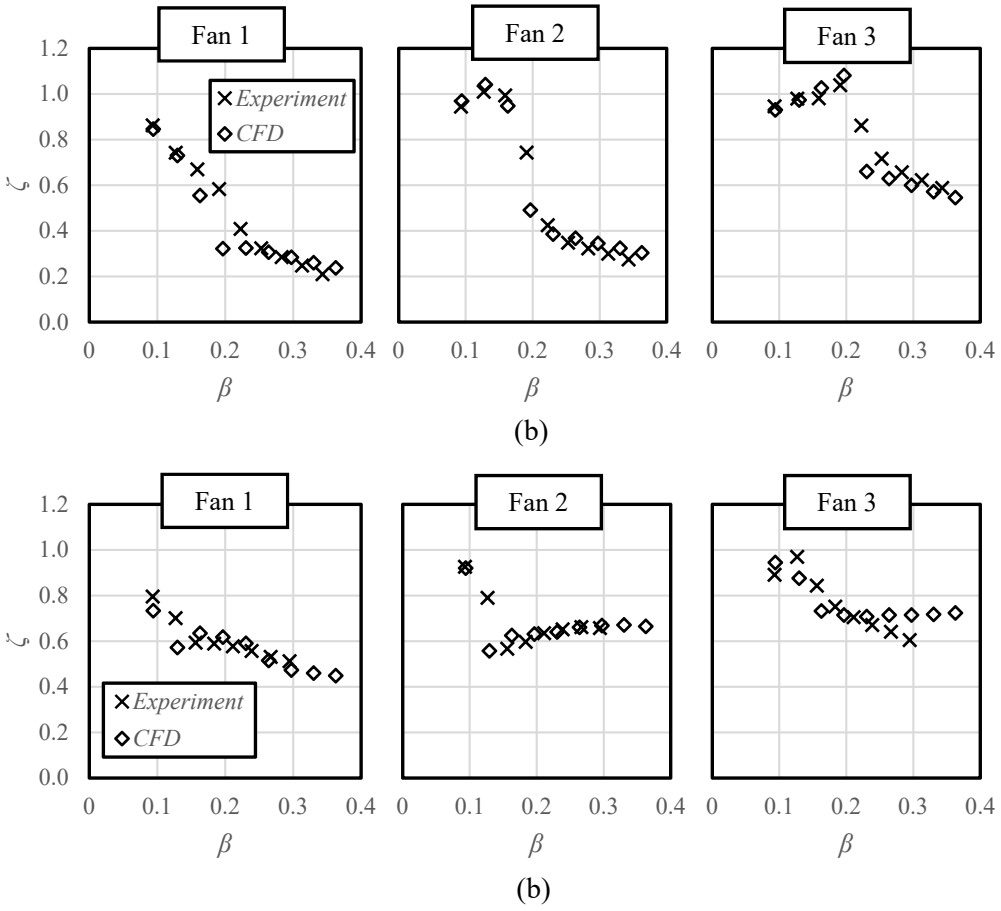

Figure 77: Effect of cross-flow on individual fan performance, $\epsilon = 0.75$: (a) $L = 0.5$ (b) $L = 0.75$

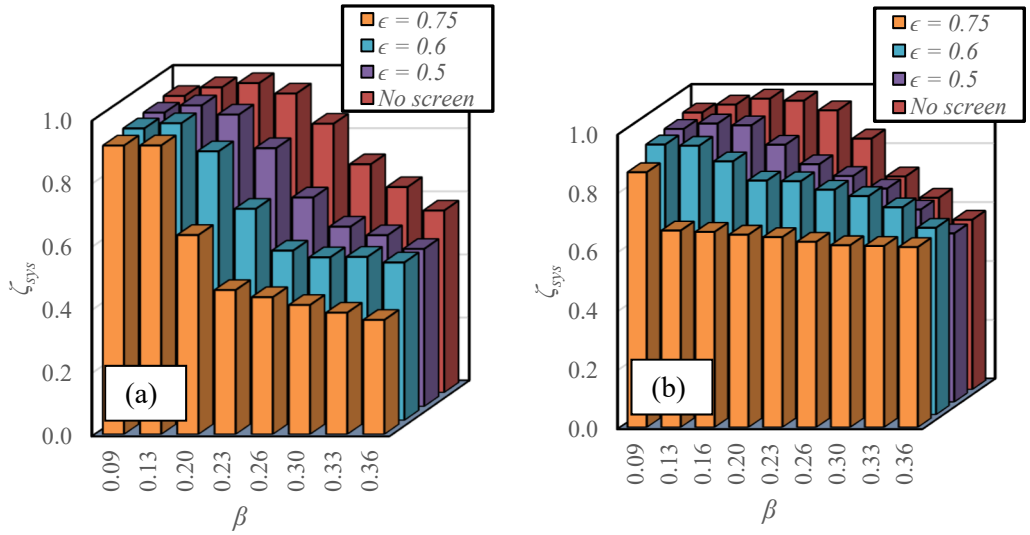

Figure 78: Effect of cross-flow on system volumetric effectiveness (remaining cases, numerical prediction): (a) $L = 0.5$ (b) $L = 0.75$

The same conclusions drawn in Section 6.1 are applicable for the results depicted in Figure 78. The primary effect of including the windscreens remains to degrade fan row performance. A maximum performance deficit of 49% is uncovered at $\beta = 0.23$ with the $\epsilon = 0.75$ material at $L = 0.5$. Slight performance enhancement is, however, obtainable at high cross-flow conditions with a high screen height ($L = 0.75$). For the $\epsilon = 0.6$ material, performance is improved from $\beta \geq 0.3$, with a maximum enhancement of 5.8% at $\beta = 0.36$. For the $\epsilon = 0.75$ material, an improvement of 3.6% occurs at $\beta = 0.36$.

Figure 79 illustrates the accuracy to which this study's experimental facility model was able to predict the system volumetric effectiveness results in Figure 78 (error is defined based on Equation 6.5, Section 6.1.4). Figure 79 shows that the model is able to predict all the $\epsilon = 0.6$ cases within a maximum error of 7.6% up to $\beta = 0.25$ (equivalent full-scale wind speed at platform height of 6 m/s); thereafter, within a maximum error of 16% up to $\beta = 0.35$. Likewise, Figure 79 shows that the model is able to predict the $\epsilon = 0.75$ cases within a maximum error of 15.7% at low flow rates (up to $\beta = 0.225$) but within a maximum error of 6% at higher cross-flow rates.

The atypical error trend for the $\epsilon = 0.75$ material at $L = 0.5$ and 0.75 suggests that the unknown flow mechanisms that the EADM ignores (van der Spuy, 2011) are only present up to intermediate flow cross-flow rates in for the $\epsilon = 0.75$ material cases, whereas with the other material cases it is reversed (mechanisms only features at higher cross-flow rates). Nonetheless, as discussed in Section 6.1, these results demonstrate that the numerical model's accuracy is limited by the simplified fan models, highlighting the need for a novel implicit model for the purposes of forced cross-flow performance assessment; as recommended in Section 8.

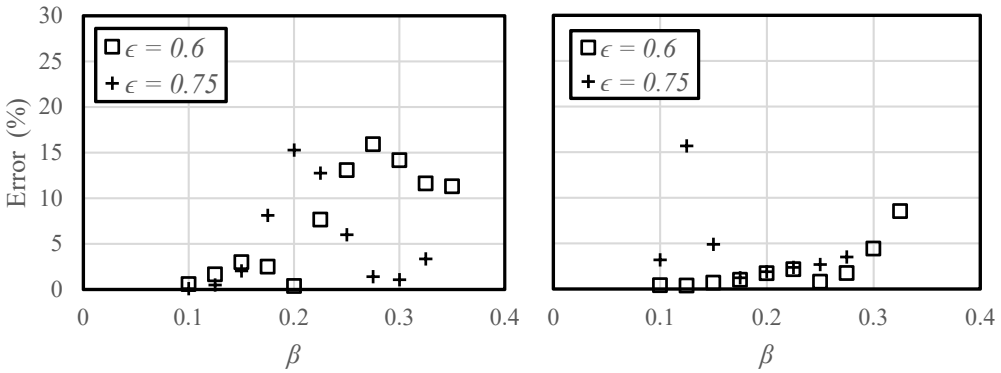

Figure 79: Numerical system volumetric effectiveness prediction error: (a) $L = 0.5$ (b) $L = 0.75$

References

Augustyn, P.H. (2013). *Experimental and Numerical Analysis of Axial Flow Fans.* MscEng Thesis, Department of Mechanical Engineering, University of Stellenbosch.

Ayvazian, J. (2015). Galebreaker Windscreen Installation on Unit 8 ACC Mystic Station Exelon Generation, Boston , MA. In: *Proceedings of the 7th Annual ACC Users Group Conference*, Gettysburg, PA.

Bredell, J. R. (2005). *Numerical Investigation of Fan Performance in a Forced Draft Air-cooled Steam Condenser,* MScEng Thesis, Department of Mechanical Engineering, University of Stellenbosch.

Bredell, J. R., Kröger, D. G. and Thiart, G. D. (2006).'Numerical investigation of fan performance in a forced draft air-cooled steam condenser', *Applied Thermal Engineering*, 26(8–9), pp. 846–852.

Bustamante, .J.G., Rattner, A.S. and Garimella, S. (2016). 'Achieving near-water-cooled power plant performance with air-cooled condensers ', *Applied Thermal Engineering*, 105, pp. 362-371.

Byers, E. A., Hall, J. W. and Amezaga, J. M. (2014). 'Electricity generation and cooling water use: UK pathways to 2050', *Global Environmental Change*, 25(1), pp. 16–30.

Carpenter, S.R., Stanley, E.H. and Vander Zanden, M.J. (2011). 'State of the World's Freshwater Ecosystems: Physical, Chemical, and Biological Changes', *Annual Review of Environment and Resources,* 36, pp. 75-99.

Çengel, Y. and Cimbala, J. (2014). *Fluid Mechanics: Fundamentals and Applications*. 3rd ed. McGraw-Hill Book Company, New York.

Chen, L., Yang, L., Du, X. and Yang, Y. (2016). 'A novel layout of air-cooled condensers to improve thermo-flow performances', *Applied Energy*, 165, pp. 244–259.

Conradie, P.J.F (2010). *Edge Fan Performance in Air-Cooled Condensers*. MScEng Thesis, Department of Mechanical Engineering, University of Stellenbosch.

DiFilippo, M. N. (2008). *Reclaiming water for cooling at SCE's Mountainview power plant*. Available at: http://mydocs.epri.com/docs/AdvancedCooling/PresentationsDay1/10_Session 1 - Mountainview Power_DeFillipo.pdf.

Dixon, S.L. (2010). *Fluid Mechanics and Thermodynamics of Turbomachnery*. 6th ed. Butterworth-Heinemann, London.

Drela, M. (1989). XFOIL: An Analysis and Design System for Low Reynolds Number Airfoils. In: *Proceedings of the Conference Notre Dame*, Indiana.

Duvenhage, K., Vermeulen, J. A., Meyer, C. J and Kröger, D. G. (1996). 'Flow Distortions At the Fan Inlet of Forced-Draught Air-Cooled Heat Exchangers', *Applied Thermal Engineering*, 16(9), pp. 741–752.

Duvenhage, K. and Kröger, D. G. (1996). 'The influence of wind on the performance of forced draught air-cooled heat exchangers', *Journal of Wind Engineering and Industrial Aerodynamics*, 62(2–3), pp. 259–277.

Engelbrecht, R., Meyer, C.J. and van der Spuy, S.J. (2019). 'Modeling Strategy for the Analysis of Forced Draft Air-Cooled Condensers Using Rotational Fan Models'. *Journel of Thermal Science and Engineering Applications,* 11(5), pp. 051011-051020.

EPRI (2004). *Comparison of Alternate Cooling Technologies for California Power Plants Economic, Environmental and Other Tradeoffs*, Palo Alto, CA: 1005358.

EPRI (2012). *Economic Evluation of Alternative Cooling Technologies*, Palo Alto, CA: 1024805.

Fluent (2009). 'ANSYS Fluent documentation', ANSYS Inc.

Fourie, N. (2014). *Simulating the effect of wind on the performance of axial flow fans in air-cooled steam condenser systems.* MScEng Thesis, Department of Mechanical Engineering, University of Stellenbosch.

Fourie, N., van der Spuy, S. J. and von Backström, T. W. (2015). 'Simulating the Effect of Wind on the Performance of Axial Flow Fans in Air-Cooled Steam Condenser Systems', *Journal of Thermal Science and Engineering Applications*, 7(2), pp. 021011-021012.

Gadhamshetty, V., Nirmalakhandan, N., Myint, M. and Ricketts, C. (2006). 'Improving Air-Cooled Condenser Performance in Combined Cycle Power Plants', *Journal of Engineering Energy*, 132(2), pp. 81–88.

Gao, X.F., Zhang, C.W. and Yu, B. (2010). 'Performance predicition of an improved air-cooled steam condenser with deflector under strong wind', *Applied Thermal Engineering*, 30(17-18), pp 2663-2669.

Gur, O. and Rosen, A. (2005). 'Propeller Performance at Low Advance Ratio', *Journal of Aircraft,* 42(2), pp 435-441.

Heinemann, T. and Becker, S. (2014). 'Cross Wind Influence on the Flow Field and Blade Vibration of an Axial Fan', In: 17th International Symposium on Applications of Laser Techniques to Fluid Mechanics, Lisbon, Portugal.

Heinemann, T. and Becker, S. (2017). 'Axial Fan Blade Vibration Assessment under Inlet Cross-Flow Conditions Using Laser Scanning Vibrometry', *Applied Sciences*, 7(8), pp. 862-877.

Hotchkiss, P. J., Meyer, C. J. and Backstro, T. W. Von (2006). 'Numerical investigation into the effect of cross-flow on the performance of axial flow fans in forced draught air-cooled heat exchangers', *Applied Thermal Engineering,* 26, pp. 200–208.

Internal Standards Office. (2007). ISO 5801 - Industrial fans: Performance testing standardized airways.

Joubert, R. (2010). *Influence of geometrical and environmental parameters on air-cooled steam condenser performance.* MScEng Thesis, Department of Mechanical Engineering, University of Stellenbosch.

Kong, Y., Wang, W., Huang, X., Yang, L., Du, X. and Yang, Y. (2017). 'Circularly arranged air-cooled condensers to restrain adverse wind effects', *Applied Thermal Engineering*, 124, pp. 202–223.

Kröger, D. G. (2004). *Air-Cooled Heat Exchangers and Cooling Towers,* Penwell Corp, Tulsa, OK.

Leap CFD Team. (2012). *Tips & Tricks: Inflation Layer Meshing in ANSYS.* Available at: https://www.computationalfluiddynamics.com.au/tips-tricks-inflation-layer-meshing-in-ansys/

Lewis, R.I. (1996). *Turbomachinery performance analysis.* Butterworth and Heinemann, London.

Lindenburg, C. (2004). 'Modelling of rotational augmentation based on engineering considerations and measurements', In: *European Wind Energy Conference*, London.

Liu, P., Duan, H. and Zhao, W. (2009). 'Numerical investigation of hot air recirculation of air-cooled condensers at a large power plant', *Applied Thermal Engineering*, 29(10), pp. 1927–1934.

Louw, F.G. (2011). *Performance Trends of a Large Air-Cooled Steam Condenser during Windy Conditions*. MScEng Thesis, Department of Mechanical Engineering, University of Stellenbosch.

Louw, F.G. (2015). *Investigation of the flow field in the vicinity of an axial flow fan during low flow rates*. PhD Dissertation, Department of Mechanical Engineering, University of Stellenbosch.

Marincowitz, F.S. (2018). *Experimental investigation of the effects of windscreens on air-cooled condenser fan performance and dynamic blade loading*, Unpublished MScEng Thesis, Department of Mechanical Engineering, University of Stellenbosch.

Marincowitz, F.S., Owen, M.T.F. and Muiyser, J. (2019). 'Experimental investigation of the effect of perimeter windscreens on air-cooled condenser fan performance', *Applied Thermal Engineering*, 163, pp. 1-9.

Maulbetsch, J. and DiFilippo, M. (2016). *Final Project Report the Use of Wind Barriers To Air-Cooled Condensers*.

Maulbetsch, J. S., DiFilippo, M. N. and O'Hagan, J. (2011). 'Effect of Wind on Air-Cooled Condenser Performance', *Advances in Aerospace Technology; Energy Water Nexus; Globalization of Engineering,* 1, pp. 391–396.

Menter, F.R., Langtry, R. and Völker, S. (2006). 'Transition Modelling for General Purpose CFD Codes', *Flow Turbulence Combust,* 77, pp. 277-303.

Meyer, C. J. (2004). 'Numerical investigation of the effect of fan performance on forced draught air-cooled heat exchanger plenum chamber aerodynamic behaviour', *Applied Thermal Engineering,* 24, pp. 359–371.

Meyer, C.J. and Kröger, D.G. (2001). 'Numerical simulation of the flow field in the vicinity of an axial flow fan', *International Journal for Numerical Methods in Fluids,* 36, pp. 947-969.

Moore, J. *et al.* (2014). 'Modelling the thermodynamic performance of a concentrated solar power plant with a novel modular air-cooled condenser', *Energy*, 69, pp. 378–391.

Muiyser, J. (2012). *Simultaneous measurement of airflow conditions and the resultant blade and gearbox loading at large-scale cooling system fans*. MScEng Thesis, Department of Mechanical Engineering, University of Stellenbosch.

Muiyser, J. (2016). *Investigation of Large-Scale Cooling System Fan Vibration*, PhD Dissertation, Department of Mechanical Engineering, University of Stellenbosch.

Owen, M.T.F. (2010). *A numerical investigation of air-cooled steam condenser performance under windy conditions.* MScEng Thesis, Department of Mechanical Engineering, University of Stellenbosch.

Owen, M.T.F. (2013). *Air-cooled condenser steam flow distribution and related dephlegmator design considerations*. PhD Dissertation, Department of Mechanical and Mechatronic Engineering, University of Stellenbosch.

Owen, M. T. F. and Kröger, D. G. (2010). 'The effect of screens on air-cooled steam condenser performance under windy conditions', *Applied Thermal Engineering*, 30(16), pp. 2610–2615.

Owen, M. T. F. and Kröger, D. G. (2011). 'An Investigation of Air-Cooled Steam Condenser Performance Under Windy Conditions Using Computational Fluid Dynamics', *Journal of Engineering for Gas Turbines and Power*, 133(6), p. 064502.

Owen, M.T.F. and Kröger, D. G. (2013). 'Contributors to increased fan inlet temperature at an air-cooled steam condenser', *Applied Thermal Engineering*, pp. 1149–1156.

Poullikkas, A., Grimes, R., Walsh, E., Hadjipaschalis, I. and Kourtis, G. (2013a). 'Optimal sizing of modular air-cooled condensers for CSP plants', 93(3), pp. 178–184.

Poullikkas, A., Hadjipaschalis, I. and Kourtis, G. (2013b). 'Comparative Assessment of an Innovative Dry-Cooled CSP System', *Conference Papers in Energy*, 2013, pp. 1–10.

Rao, P., Kostecki, R., Dale, L. and Gadgil, A. (2017). 'Technology and Engineering of the Water-Energy Nexus', *Annual Review of Environment and Resources,* 42, pp. 407-437.

Roache, P.J. (1994). 'Perspective: A Method for Uniform Reporting of Grid Refinement Studies', *Jounral of Fluids Engineering,* 116, pp. 405-413.

Romano, N. (2015). Wind loads on fan blades & blade dynamics. In: *Proceedings of the 7th annual ACC users group conference*, Gettysburg, PA.

Salta, C. A. and Kröger, D. (1995). 'Effect of Inlet Flow Distortions on Fan Performance in Forced Draught Air-Cooled Heat Exchangers', *Heat Recovery Systems & CHP*, 15(6), pp. 555–561.

Sayer, A.T. (1990). *Hydraulic and Compressible Flow Turbomachines*. New York: McGraw-Hill Book Company

Schobeiri, M.T. (2010). *Fluid Mechanics for Engineers A Graduate Textbook.* Berlin: Springer-Verlag.

Shih, T., Liou, W.W, Shabbir, Z.Y. and Zhu, J. (1995). 'A new k- ε eddy viscosity model for high Reynolds number turbulent flows', *Computers Fluids,* 24(3), pp. 227-238.

Spalart, P.R. and Allmaras, S.R. (1994). 'A one-equation turbulence model for aerodynamic flows'. *La Recherche Aerospatiale,* 1, pp. 5-21.

Stinnes, W. H. and Von Backström, T. W. (2002). 'Effect of cross-flow on the performance of air-cooled heat exchanger fans', *Applied Thermal Engineering*, 22(12), pp. 1403–1415.

Thiart, G.D. and von Backström, T.W. (1993). 'Numerical simulation of the flow field near an axial flow fan operating under distorted inflow conditions', *Journal of Wind Engineering and Industrial Aerodynamics,* 45, pp. 189-214.

van der Spuy, S.J., von Backström, T.W. and Kröger, D.G. (2009). 'Performance of low noise fans in power plant air cooled steam condensers', *Noise Control Eng. J,* 54(4), pp. 1-7.

van der Spuy, S. J. (2011). *Perimeter Fan Performance in Forced Draught Air-cooled Steam Condensers*. PhD Dissertation, Department of Mechanical and Megatronic Engineering, University of Stellenbosch.

van Rooyen, J.A. (2007). *Performance trends of an air-cooled steam condenser under windy conditions.* MScEng Thesis, Department of Mechanical Engineering, University of Stellenbosch.

Visser, J.G.J. (1990). *Die invloed van versteurde inlaatvloeipatrone op aksiaalwaaiers*. MScEng Thesis, Department of Mechanical Engineering, University of Stellenbosch.

Yang, L. J., Wang, M.H., Du, X.Z. and Yang, Y.P. (2012).. 'Trapezoidal array of air-cooled condensers to restrain the adverse impacts of ambient winds in a power plant', *Applied Energy*, 99, pp. 402–413.

Yang, L. J., Du, X. Z. and Yang, Y. P. (2011). 'Influences of wind-break wall configurations upon flow and heat transfer characteristics of air-cooled condensers in a power plant', *International Journal of Thermal Sciences*, 50(10), pp. 2050–2061..

Zhang, X. and Chen, H. (2015). 'Effects of windbreak mesh on thermo-flow characteristics of air-cooled steam condenser under windy conditions', *Applied Thermal Engineering*, 85, pp. 21–32.